

PREPARATION, CHARACTERIZATION AND PERFORMANCE STUDY
OF MODIFIED TITANIUM DIOXIDE NANOCRYSTALS FOR
THE LITHIUM-ION BATTERY

A DISSERTATION IN
Chemistry
And
Geosciences

Presented to the Faculty of the University
of Missouri-Kansas City in partial fulfillment of
the requirements for the degree

DOCTOR OF PHILOSOPHY

by
TING XIA

M.E. Zhejiang University, 2008
B.E. Nanjing University of Technology, 2006

Kansas City, Missouri
2015

© 2015

TING XIA

ALL RIGHTS RESERVED

PREPARATION, CHARACTERIZATION AND PERFORMANCE STUDY
OF MODIFIED TITANIUM DIOXIDE NANOCRYSTALS FOR
THE LITHIUM-ION BATTERY

Ting Xia, Candidate for Doctor of Philosophy Degree

University of Missouri-Kansas City, 2015

ABSTRACT

The lithium-ion battery is one of the most widely used rechargeable batteries in today's life. As an energy storage device, it can convert the stored chemical energy into electrical energy when it is being used. Titanium dioxide nanocrystals are well-known for the photocatalytic ability. However, benefited from the nanostructure and the electrochemical reactivity of lithium-ions, titanium dioxide nanocrystals are also investigated as a promising anode material used for the lithium-ion battery. It is safer than graphite as it can prevent the lithium deposition and formation of the solid electrolyte interphase; additionally, it is an environmentally friendly and economical material that can also provide good theoretical capacity. These superiorities have attracted many research interests and make it a target material in this dissertation.

However, the battery made by titanium dioxide suffers poor battery performances that are caused by two major drawbacks of the material. The low electronic conductivity in the solid phase and the low diffusion coefficient of lithium-ions cause only a thin surface layer of the titanium dioxide particle to be effectively used for the intercalation and extraction of lithium-ions at high charge/discharge rates; thus, the actual application is hindered. In order to improve the battery performances, three modification methods were discussed: hydrogenation, vacuum treatment, and carbon coating. The structural and electronic properties of the pure titanium dioxide nanocrystals and the new modified titanium dioxide nanocrystals were studied with: transmission electron microscopy, x-ray diffraction patterns, Raman spectroscopy, Fourier transform infrared spectroscopy, thermal gravimetric analysis, ^1H magic-angle spinning solid state nuclear magnetic resonance spectroscopy, electron spin resonance spectroscopy, and x-ray photoelectron spectroscopy. The coin cells used titanium dioxide nanocrystals as electrode materials and were tested and analyzed in terms of discharge capacity, Coulombic efficiency, and rate performance. The electrochemical impedance spectroscopy was also studied in order to understand the electrochemical system. Compared with the pure titanium dioxide nanocrystals, the hydrogenated titanium dioxide nanocrystals, the vacuum-treated titanium dioxide nanocrystals, and the carbon-coated titanium dioxide nanocrystals showed improved battery performances. The structure and battery performances of three different titanium dioxide nanocrystals were related and discussed systematically.

APPROVAL PAGE

The faculty listed below, appointed by the Dean of the School of Graduate Studies, have examined a dissertation titled "Preparation, Characterization and Performance Study of Modified Titanium Dioxide Nanocrystals for the Lithium-Ion Battery", presented by Ting Xia, candidate for the Doctor of Philosophy Degree, and certify that in their opinion it is worthy of acceptance.

Supervisory Committee

Xiaobo Chen, Ph.D., Committee Chair
Department of Chemistry

Zhonghua Peng, Ph.D.
Department of Chemistry

Nathan A. Oyler, Ph.D.
Department of Chemistry

James B. Murowchick, Ph.D.
Department of Geosciences

Da-Ming, Zhu, Ph.D.
Department of Physics

CONTENTS

ABSTRACT.....	iii
LIST OF ILLUSTRATIONS.....	xiii
LIST OF TABLES.....	xviii
Chapter	
1. INTRODUCTION	1
1.1 Development of the Lithium-Ion Battery	1
1.2 Components of the Lithium-Ion Battery.....	5
1.3 Working Principle of the Lithium-Ion Battery	7
1.4 Key Attributes of the Lithium-Ion Battery	7
1.4.1 Specific Charge and Charge Density.....	8
1.4.2 Theoretical Capacity.....	8
1.4.3 Specific Energy and Energy Density.....	8
1.4.4 Specific Power and Power Density	9
1.4.5 Cycle Life	9
1.4.6 Cycling Efficiency.....	9
1.4.7 Safety.....	9
1.5 Current Research Status and Future Improvements of the Lithium-Ion Battery.	10
1.5.1 Cathode Materials.....	10
1.5.1.1 Early Development.....	10
1.5.1.2 Lithium Transition Metal Oxides	11
1.5.1.3 Lithium Iron Phosphate	13
1.5.1.4 Partial Substitution Compounds.....	14
1.5.1.5 Blended Cathode Materials	14

1.5.2	Anode Materials	15
1.5.2.1	Carbon-Based Materials	15
1.5.2.2	Spinel Lithium Titanate Oxide	18
1.5.2.3	Lithium Metal Alloys	19
1.5.2.4	Oxides.....	19
1.5.3	Separator.....	20
1.5.4	Electrolyte.....	21
1.6	TiO ₂ Nanocrystals.....	22
1.6.1	General Introduction of TiO ₂	22
1.6.2	Nanostructured Materials	23
1.6.3	TiO ₂ Nanomaterials Used in the Lithium-Ion Battery.....	24
1.7	Strategies for TiO ₂ Nanocrystals Used for the Lithium-Ion Battery	26
1.7.1	Addition of Conductive Secondary Phase.....	27
1.7.1.1	Metal Oxides.....	27
1.7.1.2	Metallic Nanoparticles.....	27
1.7.1.3	Graphene Sheets	28
1.7.2	Control of Particle Size.....	29
1.7.3	Use of Different TiO ₂ Space Structures	32
1.7.3.1	Nanorods, Nanowire and Nanotubes (1D)	32
1.7.3.2	Nanosheets (2D)	33
1.7.3.3	Hierarchical 3D Structures	34
1.7.3.4	Porous Structures.....	34
1.7.4	Study of TiO ₂ Polymorphs	35
1.7.4.1	Rutile	35

1.7.4.2	Anatase	36
1.7.4.3	TiO ₂ (B).....	37
1.7.4.4	Brookite	38
1.7.5	Surface Modification	39
1.7.5.1	Coating.....	39
1.7.5.2	Doping	40
1.7.5.3	Surface Treatment.....	41
1.7.6	Strategies Summary	41
1.8	Research Objectives.....	41
1.8.1	Aim 1: Development of New Modification Strategies	41
1.8.2	Aim 2: Systematic Study of Relationships between Structure and Battery Performances	42
2.	EXPERIMENTAL AND ANALYTICAL METHODS	43
2.1	Introduction.....	43
2.2	Synthesis and Modification of TiO ₂ Nanocrystals	44
2.2.1	Synthesis of TiO ₂ Nanocrystals.....	44
2.2.2	Modification of TiO ₂ Nanocrystals	44
2.2.2.1	The Hydrogenated TiO ₂ Nanocrystals.....	44
2.2.2.2	The Vacuum-Treated TiO ₂ Nanocrystals	45
2.2.2.3	The Carbon-Coated TiO ₂ Nanocrystals	45
2.3	Characterization of TiO ₂ Nanocrystals.....	45
2.3.1	TEM.....	46
2.3.2	XRD Patterns.....	48
2.3.3	Raman Spectroscopy	52

2.3.4	FTIR.....	54
2.3.5	TGA.....	57
2.3.6	¹ H-NMR Spectroscopy.....	59
2.3.7	ESR Spectroscopy.....	61
2.3.8	XPS.....	63
2.4	Electrode Preparation.....	64
2.5	Coin Cell Fabrication and Testing.....	64
2.5.1	Coin Cell Fabrication.....	64
2.5.2	Coin Cell Testing.....	65
2.6	Electrochemical Impedance Spectroscopy (EIS).....	66
2.6.1	Introduction of EIS.....	66
2.6.2	EIS Measurement.....	67
3.	DESIGN, PREPARATION AND PROPERTIES OF THE HYDROGENATED TITANIUM DIOXIDE NANOCRYSTALS.....	68
3.1	Introduction.....	68
3.2	Preparation.....	70
3.3	Results and Discussions of Characterization.....	70
3.3.1	Low-Resolution TEM and High-Resolution TEM.....	70
3.3.2	XRD.....	71
3.3.3	Raman.....	77
3.3.4	FTIR.....	78
3.3.5	XPS.....	80
3.4	Results and Discussions of Cycling Performances.....	81
3.4.1	Discharge Capacity.....	81

3.4.2	Coulombic Efficiency	83
3.4.3	Rate Performance	85
3.4.4	Analysis of Galvanostatic Charge/Discharge Profiles.....	87
3.5	Relationships between Structure and Battery Performances	89
3.5.1	Structural Tolerance	90
3.5.2	Hydrogen Mobility	92
3.5.2.1	FTIR.....	92
3.5.2.2	¹ H-NMR.....	93
3.6	Summary.....	94
4.	DESIGN, PREPARATION AND PROPERTIES OF THE VACUUM-TREATED TITANIUM DIOXIDE NANOCRYSTALS	96
4.1	Introduction.....	96
4.2	Preparation.....	97
4.3	Results and Discussions of Characterization.....	98
4.3.1	Low-Resolution TEM and High-Resolution TEM.....	98
4.3.2	XRD.....	99
4.3.3	Raman.....	100
4.3.4	FTIR.....	101
4.3.5	ESR.....	102
4.3.6	XPS.....	104
4.4	Results and Discussions of Cycling Performances.....	106
4.4.1	Discharge Capacity.....	106
4.4.2	Coulombic Efficiency.....	107
4.4.3	Rate Performance	109

4.4.4	Analysis of Galvanostatic Charge/Discharge Profiles.....	111
4.5	EIS Analysis	115
4.6	Relationships between Structure and Battery Performances	120
4.6.1	Structural Tolerance	121
4.6.2	Built-in Electric Field (BIEF).....	122
4.7	Summary.....	124
5.	DESIGN, PREPARATION AND PROPERTIES OF THE CARBON-COATED TITANIUM DIOXIDE NANOCRYSTALS	127
5.1	Introduction.....	127
5.2	Preparation.....	128
5.3	Results and Discussions of Characterization.....	128
5.3.1	Low-Resolution TEM and High-Resolution TEM.....	128
5.3.2	XRD.....	130
5.3.3	Raman.....	131
5.3.4	FTIR.....	132
5.3.5	TGA.....	133
5.4	Results and Discussions of Cycling Performances.....	134
5.4.1	Discharge Capacity.....	134
5.4.2	Coulombic Efficiency.....	136
5.4.3	Rate Performance	137
5.4.4	Analysis of Galvanostatic Charge/Discharge Profiles.....	140
5.5	EIS Analysis	143
5.6	Relationships between Structure and Battery Performances	146
5.6.1	Structural Tolerance	147

5.6.2 Carbon-Coated Layer	148
5.7 Summary.....	149
6. CONCLUSION.....	151
6.1 Structural Similarity.....	151
6.2 Mechanism Differences of Improved Battery Performances	151
6.3 Comparison of Battery Performances for Three TiO ₂ Nanocrystals	153
REFERENCES	156
VITA	173

ILLUSTRATIONS

Figure	Page
1.1. Schematic of an intercalation electrode-based rechargeable lithium-ion battery.	6
1.2. Lattice structures of rutile, anatase, brookite, and bronze (B) of TiO ₂	23
1.3. Schematic diagram of the intercalation of lithium-ions into a particle.	30
1.4. The diffusion of lithium-ions in electrode materials made of (A) bulk crystals, (B) nanocrystals.	31
2.1. Abbe's theory of image formation in a one-lens transmission electron microscope.	47
2.2. The schematic of x-ray diffraction by a crystal.	49
2.3. Simplified x-ray spectrometer.	51
2.4. The principle of Raman spectroscopy.	52
2.5. The schematic of an FTIR spectrometer.	56
2.6. The principal components and ancillary connections in TGA apparatus.	58
2.7. Two proton energy levels in a magnetic field of magnitude B ₀	60
2.8. Zeeman splitting of energy levels of an electron placed in a magnetic field B ₀	62
2.9. Schematic of a coin cell constructed with TiO ₂ as an electrode material.	65
3.1. Low-resolution and high-resolution TEM images of (A and B) the pure TiO ₂ nanocrystals and (C and D) the hydrogenated TiO ₂ nanocrystals.	71
3.2. XRD patterns of the pure TiO ₂ nanocrystals and the hydrogenated TiO ₂ nanocrystals.	73
3.3. Changes in the plane spacing of various lattice planes in the pure TiO ₂ nanocrystals and the hydrogenated TiO ₂ nanocrystals.	73
3.4. Changes in unit cell parameters <i>a</i> and <i>c</i> with unit cell volume <i>v</i> of the pure TiO ₂ nanocrystals and the hydrogenated TiO ₂ nanocrystals.	75

3.5. Average crystalline length along different directions of the pure TiO ₂ nanocrystals and the hydrogenated TiO ₂ nanocrystals.	77
3.6. Raman spectra of the pure TiO ₂ nanocrystals and the hydrogenated TiO ₂ nanocrystals.....	78
3.7. FTIR reflectance spectra of the pure TiO ₂ nanocrystals and the hydrogenated TiO ₂ nanocrystals.....	79
3.8. (A) Ti 2 <i>p</i> (B) C 1 <i>s</i> (C) O 1 <i>s</i> XPS of the pure TiO ₂ nanocrystals and the hydrogenated TiO ₂ nanocrystals.	81
3.9. Variation of discharge capacity versus cycle number for (A) the first 500 cycles and (B) the first 50 cycles of the pure TiO ₂ nanocrystals and the hydrogenated TiO ₂ nanocrystals.....	83
3.10. Variation of Coulombic efficiency along with the charge/discharge versus cycle number of the pure TiO ₂ nanocrystals (A: the first 500 cycles; C: the first 20 cycles) and the hydrogenated TiO ₂ nanocrystals (B: the first 500 cycles; D: the first 20 cycles).	84
3.11. Comparison of the discharge capacities of the pure TiO ₂ nanocrystals and the hydrogenated TiO ₂ nanocrystals at various charge rates.	86
3.12. Galvanostatic charge/discharge profiles for the first cycle at C/25 rate, 35 th cycle at 1 C rate, and 100 th cycle at 1C rate for the electrode made of (A) the pure TiO ₂ nanocrystals and (B) the hydrogenated TiO ₂ nanocrystals.	88
3.13. Galvanostatic charge/discharge profiles at various charge rates (discharge rate = 1C) for the electrode made of (A) the pure TiO ₂ nanocrystals and (B) the hydrogenated TiO ₂ nanocrystals.	89
3.14. Illustration of the hydrogenated TiO ₂ layer to facilitate the fast charge transfer and the capacity retention.	90
3.15. ¹ H magic-angle spinning solid state NMR spectra of the pure TiO ₂ nanocrystals and the hydrogenated TiO ₂ nanocrystals.	94
4.1. Low-resolution, high-resolution TEM, and SAED patterns of (A–C) the pure TiO ₂ nanocrystals and (D–F) the vacuum-treated TiO ₂ nanocrystals.	99
4.2. XRD patterns of the pure TiO ₂ nanocrystals and the vacuum-treated TiO ₂ nanocrystals.....	100
4.3. Raman spectra of the pure TiO ₂ nanocrystals and the vacuum-treated TiO ₂ nanocrystals.....	101

4.4. FTIR reflectance spectra of the pure TiO ₂ nanocrystals and the vacuum-treated TiO ₂ nanocrystals.....	102
4.5. ESR spectra of the pure TiO ₂ nanocrystals and the vacuum-treated TiO ₂ nanocrystals.....	103
4.6. (A) XPS survey and (B) C 1s (C) O 1s (D) Ti 2p of the pure TiO ₂ nanocrystals and the vacuum-treated TiO ₂ nanocrystals.	105
4.7. Variation of discharge capacity versus cycle number for (A) the first 500 cycles and (B) the first 50 cycles of the pure TiO ₂ nanocrystals and the vacuum-treated TiO ₂ nanocrystals.....	107
4.8. Variation of Coulombic efficiency along with the charge/discharge versus cycle number of the pure TiO ₂ nanocrystals (A: the first 500 cycles, C: the first 20 cycles) and the vacuum-treated TiO ₂ nanocrystals (B: the first 500 cycles, D: the first 20 cycles).	108
4.9. Comparison of the discharge capacities of the pure TiO ₂ nanocrystals and the vacuum-treated TiO ₂ nanocrystals at various charge rates.	110
4.10. Galvanostatic charge/discharge profiles for the first cycle at C/25 rate, 35 th cycle at 1 C rate, and 100 th cycle at 1C rate for the electrode made of (A) the pure TiO ₂ nanocrystals and (B) the vacuum-treated TiO ₂ nanocrystals.	112
4.11. Galvanostatic charge/discharge profiles at various charge rates (discharge rate = 1C) for the electrode made of (A) the pure TiO ₂ nanocrystals and (B) the vacuum-treated TiO ₂ nanocrystals.	113
4.12. Comparison of the galvanostatic charge/discharge profiles for the pure TiO ₂ nanocrystals and the vacuum-treated TiO ₂ nanocrystals at charge rate of 20C.....	115
4.13. EIS of the pure TiO ₂ nanocrystals and the vacuum-treated TiO ₂ nanocrystals.	118
4.14. The corresponding components in the circuit and the battery.	119
4.15. Illustration of the vacuum-treated TiO ₂ containing the amorphous layer to facilitate charge transfer and the capacity retention.	121
4.16. The illustration of the facilitation of charge transfer under the BIEF during (A) intercalation and (B) extraction processes.	124
5.1. Low-resolution and high-resolution TEM images of (A and B) the pure TiO ₂ nanocrystals and (C and D) the carbon-coated TiO ₂ nanocrystals.	130

5.2. XRD patterns of the pure TiO ₂ nanocrystals and the carbon-coated TiO ₂ nanocrystals.....	131
5.3. Raman spectra of the pure TiO ₂ nanocrystals and the carbon-coated TiO ₂ nanocrystals.....	132
5.4. FTIR reflectance spectra of the pure TiO ₂ nanocrystals and the carbon-coated TiO ₂ nanocrystals.....	133
5.5. TGA spectra of the pure TiO ₂ nanocrystals and the carbon-coated TiO ₂ nanocrystals.	134
5.6. Variation of discharge capacity versus cycle number for (A) the first 100 cycles and (B) the first 50 cycles of the pure TiO ₂ nanocrystals and the carbon-coated TiO ₂ nanocrystals.....	135
5.7. Variation of Coulombic efficiency along with the charge/discharge versus cycle number of the pure TiO ₂ nanocrystals (A: the first 100 cycles, C: the first 20 cycles) and the carbon-coated TiO ₂ nanocrystals. (B: the first 100 cycles, D: the first 20 cycles).	137
5.8. Comparison of the discharge capacities of the pure TiO ₂ nanocrystals and the carbon-coated TiO ₂ nanocrystals at various charge rates.	139
5.9. Galvanostatic charge/discharge profiles for the first cycle at C/25 rate, 35 th cycle at 1 C rate, and 100 th cycle at 1C rate for the electrode made of (A) the pure TiO ₂ nanocrystals and (B) the carbon-coated TiO ₂ nanocrystals.	141
5.10. Galvanostatic charge/discharge profiles at various charge rates (discharge rate = 1C)for the electrode made of (A) the pure TiO ₂ nanocrystals and (B) the carbon-coated TiO ₂ nanocrystals.	142
5.11. Comparison of the galvanostatic charge/discharge profiles for the pure TiO ₂ nanocrystals and the carbon-coated TiO ₂ nanocrystals at charge rate of 50C.....	143
5.12. EIS of the pure TiO ₂ nanocrystals and the carbon-coated TiO ₂ nanocrystals.	145
5.13. Illustration of a thin carbon layer on the crystalline core of the carbon-coated TiO ₂ nanocrystals.....	147
6.1. Comparison of rate performance for the four TiO ₂ nanocrystals when discharge rate equaled charge rate.	154
6.2. Comparison of rate performance for the four TiO ₂ nanocrystals when discharge was kept at 1C.	154

ILLUSTRATIONS

Scheme	Page
2.1. Classical equivalent circuit of the lithium-ion battery.....	67
4.1. The equivalent circuit modeling used to fit the EIS.	118
5.1. The equivalent circuit modeling used to fit the EIS.	146

TABLES

Table	Page
3.1. Size of the pure TiO ₂ nanocrystals and the hydrogenated TiO ₂ nanocrystals derived from XRD data.....	74
3.2. Unit cell parameters of the pure TiO ₂ nanocrystals and the hydrogenated TiO ₂ nanocrystals.....	76
3.3. Rate performance of the pure TiO ₂ nanocrystals and the hydrogenated TiO ₂ nanocrystals at various charge rates.....	87
4.1. Rate performance of the pure TiO ₂ nanocrystals and the vacuum-treated TiO ₂ nanocrystals at various charge rates.....	111
4.2. The fitted EIS results from the equivalent circuits.	119
5.1. Rate performance of the pure TiO ₂ nanocrystals and the carbon-coated TiO ₂ nanocrystals at various charge rates.....	139
5.2. The fitted EIS results from the equivalent circuits.	146

ACKNOWLEDGEMENT

I would like to express my thanks to my research advisor and committee chair, Dr. Xiaobo Chen for providing me the opportunity to study and do research in his group. As his first Ph.D. student at the University of Missouri-Kansas City, I received a lot of help directly from him. I am impressed by his intelligence and hard work.

I also want to thank my committee members, Dr. Zhonghua Peng, Dr. Nathan A. Oyler, Dr. James B. Murowchick and Dr. Da-Ming Zhu, for giving valuable support to my research and reviewing this dissertation.

I would also like to extend my thanks to the collaborators of our research group: Dr. Zhonghua Peng's group, Dr. Nathan A. Oyler's group, Dr. James B. Murowchick, Dr. Da-Ming Zhu's group, Dr. Tom C. Sandreczki at the University of Missouri-Kansas City, and Dr. Gao Liu's group at the Environmental Energy Technologies Division-Lawrence Berkeley National Laboratory. They helped a lot with sample characterization and testing.

Meanwhile, I must thank my previous and current group members, Dr. Xin Li, Dr. Yuliang Zhang, Mr. Xiaodong Yan, Dr. Zhaohui Hou, Mr. Xiaolin Li, Dr. Lihong Tian and Dr. Min He. I also want to give my thanks to my college students and friends in Kansas City.

I also want to express my thanks to the support from the Department of Chemistry, University of Missouri, Kansas City, University of Missouri Research Board and Dow Kokam.

Finally, I would express my sincerest love and gratitude to my parents who always give me the greatest support and unconditional love.

Dedicated to my parents

CHAPTER 1

INTRODUCTION

1.1 Development of the Lithium-Ion Battery

Nowadays, life quality is much higher than before. But the modern life is highly based on the huge consumption of energy. Meanwhile, the increasing population poses an extremely heavy pressure on the traditional resources. Numerous research efforts have been put into the realm of energy since the 19th century.¹⁻⁶ It includes but is not limited to the renewable energy,¹ energy storage,^{6,7} and energy conversion.⁷ Among them, battery development has attracted the significant attention for energy storage.^{6,8-10} A battery is a device that can store electrical energy into chemical energy and convert the stored chemical energy back into electrical energy when it is being used. It can be used in devices as big as auto vehicles and parts as small as microchips and all electric equipment that can be imagined. There are mainly two types of batteries: primary batteries and secondary batteries. Primary batteries are generally designed to be used once and discarded after use. Zinc-carbon battery, alkaline battery, and metallic lithium battery belong to that category.¹¹ Secondary batteries are also called rechargeable batteries, which can be used within a certain period of time. This type of batteries mainly includes the lead-acid battery, nickel-cadmium battery, nickel-metal hydride battery, and lithium-ion battery.¹¹

However, the problem of how to increase the performance of rechargeable batteries for further application is still under investigation and needs much more effort. The improvements should be focused on the stored energy, power, cycle life, safety, and price.^{12,13}

The first primary battery called Volta's cell^{6,14} was invented in 1800. It used zinc and silver discs that were separated by a cardboard as well as a sodium chloride solution. In 1836, this kind of battery form was evolved into the Daniel cell that had two electrolytes. In 1866, French engineer Georges-Lionel Lechaché¹⁵ further improved it into Lechaché cell, which used a zinc rod negative electrode as an anode, a manganese oxide-carbon mixture as a cathode, and an aqueous ammonium chloride solution as an electrolyte. Although this battery is not used anymore, this concept is widely utilized still today and has made a huge contribution to the commercial market. As for the rechargeable batteries, the lead-acid battery was invented by French scientist Gaston Planté⁶ in 1859. The first nickel-cadmium battery was created by Swedish engineer Waldmar Jungner^{6,14} in 1899. These systems also play a significant role in today's market.

A new approach that exploited lithium as an electrode material appeared from the 1970s.^{6,14,16} Because of the low density, lithium can provide high theoretical specific capacity or energy density. Numerous cathode materials have been developed for this lithium primary battery. The typical battery cells were lithium/manganese dioxide cells, lithium/iodine cells, lithium/thionyl chloride cells, lithium/iron sulphide cells, and lithium polymer cells.⁹ These batteries have their specific applications. In theory, lithium metal

batteries could be made as secondary batteries because lithium-ions formed in the discharge process are expected to be reduced to lithium metal during the charge process. However, this is not the case for two reasons.¹¹ First, the lithium metal generated in the negative electrode has the form of dendrites that will easily cause short-circuiting.¹¹ Second, metallic lithium has a high reaction activity, which has a big impact on battery performances, such as inadequate cycle durability and safety issues.¹¹

The concept of intercalation was introduced in order to make lithium rechargeable batteries. Here, intercalation means a reversible insertion process. It is based on the host material that can reversibly accept and release lithium-ions in and out without any significant change of its lattice structure except for a minor expansion or shrinkage.^{6,14} During the charge process, the negative intercalation electrode that is an anode in this system acts as “lithium-accepting sink,” while the positive intercalation electrode that is a cathode plays a role as “lithium-providing source.”¹⁴ During the discharge process, electrochemical reactions happen reversely. Due to the nature of “rock” for lithium-ions, the new battery system is called the lithium rocking chair battery. The initial research began with cathode materials for the lithium rechargeable batteries, from layered dichalcogenides, then spreading to trichalcogenides and oxides.¹⁷ For anode materials, graphitic carbon is one of the most widely accepted forms. A nonaqueous solution that commonly contains a lithium salt dissolved in a mixture of organic solvents works as the electrolyte. In 1991, SONY successfully commercialized this kind of battery for the first time, using lithium cobalt oxide (LiCoO_2) as a cathode material and carbonaceous

materials as an anode material. It has extensively explored research interests worldwide. The battery has a new name: the lithium-ion battery.

The lithium-ion battery is considered to be a promising rechargeable battery. It uses a lithium-containing mixture as an electrolyte material, making lithium-ions move between the cathode and the anode during the charge and discharge processes. Different from the lithium primary battery, lithium metal is replaced by the lithium source material(s) in the system of the lithium-ion battery, reducing the high safety risk caused by dendrites.

Besides, compared to other batteries, the lithium-ion battery has two main advantages. First, its high specific energy (~ 180 Wh/kg at an average voltage of 3.8 V¹²) makes it suitable for portable electronic devices. By comparison, the specific energy of lead-acid batteries is 33 - 42 Wh/kg.^{18,19} Second, it has long cycling numbers as lithium-ions can be reversibly intercalated and extracted between the lithium-accepting anode and lithium-source cathode without destroying the structure of the host materials.¹² It also has other advantages, such as a low self-discharge rate, simple and efficient production processes.¹¹

Due to these advantages, its applications are not restricted to electronic devices. It can be used for hybrid electric vehicles (HEVs) and electric vehicles (EVs) as well as stationary power sources for storing energy from wind and solar power.¹² However, these applications require higher properties. Also, different types of lithium-ion batteries are needed in order to meet different application focuses. For example, for HEVs, the required specific energy density and specific power density should be above 50 Wh/kg

and 3 kW/kg, respectively. For EVs, the desired values are even higher.²⁰ Moreover, both HEVs and EVs should have the ability of fast charging. However, when charge and discharge rates increase, a large polarization will occur. It is thought to be caused by the slow diffusion rates of lithium-ions in the solid phase and it hinders the further capacity performance.²¹ Hence, the high-rate performance is difficult to achieve. Besides, as the lithium-ion battery always has highly toxic and flammable solvents in the electrolyte, it poses a safety hazard if it is used improperly, such as overcharging or short circuits. Last but not least, the cost for the battery should be affordable for popularization. Therefore, in order to develop new lithium-ion batteries to meet high requirements for different applications, three main directions should be considered. First, make progress in the specific capacity. Second, improve the high-rate performance. Third, ensure the safety and reliability.

1.2 Components of the Lithium-Ion Battery

The lithium-ion battery is mainly composed of four parts:^{20,22} a positive electrode (cathode) that acts as a lithium source, a negative electrode (anode) that works as a lithium sink, a lithium-ion containing electrolyte, and a separator membrane. The schematic of an intercalation electrode-based rechargeable lithium-ion battery is shown in Figure 1.1.²⁰

LiCoO₂ is commercially mature as a cathode material. Other materials, such as LiFePO₄, LiMnO₂, LiNi_xMn_yCo_{1-x-y}O₂, are also developed and applied.²³ They have their

intrinsic strengths and weaknesses concerning energy density, power, safety, cycle life, and cost.

Due to the advantages of low cost, high abundance, and excellent kinetics,²⁴ carbon-based materials (typically graphite) are widely used for anodes. However, the carbon-based materials have the drawbacks that hinder them for large-scale applications. Continuous effort should be made in order to develop more reliable anode materials.

A separator membrane is used to mechanically avoid the short circuit of the anode and the cathode while permitting the transport of free ions and electrons.²² In today's separator market, the most commonly used materials are polyolefine (PO) membranes.²²

A lithium-ion containing electrolyte enables lithium-ions transport between the cathode and the anode. In general, the electrolyte contains the lithium salts, solvents, and specialized additives.²³

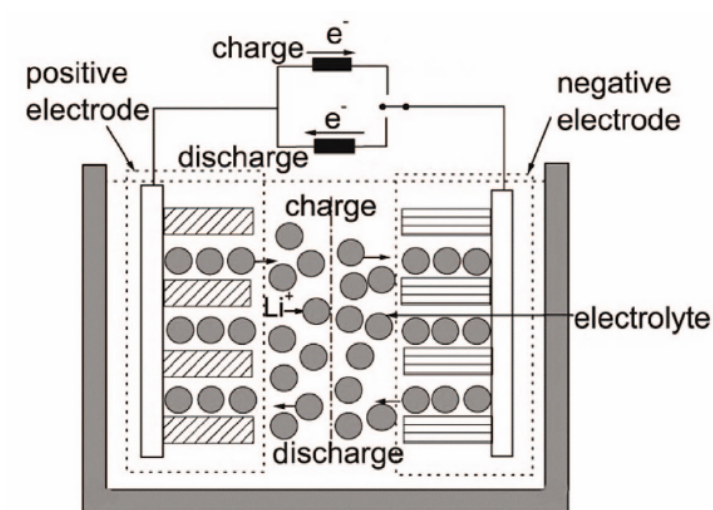
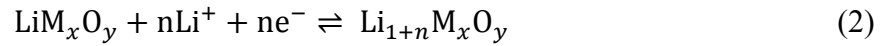
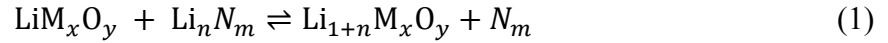


Figure 1.1.²⁰ Schematic of an intercalation electrode-based rechargeable lithium-ion battery.

1.3 Working Principle of the Lithium-Ion Battery

The reaction of the lithium-ion battery can be expressed as follows:



Reaction one represents the reaction happening in the whole battery, while reaction two and three represent the reactions taking place in the positive electrode and the negative electrode, respectively. During the charge process, the lithium-ions are extracted from the positive electrode and intercalated into the negative electrode, gradually making the positive electrode lithium-ion deficient. As for the discharge process, the lithium-ions are extracted from the negative electrode and intercalated into the positive electrode.²⁰

1.4 Key Attributes of the Lithium-Ion Battery

The main attributes of the lithium-ion battery are related to energy density, power density, cycle life, safety, and cost.^{12,13} The following sections list the key attributes of the lithium-ion battery.

1.4.1 Specific Charge and Charge Density

The specific charge (in Ah/kg) and the charge density (in Ah/L) represent the number of available charge carriers per mass and volume unit of material.²⁷ In the terminology of battery, the capacity is the amount of electric charge that can deliver at a rated voltage. Thus, sometimes the term “specific capacity” is also used.

1.4.2 Theoretical Capacity

The capacity of a cell is expressed as the total quantity of electricity involved in the electrochemical reaction and is defined in terms of coulombs or ampere-hours. The theoretical capacity of a battery system, based only on the active materials participating in the electrochemical reaction, is calculated from the equivalent weight of the systems.²⁸

1.4.3 Specific Energy and Energy Density

In order to evaluate the energy content of battery, two terms are introduced:²⁷ the specific energy (Wh/kg) and the energy density (Wh/L). The specific energy represents the electric energy that a battery stores per unit mass. The energy density is the amount of energy stored in a material per unit volume. In order to get high energy content, the electrode materials should achieve two fundamental requirements. One is the high specific charge and charge density. The other is the large standard redox potential difference between two electrodes.

1.4.4 Specific Power and Power Density

The rate capacity is expressed as the specific power (W/kg) and the power density (W/L).²⁷ In battery science, the specific power refers to the electric power that a material can provide per unit mass. The power density expresses the electric power that a battery can provide per unit volume.

1.4.5 Cycle Life

The cycle life is the number of complete charge/discharge cycles that a battery is able to support before its capacity falls under 80% of its original capacity.

1.4.6 Cycling Efficiency

The cycling efficiency represents the percentage of charge that can be recovered in a charge/discharge cycle. Assume the cycling efficiency is 99% for each charge/discharge cycle, after 500 cycles, only 1% specific capacity remains. Thus, a good cycling efficiency indicates a good rechargeability and a long cycle life of a battery.

1.4.7 Safety

Because of the organic solvents (they are usually highly toxic and flammable) used in the battery systems, safety hazards, such as overcharging or short circuits, will be caused when they are used improperly.²⁹ Recently, numerous lithium-ion battery accidents causing fires and explosions have been reported.^{29,30}

Safety concerns the thermal stability of two electrodes and the possibility of short circuits. In order to improve the operation safety of the lithium-ion battery, researchers have put efforts in the fields of the electrode materials,^{31,32} electrolyte,²⁹ separator,³³ and manufacturing methods.³⁴

1.5 Current Research Status and Future Improvements of the Lithium-Ion Battery

As discussed before, the lithium-ion battery can be widely used in both daily life and industry. The performances of the lithium-ion battery largely depend on the materials. Currently, scientists are still looking for the breakthrough in the material field to solve the problems of energy, power, safety, and cost to meet higher requirements. The trend includes but is not limited to the following directions.³⁵ First, find out new lithium-source cathode materials to solve the cost and the environmental issue. Second, develop new lithium-accepting anode materials to improve the safety. Third, replace the current electrolyte with more reliable ones.

1.5.1 Cathode Materials

1.5.1.1 Early Development

The earliest rechargeable lithium batteries used metallic lithium or Li-Al alloys as the anode materials. The layered dichalcogenides,¹⁷ such as titanium disulfide (TiS_2),^{16,36} vanadium diselenide (VSe_2),³⁷ and molybdenum disulfide (MoS_2)³⁸, as well as trichalcogenides and the related materials, such as the triselenide of niobium (NbSe_3),³⁹

and the oxides such as vanadium pentoxide (V_2O_5)⁴⁰ and molybdenum trioxide (MoO_3),⁴¹ were studied as the cathode materials. However, the lithium metal that acted as an anode material in rechargeable batteries turned out to be unsuccessful due to safety issues within current techniques.

1.5.1.2 Lithium Transition Metal Oxides

The lithium transition metal oxides can undergo oxidation to higher valences when the lithium-ions are removed.¹⁷ Although transition metal oxides can maintain charge neutrality in the compound, large compositional changes often cause phase changes, so in order to utilize it in the rechargeable battery, materials must be stable over the wide ranges of the lithium-ion compositions.⁴²

In 1979, Goodenough and co-workers⁴³ first reported $LiCoO_2$ as a new cathode material. SONY first used it in the commercial lithium-ion battery in 1991. From then on, the layer-structured $LiCoO_2$, which has a theoretical capacity of 273 mAh/g,⁴⁴ has dominated the commercial lithium-ion battery market. $LiCoO_2$ has the α - $NaFeO_2$ structure with the oxygen in a cubic close-packed arrangement. It has many advantages, such as easy synthesis, high working potential, and excellent cycle ability. However, it has several limitations. Due to the safety reasons (cut-off voltage is around 4.2 V), the delithiation of $LiCoO_2$ is limited to 0.5 lithium. That means, only half of the theoretical capacity could be obtained.⁴⁵ In other words, when $Li/LiCO_2$ is cycled within the composition range of $0 < x < 0.5$, it has excellent cycling performance. However, if $x > 0.5$, its capacity fades rapidly.⁴⁶

There are several reasons to explain this phenomenon. First, the dissolvability of cobalt in the electrolyte during the charge process will hinder the intercalation of lithium during the discharge process.⁴⁷ In addition, it suffers unstable structure when the lithium composition changes.⁴⁸ The surface coating with inert oxides, such as SnO₂,⁴⁹ Al₂O₃,⁵⁰ and MgO,⁵¹ could be one strategy to improve the structure stability.

Another limitation is related to the diffusion coefficient of lithium-ions in LiCoO₂, which is between 10⁻¹² cm²/s and 10⁻⁹ cm²/s.^{52,53} It is problematic for high power batteries. Furthermore, cobalt is a limited resource and it has a high price, which increases the overall cost of the lithium-ion battery. Finally, it is highly toxic.

Due to its favorable specific capacity compared to LiCoO₂ and the natural abundance, LiNiO₂ is also considered to be a cathode material. Although LiNiO₂ is isostructural to LiCoO₂, it is difficult to synthesize stoichiometric LiNiO₂.⁵⁴ As additional nickel-ions are always found in the lithium layer and reversely in the crystal structure of LiNiO₂, the Li-Ni-O system is represented by Li_{1-y}Ni_{1+y}O₂.⁵⁴ It suffers a poor thermal stability at its high oxidation state. The addition of cobalt to LiNiO₂ can suppress the migration of nickel to the lithium sites.¹⁷ This safety problem could also be overcome by partial substitution of other metals, such as Mg, Mn, and Al.⁵⁵ Blended cathode materials will also be discussed.

The layered LiMnO₂ is also an attractive cathode candidate from an economical and environmental point of view. However, manganese does not form a stable LiMnO₂.¹⁷ LiMn₂O₄ can form a stable spinel phase.

LiMn_2O_4 has spinel structure, in which manganese takes places in the octahedral sites while the lithium-ions mainly take place in the tetrahedral sites.⁵⁶ It is the third most popular cathode material after LiCoO_2 and LiNiO_2 . Same as LiMnO_2 , it is cost-saving and relatively safe. Similar to other cathode materials, it also has drawbacks, such as low specific capacity (~ 120 mAh/g), limited cycling (due to irreversible structure modifications), and storage losses at elevated temperatures (due to Mn^{2+} dissolution into the electrolyte).³⁵ These limitations could be improved by substitution and surface modification.

1.5.1.3 Lithium Iron Phosphate

The ion-based compounds containing polyanions form $(\text{XO}_4)^{n-}$ ($\text{X} = \text{S}, \text{P}, \text{As}, \text{Mo}, \text{W}$) have been studied. Padhi and co-workers⁵⁷ first introduced the lithium iron phosphate (LiFePO_4) as a cathode material in 1997. Iron is not expensive and environmentally friendly compared to cobalt, nickel and vanadium. In addition, lithium-ions can be reversibly intercalated into LiFePO_4 at a high voltage (3.5 V)⁵⁸ and 90% of theoretical capacity (165 mAh/g) could be used. Furthermore, it is more thermally stable in the electrolyte than lithium transition metal oxides.⁵⁹ However, it suffers poor electronic and ionic conductivity that restrict its application in high power batteries.⁴⁶ In order to solve this problem, doping, coating technology, and nanotechnology have been applied to LiFePO_4 to improve the performances.^{58,60}

1.5.1.4 Partial Substitution Compounds

When one cathode material cannot realize excellence in every aspect, partial substitution could be one way to improve the performances. For example, $\text{LiNi}_{1-x}\text{Co}_x\text{O}_2$ ($x \approx 0.8$) has been used to take advantage of the low cost and high capacity of nickel.^{61,62} Small amount of cobalt (up to 0.20-0.25) has shown the ability to improve the capacity.⁴² The partial substitution of manganese-ion by cobalt, iron, or nickel can improve the electronic conductivity of manganese oxide and lead to the formation of $\alpha\text{-NaFeO}_2$ structure.^{17,63,64} $\text{Li}(\text{Ni}, \text{Mn}, \text{Co})\text{O}_2$ composition with equal amount of the three transition metals exhibited excellent discharge capacity and rate capacity.⁴² Moreover, it can be operated at high voltages.⁴²

1.5.1.5 Blended Cathode Materials

Besides the above materials, blended composites have been studied as cathode materials. Blended cathode materials contain a physical mixture of two or more distinct lithium intercalation compounds.⁶⁵ The purpose of blending is to take the advantages of each single material to obtain an overall performances, including reduced capacity loss, longer cycle life, cost saving, and improved thermal stability.⁶⁶ For example, LiMn_2O_4 spinel can be blended with $\text{LiNi}_x\text{Co}_{1-x-y}\text{Al}_y\text{O}_2$ to overcome the shortcomings of the two materials.⁶⁵

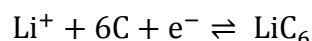
1.5.2 Anode Materials

1.5.2.1 Carbon-Based Materials

The carbon-based materials have received widespread applications as anode materials. They have excellent cycling ability and long cycle life.⁶⁷ The first report⁶⁸ regarding the electrochemical intercalation and extraction of lithium-ions in graphite was published by Yazami and Touzain. Yoshino⁶⁹ invented the lithium-ion battery using carbonaceous material with a certain crystalline structure VGCF (vapor-phase-grown carbon fiber) as an anode material in 1985. After further development, the lithium-ion battery was commercialized by SONY using LiCoO_2 as a cathode material and carbonaceous material as an anode material. Graphite was not used because at that time propylene carbonate that was used as an electrolyte would decompose when graphite was used.¹¹ It has been used properly as an anode material since ethylene carbonate was introduced as an electrolyte material.⁷⁰ After that, the graphitized mesophase microbeads (MCMB) were developed.^{71,72} In today's market, carbon-based materials used for commercial lithium-ion secondary batteries include graphite, soft carbon, and hard carbon. The decomposing precursor determines the carbon types.^{73,74} If the precursor can form a semifluid state, such as petroleum pitch and coal tar pitch, the planar sheets formed in the early stage of pyrolysis can align in parallel to form graphitized structure at a very high temperature. The products could be "soft" or graphitizing carbons.^{73,74} However, if the precursor cannot form a semifluid state, such as phenolic resin and vegetable fibers, the planar aromatic structures cannot align. This kind of product rarely

forms a graphitized structure even at a very high temperature with an ambient pressure. It is so called hard carbon.^{73,74}

Graphite has a three-dimensional layered structure, which can be characterized as stacks of hexagonally bonded sheets of carbon held by van der Waals forces.⁷⁵ Lithium-ions can be intercalated into every 2nd hexagonal planes in the graphite sheets.⁷⁵ That means, every six carbon atoms can hold one lithium atom. It has a theoretical capacity of 372 mAh/g when reaches the formation of LiC₆.⁷⁶



Graphite plays an important role in carbon-based materials used for the commercial lithium-ion batteries in the market because of its high cycling efficiency during the intercalation and the extraction of lithium-ions.⁷⁵ It offers a flat and low voltage range and an affordable price.⁷⁷ However, there is still the room for improvement. First, although the expansion is relatively low, it is not negligible. The volume expansion and shrinkage during the intercalation and the extraction of lithium-ions will cause capacity loss and unsafe situations.²⁵ Furthermore, the low lithium-ion intercalation potential (approaching 0 V vs. Li/Li⁺) will result in the formation of the lithium dendrites during overcharge process.²⁵ Researchers are seeking the alternative materials that can offer not only higher reversible capacity, but also safe operation.

Different from graphite, soft carbon and hard carbon have two-dimensional “turbostratic” structures where ordered graphene sheets are randomly stacked.⁷⁴ A

report⁷⁸ showed that the capacity of soft carbons could reach as high as 700 mAh/g but it underwent voltage hysteresis. But some researchers⁷⁹ also said that due to disordered graphene sheets, the lithium-ions had difficulty intercalating into the interlayer space thus resulted in a low capacity. Hard carbons, although it cannot be graphitized, appear to display much high capacity from 200 to 600 mAh/g over a voltage range of 1.5-0 V vs. Li/Li⁺.⁴⁶ They also have the implementation difficulties, such as low initial Coulombic efficiency and low tap density. Although the spherical hard carbon materials are desirable, the synthesis methods are difficult. Numerous experiments have been performed and studied.⁴⁶

Besides the three types of carbon, the nanostructured carbon materials have been extensively investigated in order to obtain higher capacity for the lithium-ion battery. Two mechanisms can explain the excess storage of lithium-ions during intercalation.⁸⁰ One is to use microcavities or nanopores to store lithium-ions. The other is to utilize the surfaces and interfaces of microcrystalline or nanocrystalline graphite or stacked graphene sheets to get high capacity.⁸⁰ The carbon nanotubes can be considered to be potential anode nanomaterials.^{75,80} Although they have many advantages, such as high conductivity, high tensile strength, and relative inertness, they also have obvious drawbacks, such as irreversible lithium-ion capacity and lack of voltage plateau while battery is discharged.⁷⁵ A lot of research work is waiting to be put on these materials to overcome the difficulties.

1.5.2.2 Spinel Lithium Titanate Oxide

The spinel lithium titanate oxide ($\text{Li}_4\text{Ti}_5\text{O}_{12}$) is another promising anode material. It is called the “zero strain” material for the lithium-ion battery, as it does not undergo obvious particle expansion or shrinkage when lithium-ions are intercalated or extracted.^{81,82} That is mainly because lithium-ions have the same size as the sites in the crystal structure where it stores.⁸¹ One mole of $\text{Li}_4\text{Ti}_5\text{O}_{12}$ can accommodate three moles of lithium-ions with the following electrochemical reaction:⁸¹



According to the equation, the theoretical capacity is 175 mAh/g. Although it is not high compared to graphite, it can offer reversible capacity around 150-160 mAh/g at 1.5 V vs. Li/Li⁺ actually.⁸² Also, it exhibits a flat operation potential plateau. In addition, the undesirable solid electrolyte interphase (SEI) will not form (It occurs at reductive potentials below 1 V vs. Li/Li⁺).⁸³ These advantages can ensure safety and long lifetime for the lithium-ion battery. However, its electronic structure characterized by empty Ti 3d-states with a band gap energy 2-3 eV makes it an insulating material.⁸⁴ The electronic conductivity is below 10^{-13} S/cm.⁸³ That characteristic inhibits its sufficient applications. In order to solve this problem, researchers have tried different modification methods, including reducing particle size, adding conductive materials, and making mesoporous structures.⁸³ Further improvements are still needed.

1.5.2.3 Lithium Metal Alloys

The lithium metal was first investigated as an anode material for the primary lithium batteries. But for the lithium-ion rechargeable battery, it suffers dendrites problem and other safety concerns.¹¹ Much effort has been put into the field of lithium metal alloys (Li_yM , e.g. $\text{M} = \text{Sn}, \text{Pb}, \text{Si}, \text{In}$) because they possess higher theoretical capacity than the carbon-based materials. For example, the theoretical capacity for LiSn and LiSi is 990 mAh/g and 4000 mAh/g, respectively. However, the difficulties are also obvious. The volumes expand and contract dramatically when lithium-ions are intercalated or extracted. This will cause pulverization of the host material and cycling issues.⁴⁶ In other words, when cycling number increases, the volume changes will cause disintegration of the electrode and battery failure. Altering alloy particle size to nanometer scale could be one effective way to improve the cracking problem.⁸⁵ Although nanostructured alloys cannot reduce the volume expansion, they can reduce the cracking of the electrode by altering particle deformation.⁷ Besides, using intermetallic phase instead of a single metal alloy could be another effective way to get good cycling results.⁸⁶ For example, intermetallic Ni_3Sn_4 deposited on the surface of the copper nanorods could be used to achieve high-rate capability and excellent capacity.⁸⁷

1.5.2.4 Oxides

Oxides have attracted researchers' eyes as possible anode materials. For example, SnO_2 has a high theoretical capacity (790 mAh/g) and it can be applied in conjunction with other cathode materials (e.g. LiCoO_2 and LiFePO_4) to have a high overall cell

potential of more than 3 V.⁸⁸ Nevertheless, its initial capacity loss and severe capacity fading upon extended cycling hinder its further applications.⁸⁸ The effort has been made towards the higher-order nanostructured materials through template-assistant methods.³ Also, the concept of composite could be used. Both the carbon loaded SnO₂ composites⁸⁹ and the carbon nanotube-encapsulated SnO₂⁹⁰ have been reported.

Transition-metal oxides, such as CoO, CuO, NiO, and FeO, do not alloy with lithium, but they can react reversibly with lithium-ions, exhibiting high capacity and cycling number. The open structures of the transition-metal oxides can provide space for the intercalation of lithium-ions.⁹¹ The major drawbacks are their poor diffusion rate of lithium-ions and electrons, which could be enhanced by reducing the particle size and other modification methods.⁸⁶

In this dissertation, titanium dioxide (TiO₂) is the target material, which shows an electrochemical activity and has been studied as an anode material. Further discussion will be presented later.

1.5.3 Separator

The separator used in the lithium-ion battery is a porous film that is placed between the cathode and the anode to prevent short circuits of the electrodes while enabling the transport of free ions and electrons.²² There are mainly three types of separators according to structure and composition: microporous polymer membranes, non-woven fabric mats, and inorganic composite membranes. Among them, the most commonly used type is the microporous polyolefine (PO) membrane.²² It can be made of polypropylene

(PP) and polyethylene (PE) by different manufacturing techniques.²² In general, the following properties: chemical stability, thickness, porosity, pore size, permeability, mechanical strength, shutdown, and cost should be considered before battery application.

1.5.4 Electrolyte

Electrolyte is typically a nonaqueous solution with lithium salts that can transfer between the cathode and the anode. Researchers found that the alkyl carbonates could be served as the best solvents for the lithium-ion battery.⁹² The search for a binary solvent mixture is important for the performances of the lithium-ion battery. Lithium hexafluorophosphate (LiPF_6) works as the basic standard lithium salt.⁸² Most commonly, solution of LiPF_6 in ethylene carbonate (EC)-dimethylcarbonate (DMC) serves as an electrolyte for the commercial lithium-ion batteries.⁸² Additives are also needed considering battery performances and safety issues.⁹³ They can improve the formation of the SEI between the electrode and the solution.⁹³ The SEI is formed by electrolyte reduction at the negatively polarized graphite surface during the initial intercalation at about 0.8 V.^{94,95} An ideal passive layer is supposed to prevent further electrolyte decomposition.⁹⁴ When the battery operation temperature is above the critical temperature, the SEI layer decomposes, following by continuous reactions between the electrolyte and the electrodes. It will generate safety problems.⁹⁵ Thus, the SEI has to be thermally stable. Besides, effective additives can help protect electrodes, stabilize LiPF_6 , and ensure safety operation.⁹³ Polymer membrane that can act as both separator and electrolyte is a new direction. A good example is to use polyethylene oxide to host a

lithium salt (e.g. lithium trifluoromethanesulfonate (LiCF_3SO_3)).⁹⁶ In addition, by using this polymer membrane, it is possible to use lithium metal as a rechargeable anode material.⁹⁶ The amorphous and crystalline polymer electrolytes have also been developed.^{35,86} These kinds of solvent free systems can improve battery reliability.

1.6 TiO_2 Nanocrystals

1.6.1 General Introduction of TiO_2

TiO_2 is a famous material. Nowadays, the major consumption for TiO_2 is pigment. It is also used in sunscreens,⁹⁷ ointments, and toothpastes.⁹⁸ Since 1972, Fujishima and Honda⁹⁹ first reported the phenomenon of photocatalytic splitting of water on a TiO_2 electrode under ultraviolet (UV) light, it has been studied as a photovoltaic and photocatalytic material.¹⁰⁰⁻¹⁰²

There are two major crystalline phases of TiO_2 : anatase and rutile. Anatase is kinetically stable in nanocrystalline while rutile is thermodynamically stable.^{103,104} At a high temperature, metastable phase anatase will thermodynamically convert to rutile. The accepted band gap of TiO_2 is 3.0 eV for rutile and 3.2 eV for anatase, but optical absorption only becomes appreciable near ca. 3.5 eV and approaches a maximum above 4.0 eV.^{105,106} Both rutile and anatase have chains of TiO_6 octahedra, where each Ti^{4+} ion is surrounded by an octahedron of six O^{2-} ions. Anatase is well used for catalysts.¹⁰⁷ Because of high refractive index, rutile is well-known for its optical purpose.¹⁰⁸ In addition to the two naturally occurred polymorphs, brookite also occurs naturally.

Besides, there are other synthetic polymorphs, such as $\text{TiO}_2(\text{B})$ (bronze, monoclinic, C2/m), $\text{TiO}_2(\text{H})$ (tetragonal, hollandite-like form), $\text{TiO}_2(\text{II})$ (orthorhombic, $\alpha\text{-PbO}_2$ -like form), baddeleyite-like form (monoclinic, 7-coordinated titanium), $\text{TiO}_2\text{-OI}$ (orthorhombic), cubic form, and $\text{TiO}_2\text{-OII}$ (orthorhombic, cotunnite (PbCl_2)-like).⁹⁵ Figure 1.2 shows the lattice structures of rutile, anatase, brookite, and bronze (B) of TiO_2 .¹³

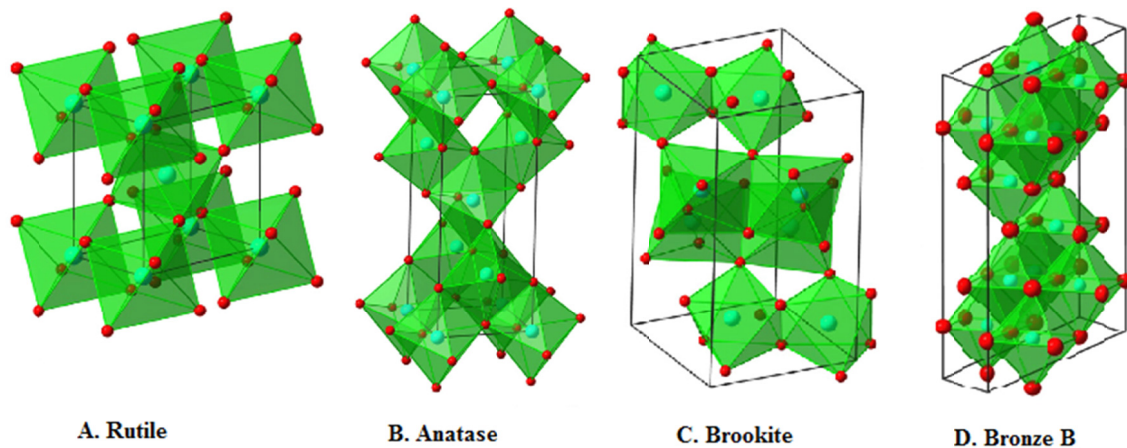


Figure 1.2.¹³ Lattice structures of rutile, anatase, brookite, and bronze (B) of TiO_2 .

1.6.2 Nanostructured Materials

Due to the specific characteristics, nanostructured materials have received tremendous attentions and successes. As the size of the material becomes small to nanometer scale, new physical and chemical properties will appear. This is mainly because specific area and surface-to-volume ratio that have a prominent influence on the

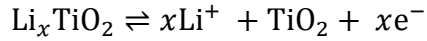
properties will go up rapidly as the material size decreases.^{109,110} Thus, when the nanotechnology plays a role on TiO₂, surprising results may occur. TiO₂ nanocrystals show great potential in many fields, such as photocatalysis¹¹¹ and TiO₂-based devices¹¹¹.

1.6.3 TiO₂ Nanomaterials Used in the Lithium-Ion Battery

In order to broaden the applications of TiO₂ nanomaterials, new approach appeared in the field of the lithium-ion battery. Benefited from the nanostructure and special characteristics, TiO₂ nanocrystals are considered to be an alternative anode material for the lithium-ion battery compared to the traditional graphite, possessing great significance in developing new types of the lithium-ion batteries.

TiO₂ nanocrystals have the following key advantages as an anode material.⁹¹ First, it is not a heavy material. The density for rutile is 4.23 g/cm³, and for anatase it is 3.78 g/cm³. Thus, volumetrically and gravimetrically it can have good theoretical capacity. Moreover, it is an environmentally friendly material with relatively low cost. It also has the superiority over graphite. The relatively high potential *vs.* lithium (relative potential 1.5-1.8 V *vs.* Li/Li⁺) can effectively prevent the lithium deposition and the formation of the SEI layer, which means it is safer than graphite whose operating voltage is close to the intercalation potential of lithium-ions (approaching 0 V *vs.* Li/Li⁺).²⁵

The charge/discharge processes of the lithium-ion battery involve the redox electrochemical reactions, which come up with both charge transfer and diffusivity of lithium-ions between the cathode and the anode.²⁷ The reaction between lithium and TiO₂ can be expressed as follows with a complete Ti⁴⁺ to Ti³⁺ reduction:



where x is the molar fraction of lithium in the TiO_2 . Theoretically, TiO_2 can provide a capacity up to 335 mAh/g, which corresponds to 1.0 lithium per TiO_2 . In actual situation, x is varied with different polymorphs, morphologies, crystal forms, and particle size of TiO_2 . There are two mechanisms to explain the storage of lithium-ions in the host materials.³ The lithium-ions store through intercalation could be one explanation. They can also be stored through electric double layer and surface redox processes. Thus, the intercalation of lithium-ions with the host materials primarily depends on two major transport properties: the electronic conductivity and the diffusivity of lithium-ions.⁹¹ However, the low electronic conductivity (10^{-4} S/cm)²¹ in the solid phase and the low diffusion coefficient of lithium-ions (10^{-11} to 10^{-13} cm²/s)¹¹² are the two major difficulties that cause only a thin surface layer of the TiO_2 particle could be effective for charge and discharge at high rates of the lithium-ion battery. Two obvious problems will occur in this situation. First, full intercalation of lithium-ions into the whole particle is not possible because the center of the TiO_2 particle cannot be utilized. For bulk anatase TiO_2 , $x = 0.5$ was reported to be the maximum value for the electrochemical intercalation of lithium-ions.^{113,114} Second, this will also cause a poor-rate capacity. In addition to the two problems caused by the low electronic conductivity and the low diffusion coefficient of lithium-ions, current TiO_2 anode materials always suffer the problem of an initially irreversible capacity loss. It is believed that the irreversible capacity loss is related to the formation of the SEI.¹¹⁵ However, since the SEI is not formed in the TiO_2 battery system,

how can the capacity loss come from? Although it is not clearly understood, there are several possible hypotheses.¹¹⁶ The intercalation of lithium-ions into the irreversible sites could be considered to be one reason.¹¹⁷ Besides, the capacity loss may come from the side reactions caused by the water absorbed on TiO₂ electrode.¹¹⁸ The poor electronic conductivity could be the third reason.¹¹⁹ Thus, the current battery performances of the TiO₂ electrode turn out to be far from satisfactory. They need to be improved imperatively to meet the application requirements.

Both anatase¹²⁰ and rutile¹²¹ have been studied as the anode materials. Besides, TiO₂(B)¹²² and brookite¹²³ are also investigated. Meanwhile, different modification methods have also been studied. Researchers have put lots of energy to improve the battery performances of TiO₂ nanocrystals electrode. They are discussed as follows.

1.7 Strategies for TiO₂ Nanocrystals Used for the Lithium-Ion Battery

As mentioned before, although TiO₂ nanocrystals are safer anode materials than graphite, the battery performances, especially the rate performance is still unsatisfactory. The low electronic conductivity in the solid phase and the low diffusion coefficient of lithium-ions hinder the practical applications. The intercalation and extraction of lithium-ions can only happen in a thin layer of the particle. The bulk TiO₂ cannot be used sufficiently.

Tremendous work has been put to overcome the two drawbacks. There are two general ways to improve the conductivity.¹¹⁶ One is to add secondary conductive phases to TiO₂. The other is to use one-dimensional (1D) TiO₂ structures, such as nanowires and

nanotubes, because the electrons can efficiently transfer along its 1D geometry.¹¹⁶ As for the improvement of the kinetics associated with the diffusion lithium-ions, approaches could be focused on controlling of the particle size, using different TiO₂ polymorphs, and modification of the surface of the particle.

1.7.1 Addition of Conductive Secondary Phase

Addition of secondary conductive phases could be one effective approach to improve the poor electronic conductivity of TiO₂. Metal oxides like RuO₂,¹²⁰ metallic nanoparticles such as Au,¹²⁴ Ag,^{124,125} have been reported to synthesize the nanocomposites to help improve the electronic conductivity. Conductive carbon-based materials like graphene sheet have also been reported.¹²⁶⁻¹²⁸

1.7.1.1 Metal Oxides

Guo et al.¹²⁰ reported a hierarchically nanostructured electrode with highly efficient mixed conducting 3D networks made of mesoporous TiO₂:RuO₂ nanocomposites. RuO₂ enables favorable surface-surface interactions.

1.7.1.2 Metallic Nanoparticles

Researches showed that the incorporation of metal nanoparticles could improve the electronic conductivity through the formation of a conductive percolation network. Metal-embedded electrodes usually increase the specific capacity by around 10-30%.¹²⁴

He et al.¹²⁵ reported a Ag-modified TiO₂ nanotube material by the traditional silver mirror reaction to improve the electronic conductivity, high-rate discharge capacity, cycling stability, as well as decrease the cell polarization significantly. Nam et al.¹²⁴ used a one-step electrospinning method to embed Ag and Au metal nanoparticles into the anatase TiO₂ nanofibers to achieve better electronic conductivity for the lithium-ion battery (capacity improved 20% or more).

1.7.1.3 Graphene Sheets

Graphene can be served as a composite material for the lithium-ion battery as it has the excellent conductivity, large surface area, good flexibility, chemical stability, and tunable surface functional groups.^{126,129} Its tunable surface functional groups can act as the active nucleation sites for guest materials.¹²⁶ Besides, it may tune the size and the structure of the guest particles.¹²⁶ It can help increase the conductivity ability and keep the volume variation within small fraction.¹²⁸ Li et al.¹²⁶ reported a simple template-free self-assembly method to synthesize the uniform mesoporous anatase TiO₂ nanospheres on the graphene sheets and they showed a superior high-rate performance for the lithium-ion battery. Xin et al.¹²⁸ synthesized a TiO₂/grapheme composite that had an excellent rate performance using hydroxyl titanium oxalate as the precursor. Hou et al.¹²⁷ discovered a composite of graphene-TiO₂(B) nanowires with an excellent storage performance of lithium-ions. They indicated that the usage of the graphene sheets can facilitate the nanotube-nanowire transformation and improve the thermal stability of TiO₂(B).¹²⁷

1.7.2 Control of Particle Size

Currently, the commercial batteries are most made by the micrometer-sized electrode materials that have a low surface area ($< 10 \text{ m}^2/\text{g}$). These micrometer-sized electrode materials are not helpful to the high-rate charge/discharge processes because of the long diffusion length for lithium-ions and low contact area between the electrodes and electrolyte.²⁰ The diffusion of lithium-ions is very complex as the nature of electrolyte phase, solid-liquid interface, tortuosity, and particle size have to be considered.¹³⁰ The process can be simplified and only the overall process is considered. The diffusion length L of the lithium-ions can be estimated with the formula:

$$L = \sqrt{D\tau}$$

where D is the diffusion coefficient and τ is the mean diffusion (or storage) time. The specific capacity Q of the battery can be obtained by $i \times \tau$, where i is the specific charge/discharge current density in A/kg or mA/g. The value of τ will decrease as the increase of i at a certain specific capacity. The effective specific capacity depends on the volume ratio:

$$[r^3 - (r - L)^3]/r^3$$

where r is the radius of the active particle.¹³¹ The schematic diagram of the intercalation of lithium-ions into a particle is shown in Figure 1.3. Within a certain period of time, in

order to realize full capacity, which means the diffusion length L is larger than the particle radius ($L(= \sqrt{D\tau}) \geq r$), there are two different strategies. One is to increase the diffusion coefficient D and the other is to decrease the particle size. Here only the latter situation is discussed. The particle size can be controlled by changing the templates, surfactant, and reaction temperature.¹²⁴

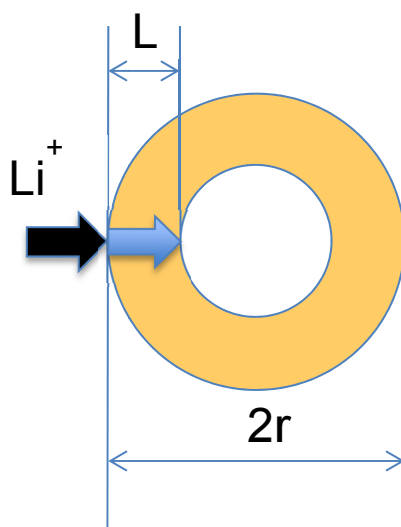


Figure 1.3. Schematic diagram of the intercalation of lithium-ions into a particle.

As shown in Figure 1.4, assume the efficient diffusion distance of lithium-ions is 20 nm, reducing the particle size to 40 nm can let lithium-ions intercalate into the whole particle within a certain period of time. However, the actual performance is always lower than expected, which indicates that besides the size effect, there are also other attributed factors could have impact on the battery performances.

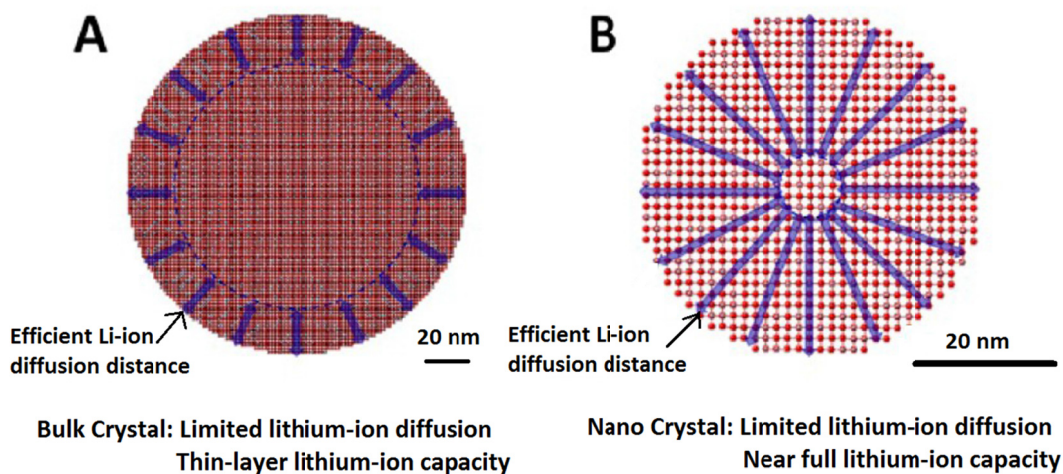


Figure 1.4.¹³² The diffusion of lithium-ions in electrode materials made of (A) bulk crystals, (B) nanocrystals.

Reduce the particle size will not only increase the capacity, but also enhance the rate performance, as a short transport distance can make full diffusion of lithium-ions possible within a short time.¹³³ In addition, smaller particles can also provide a larger electrode-electrolyte contact area, which facilitates the transport of lithium-ions.⁹¹ Especially, as mentioned before, when the particle size is reduced to nanometer scale, the new physical and chemical properties will appear. The nanosized materials can host lithium-ions not only in the bulk, but also in the solid-liquid interface and the solid-solid interface between the host materials, the electrolyte, and the conductive additives.⁹¹

Although it seems that the nanostructured materials have the above advantages, they suffer problems from other concerns. First, the nanostructured materials are easy to form agglomerations, which makes it difficult to disperse uniformly in other materials to make

electrodes.¹³³ Second, the nanostructured materials with a high surface area have a high possibility to have side reactions with the electrolyte.¹³³ Furthermore, using nanostructured materials may decrease the energy density, as more other components (e.g. binder and additives) need to be added.¹³³ In addition, the high surface area makes the tap density lower than that of the bulk materials. This will make an even lower volumetric energy density.⁷ Hence, other strategies including the change of space structures, and surface coating are also needed.

1.7.3 Use of Different TiO₂ Space Structures

Different TiO₂ space structures possess different electrochemical reactivities. One-dimensional (1D) structure provides a direct conductive path,¹¹⁶ which can increase the conductivity of the material. Two-dimensional (2D) structure possesses a large surface area that ensures the large contact area between the electrode and the electrolyte.¹³⁴ Today, even hierarchical three-dimensional (3D) structures have been studied for the lithium-ion battery.^{91,120} Besides, the porous structures with special high surface area have also been discovered to increase the battery performances.¹³⁵⁻¹³⁷

1.7.3.1 Nanorods, Nanowire and Nanotubes (1D)

TiO₂ with 1D structure has the advantages used as an anode material for the lithium-ion battery. It possesses the large surface area and pore volume.¹³⁸ Besides, it has the ability of the efficient electron transport along its 1D geometry.¹¹⁶ Different synthesis

methods can generate different structures, like nanorods,¹³⁸ nanowire,^{119,139} and nanotubes.^{140,141}

Gao et al.¹³⁸ reported nanorods with 3-5 nm in diameter and 40-50 nm in length exhibited high capacity (192 mAh/g, $x = 0.6$), which was larger than the capacity of ordinary anatase.

Armstrong et al.¹³⁹ synthesized TiO₂(B) nanowires to achieve high intercalation capacity of lithium-ions (formation of Li_{0.91}TiO₂(B), corresponding to a specific capacity of 305 mAh/g). Compared to the bulk TiO₂(B), the TiO₂(B) nanowires showed better specific capacity and rate performance, demonstrating the advantage of the nanowire technology.¹³⁹

Highly ordered TiO₂ nanotubes (TNTs) can provide the high surface and high conductivity. However, because TNT arrays are synthesized on Ti foil by the traditional synthesis method, the application for the lithium-ion battery is limited.¹⁴⁰ Park et al.¹⁴¹ synthesized the carbon-coated TNTs by hydrothermal reaction of TiO₂ (anatase) powders with a NaOH aqueous solution to get high-rate capacity.

1.7.3.2 Nanosheets (2D)

The recent¹⁴² research revealed that the anatase TiO₂ nanosheets with exposed (001) facets had could facilitate electronic conductivity. It was reported⁸⁸ that the diffusion of lithium-ions in anatase was along the c -axis. Both the experiments and the theoretical calculation confirmed that the exposed (001) facets had a lower energy barrier for the intercalation of lithium-ions than that of the (101) surfaces.⁸⁸ Thus, by using this

advantage, the TiO₂ hierarchical spheres assembled from nanosheets possessed excellent rate performance.¹⁴³ The rutile nanosheets⁸⁸ were studied as well as the anatase nanosheets.

1.7.3.3 Hierarchical 3D Structures

As mentioned before, Guo et al.¹²⁰ reported a hierarchically nanostructured electrode with highly efficient mixed conducting 3D networks made of mesoporous TiO₂:RuO₂ nanocomposites. The mesoporous 3D structure together with conductive RuO₂ helped increase the battery performances.¹²⁰ Shin et al.⁹¹ discovered a 3D, interconnected, hierarchical nanoporous anatase that had a special high surface area to facilitate the surface storage of lithium-ions.

1.7.3.4 Porous Structures

As porous structures can provide an active large surface area and internal surface area that can help increase the reaction area and enhance the diffusion kinetics, TiO₂ nanomaterials with highly porous structure have attracted a lot of attention.¹³⁵⁻¹³⁷ Jung et al.¹³⁵ found that the pristine mesoporous anatase TiO₂ exhibited higher charge capacity (195 mAh/g, $x = 0.58$) than the ordinary anatase ($x = 0.5$), which could be attributed to the mesoporous structure. Ye et al.¹³⁶ used an additive-free method to synthesize the nanoporous anatase TiO₂ mesocrystals that utilized the advantages of highly porous mesocrystals. This material possessed better rate capacity than nanocrystals, which might

have been benefited from the crystallographically oriented structure with few grain boundaries and increased electrode/electrolyte contact area.¹³⁶ Wang et al.¹³⁷ synthesized the porous TiO₂ nanospheres through a simple sol-gel process followed by a low-temperature hydrothermal treatment. This porous nanospheres had better discharge capacity and rate capacity than the dense TiO₂ materials, which could be ascribed to the increase of surface area caused by porous structure.¹³⁷ It may also alleviate the volume expansion and shrinkage during intercalation and extraction of lithium-ions.¹³⁷

1.7.4 Study of TiO₂ Polymorphs

Four different polymorphs types of TiO₂: rutile, anatase, brookite, and TiO₂(B), have been reported to have different lithium-ion electrochemical reactivities that also vary in different particle sizes and structures.

1.7.4.1 Rutile

Rutile is the most thermodynamically stable polymorph of TiO₂. Bulk rutile can only accommodate negligible lithium (< 0.1 per TiO₂ unit) at room temperature, although it can realize full intercalation at 120 °C.^{144,145} That means the intercalation of lithium-ions into rutile is thermodynamically favorable and the low capacity of rutile capacity at room temperature is limited by kinetic restrictions. A report³ has shown that the oxygen octahedral vacancy is the favorite site for the intercalation of lithium-ions. In order to reach this position, the diffusion of lithium-ions in rutile is highly anisotropic. It shows a

rapid diffusion along the c -axis channels ($\sim 10^{-6}$ cm²/s) and a slow diffusion in the ab -plane ($\sim 10^{-15}$ cm²/s).¹³ Thus, lithium-ions have difficulty reaching thermodynamically favorable octahedral sites and keep staying in the c -channels, which means only one dimension of structure can be used well.¹³ Moreover, the intercalation of lithium-ions may even be limited as repulsive Li-Li interactions in the c -channel and trapped lithium-ions in the ab -plane may block the c -channel.¹³ However, when the particle size is reduced to micrometer or even nanometer scale, this situation can be improved. Hu et al.¹²¹ synthesized the nanometer-sized rutile TiO₂ to obtain up to 0.8 lithium per unit at room temperature. This capacity increase was caused by the short diffusion length of the nanometer particle, where lithium-ions could reach more octahedral sites in the ab -plane within a certain period of time. Besides, they found that lithium-ions preferred the surface storage to the bulk intercalation.¹²¹ Researchers²⁰ also concluded that as the particle size reduced and the specific surface area increased, the main kinetic limitation that was associated with mechanical strains could be reduced, thus more lithium-ions could be stored. In addition to the size effect, researchers¹³ found that the mesoporous crystalline structure could also be used to increase the capacity of rutile.

1.7.4.2 Anatase

Anatase has a tetragonal body-centered space group $I4_1/amd$. It is comprised of two TiO₆ octahedrons sharing two adjacent edges with two other octahedrons so that the planar chains are formed.¹⁴⁶ Lithium-ions can diffuse along the octahedral interstitial sites.^{147,148} During the process of intercalation, the symmetry of anatase unit cell

decreases. When $x = 0.5$ ($\text{Li}_{0.5}\text{TiO}_2$), its original $I4_1/amd$ symmetry transforms into the orthorhombic $Pmn2_1$ space group due to the loss of symmetry in the y direction.¹⁴⁹ The unit volume will increase around 4% as the c -axis decreases and the b -axis increases by symmetry change, which causes a rapid capacity fade.¹⁵⁰ Thus, $x = 0.5$ is considered to be the maximum intercalation value for anatase.^{113,114} It has also been found^{151,152} that during the intercalation of lithium-ions, anatase will separate into $\text{Li}_{0.01}\text{TiO}_2$ and $\text{Li}_{0.6}\text{TiO}_2$ spontaneously on a scale of several tens of nanometers. There is a flat voltage curve indicating a classical bi-phase electrochemical reaction of the intercalation/extraction processes lithium-ions. The behavior of the interaction of lithium-ions with nanostructure appears to like solid solution. Similar to rutile, reduce the anatase particle size will significantly help increase the capacity.¹⁵³ The size reduction, together with the morphologies modification, may increase the capacity of anatase over 0.5 lithium per formula.¹³

1.7.4.3 $\text{TiO}_2(\text{B})$

The lattice structure of $\text{TiO}_2(\text{B})$ is monoclinic (space group $C2/m$). It has chains of TiO_6 octahedra, where each octahedron shares the corners and edges like rutile and anatase.¹⁵⁴ It has more open structures and a lower density than anatase and rutile.¹²⁷ One-dimensional (1D) structure of $\text{TiO}_2(\text{B})$ has attracted research attention for the lithium-ion battery because it can enhance the transfer of electrons along the long dimension and the two short dimensions can facilitate the transport of lithium-ions.¹²⁷

The maximum intercalation of lithium-ions in $\text{TiO}_2(\text{B})$ is about 0.85 per unit, which is larger than rutile and anatase.³ The density functional theory (DFT) study^{98,155} about the energy barrier showed that the favored pathway for the facile diffusion of lithium-ions was along the *b*-axis channel in the (010) direction and the transport of lithium-ions was anisotropic. Different from the solid-solid state diffusion of lithium-ions in anatase, it is believed^{156,157} that the pseudo-capacitive faradic process and the diffusion limited solid-state reaction, which are depended on the microstructure of $\text{TiO}_2(\text{B})$, govern the storage kinetics of lithium-ions. Thus, in order to fully utilize this mechanism, focus should be put on the morphology and structure of $\text{TiO}_2(\text{B})$. Moreover, as $\text{TiO}_2(\text{B})$ is thermodynamically metastable, it is not feasible to undergo high-temperature heat treatment. From this perspective, the low-temperature surface modification or composite preparation may provide suitable ways to improve its performance.²⁵

1.7.4.4 Brookite

Brookite also has an electrochemical reactivity besides rutile, anatase, and $\text{TiO}_2(\text{B})$. Dambournet et al.¹⁵⁸ used a pair distribution function (PDF) to study the intercalation ability of lithium-ions for brookite. They found that brookite could hold up to 0.75 lithium per unit.¹⁵⁸ The specific capacity of brookite also varies as the particle size changes.

1.7.5 Surface Modification

Changing the particle surface can be another viable way to increase the capacity of lithium-ions. The methods include mild oxidation, deposition of metals and metal oxides, coating with polymers, and coating with other kinds of carbons.¹⁵⁹ However, recent research about surface modification of anode is mainly on the carbon-based materials. Surface modification on other anode materials is still far from satisfactory. A lot of attempts have been put into the field of modification to increase the battery performances for TiO₂ anode.

1.7.5.1 Coating

Coating TiO₂ nanocrystals with different materials could also be one way to improve the low conductivity and the low diffusion rate. Depending on the material, the surface coating can promote faster diffusion or transfer. It can also suppress the particle clustering and/or limit the excessive particle growth.¹⁴¹ Carbon coating obtained great attention because of the simplicity and the low cost. However, the improvement is not obvious. Park et al.¹⁴¹ suggested that research focused primarily on an increase of electronic conductivity might not be sufficient to make a huge improvement on the intercalation performance of lithium-ions, especially at high rates. Instead, carbon coating could play a role as a dispersant to prevent agglomerations and enhance electronic conductivity.¹⁴¹ Kang et al.¹⁶⁰ developed a sol-gel method to synthesize the carbon-coated TiO₂ nanotubes by using polyvinylpyrrolidone as a carbon source.

Besides carbon, other materials, like Sn,^{161,162} Cu,¹⁶² MoO_xS_y,¹⁶³ and MoO₂,¹⁶⁴ were also used for coating. Kim et al.¹⁶¹ reported a TiO₂/Sn core/shell nanotube for a high-density storage of lithium-ions.

1.7.5.2 Doping

Xu et al.¹¹⁷ used a sol-gel method to synthesize the carbon-doped TiO₂ nanotubes that had better battery performances than the undoped TiO₂ nanotubes. They demonstrated that the improvement could be ascribed to the suppression of structure degradation and the increase of conductivity after doping.¹¹⁷ Jung et al.¹³⁵ reported a F⁻ doped mesoporous anatase TiO₂ with superior electrochemical performances compared to the pristine TiO₂. They found that the uniform doping of F⁻ could increase the crystallinity, primary particle size, and pore volume.¹³⁵ Besides, F⁻ might have protected the interface between the anode and liquid electrolyte.¹³⁵ Different from adding a secondary conductive phase, trivalent doping had little influence on the improvement of electronic conductivity.^{165,166} Andriamiadamanana et al.¹⁶⁷ synthesized an iron-doped anatase used for the lithium-ion battery at room temperature. They hypothesized that the fast mobility of lithium-ions in the crystal structure was caused by the point defect introduced by the addition of Fe³⁺ and the formation of oxygen vacancies.¹⁶⁷

1.7.5.3 Surface Treatment

Brutti et al.¹²² demonstrated that the irreversible capacity loss of TiO₂(B) nanotubes during the first cycle was caused by the reactions between the surface of nanotubes and the electrolyte. They discovered a surface treatment method by treating TiO₂(B) with C₂H₅OLi to effectively protect the interface.¹²²

1.7.6 Strategies Summary

Researchers have been developed numerous modification strategies to improve the battery performances of TiO₂. It is not difficult to find that combine some of these strategies together to utilize their advantages is suitable. Indeed, it has already been implemented and the results are positive. For example, Liu et al.¹⁶⁸ synthesized the nanosheet-constructed porous TiO₂(B) that combined the advantages of TiO₂(B) polymorph with porous structure and thin nanosheets. This kind of example is common today and can also be found in previous discussions.

1.8 Research Objectives

1.8.1 Aim 1: Development of New Modification Strategies

In this dissertation, three different modification methods of TiO₂ nanocrystals will be presented. They are hydrogenation, vacuum treatment, and carbon coating.

1.8.2 Aim 2: Systematic Study of Relationships between Structure and Battery Performances

The structural and electronic properties as well as the battery performances of three different TiO₂ nanocrystals will be discussed. The relationships between the structure and the battery performances can be revealed. This systematic study can provide better understanding for future improvement. It can accelerate the speed of making the lithium-ion battery with high energy, high power, and high storage, providing new approaches to develop functional TiO₂ nanocrystals.

CHAPTER 2

EXPERIMENTAL AND ANALYTICAL METHODS

2.1 Introduction

Due to the significance of the lithium-ion battery, researchers have put a lot of effort into this area. The performances of the lithium-ion battery largely depend on the materials of electrodes. In order to develop better anode materials for the lithium-ion battery to satisfy different application requirements, TiO_2 is considered to be the targeted alternative. However, as the current battery performances of TiO_2 are not satisfactory, modification of TiO_2 is necessarily needed. According to above background and rationale, anatase TiO_2 nanocrystals are used as a starting material. They were rendered with special characteristics to improve the battery performances.

Three different types of TiO_2 nanocrystals were designed and synthesized by different modification methods. Their structural and electronic properties were studied after that. They were used as electrode materials to make coin cell. Their battery performances were tested and analyzed.

2.2 Synthesis and Modification of TiO₂ Nanocrystals

2.2.1 Synthesis of TiO₂ Nanocrystals

One type of anatase TiO₂ nanocrystals was synthesized as a start material. It was synthesized from a precursor solution consisting of titanium tetraisopropoxide (TTIP, Ti(OCH(CH₃)₂)₄), ethanol, hydrochloric acid, deionized water, and a polymer template (Pluronic F127). The molar ratio of TTIP/ethanol/HCl/H₂O/F127 was 1:40:0.5:15:0.005. The solution was maintained at 40 °C for 24 hours and then dried at 110 °C. The dried powders were calcinated in air at 500 °C for 6 hours to remove the polymer template and to enhance the crystallization of TiO₂ nanoparticles. The pure TiO₂ nanocrystals were obtained after that (They were called “the pure TiO₂ nanocrystals” in this dissertation). They served as the starting material for the three new TiO₂ nanocrystals, as well as a reference sample to compare the battery performances.

2.2.2 Modification of TiO₂ Nanocrystals

2.2.2.1 *The Hydrogenated TiO₂ Nanocrystals*

The hydrogenated TiO₂ Nanocrystals were obtained through a hydrogenation process by placing the pure TiO₂ nanocrystals in a sealed sample chamber under a vacuum for 1 hour followed by hydrogenation under a 20.0 bar H₂ atmosphere at about 200 °C for 5 days.

2.2.2.2 *The Vacuum-Treated TiO₂ Nanocrystals*

The vacuum-treated TiO₂ nanocrystals were obtained from treating the pure TiO₂ nanocrystals in a vacuum chamber at 500 °C for 4 hours. The temperature ramping and cooling rates were 10 °C /min.

2.2.2.3 *The Carbon-Coated TiO₂ Nanocrystals*

The synthesis of the carbon-coated TiO₂ nanocrystals was similar to the vacuum-treated TiO₂ nanocrystals. To wrap up, a precursor solution containing titanium tetraisopropoxide, ethanol, hydrochloric acid, deionized water, and a polymer template (Pluronic F127) was maintained at 40 °C for 24 hours and then dried at 110 °C. The dried powders were divided into two parts. One part was calcinated in air at 500 °C for 6 hours to remove the polymer template and to enhance the crystallization of TiO₂ nanoparticles. The other part did not undergo a calcination process. The calcinated samples (the pure TiO₂ nanocrystals) and uncalcinated samples were put separately into two beakers in the same vacuum chamber at 600 °C for 4 hours. The decomposition of the uncalcinated TiO₂ precursor deposited a thin-layer of amorphous carbon on the surface of the pure TiO₂ nanocrystals to obtain the carbon-coated TiO₂ nanocrystals.

2.3 Characterization of TiO₂ Nanocrystals

The structural and electronic properties of TiO₂ nanocrystals were studied with: transmission electron microscopy (TEM), x-ray diffraction (XRD) patterns, Raman

spectroscopy, Fourier transform infrared spectroscopy (FTIR), thermal gravimetric analysis (TGA), ^1H magic-angle spinning solid state nuclear magnetic resonance (NMR) spectroscopy, electron spin resonance (ESR) spectroscopy, and x-ray photoelectron spectroscopy (XPS).

2.3.1 TEM

TEM is a modern microscope technology to characterize the nanocrystal materials. Today's TEM can not only provide useful information of atomic-resolution lattice, but also give chemical information at a spatial resolution of 1 nm or better, allowing direct identification of the chemistry of a single nanocrystal.¹⁶⁹

A modern TEM is composed of six parts: an illumination system, a specimen stage, an objective lens system, a magnification system, data recording system(s), and a chemical analysis system.¹⁶⁹ The image formation process can be simplified into a single lens microscope as shown in Figure 2.1.¹⁶⁹ The electron gun is the key part of the illumination system. The electron beams that are emitted by the electron gun hit the specimen on the specimen stage. Then, they are diffracted by the lattices of the crystal to form the Bragg beams that are propagating along different directions.¹⁶⁹ The interaction between electrons and specimen will result in changes of phase and amplitude of electron wave that provides the information of the specimen.¹⁶⁹

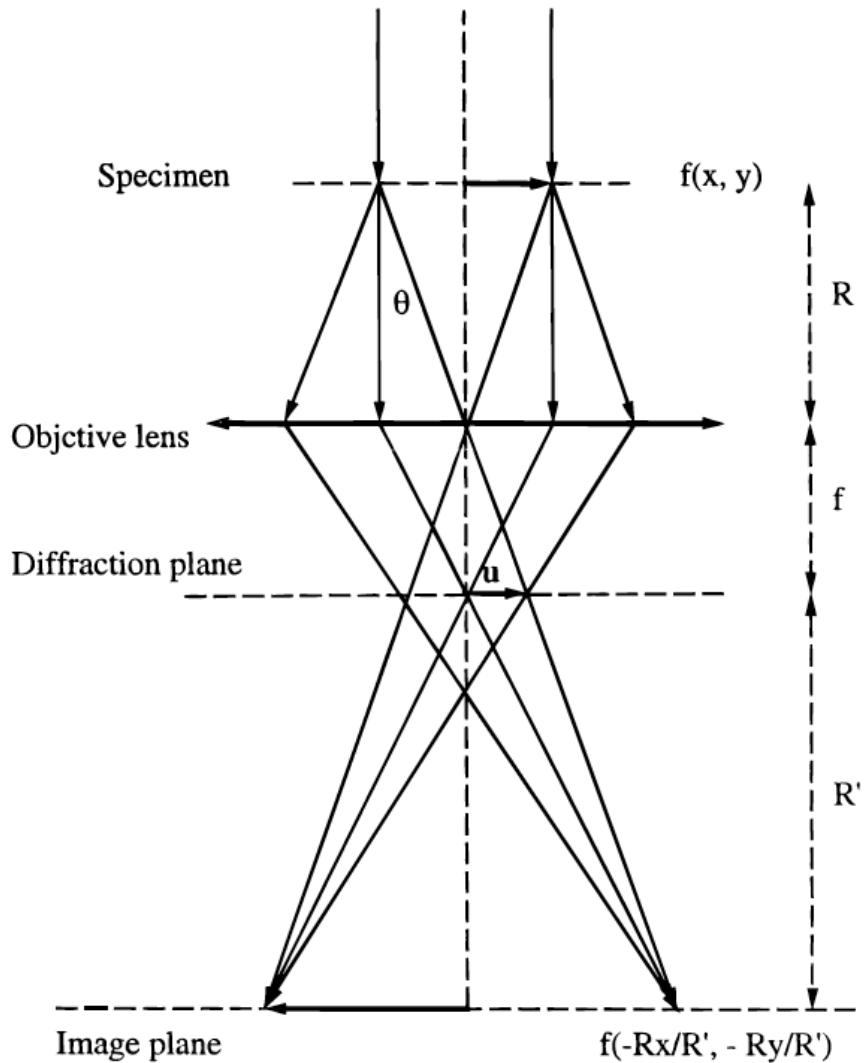


Figure 2.1.¹⁶⁹ Abbe's theory of image formation in a one-lens transmission electron microscope.

In this dissertation, the hydrogenated TiO_2 nanocrystals and the reference pure TiO_2 nanocrystals were characterized by Phillips CM200 TEM (Phillips, Andover, MA). The other samples were performed on an FEI Tecnai F20 TEM (FEI, Hillsboro, OR). The electron accelerating voltage was at 200 kV. A small amount of sample was first

dispersed in water by sonication. One drop of the aqueous suspension was then dropped onto a thin holey carbon film. The grids were then transferred to an oven kept at 60 °C and dried for overnight before TEM measurement.

2.3.2 XRD Patterns

XRD provides the information of the atomic and molecular structure of a crystal. Different polymorphs of TiO₂ nanocrystals have the corresponding spectra. Therefore, it can be used to characterize the polymorphs of TiO₂ nanocrystals. Constructive interference occurs between the scattered x-rays when the path difference ($n\lambda$) equals $2d \sin \theta$. This relationship is described in Bragg's law as follows:

$$n\lambda = 2d \sin \theta$$

where n is an integer, λ is the wavelength of the incident wave (Cu-K, $\lambda = 1.5418 \text{ \AA}$), d is the spacing between the planes in the atomic lattice, and θ is the angle between the incident ray and the scattering planes (Bragg angle).¹⁷⁰ The lattice plane spacings and lattice parameters of crystals can then be deduced. The schematic of x-ray diffraction by a crystal is shown in Figure 2.2:

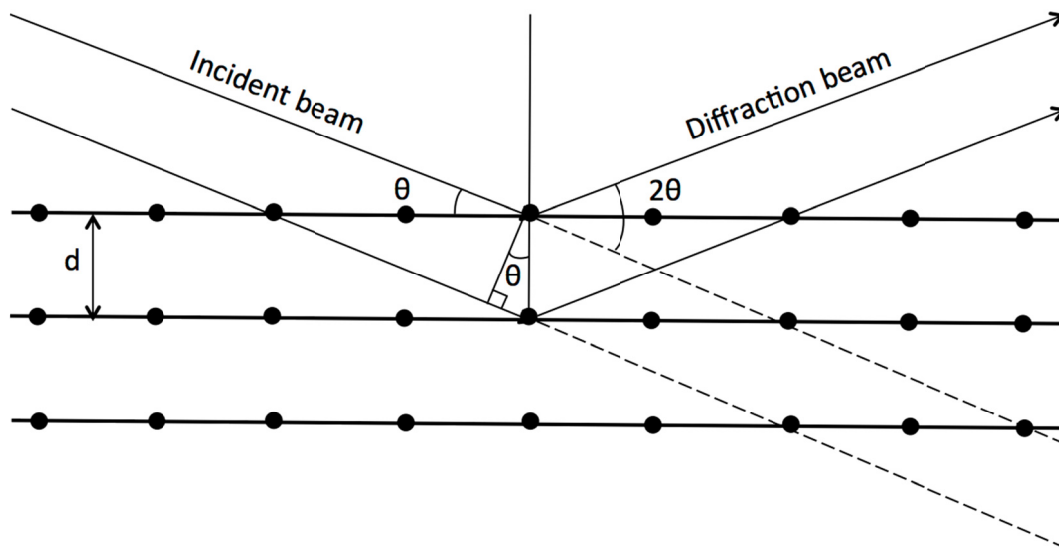


Figure 2.2. The schematic of x-ray diffraction by a crystal.

The crystalline grain size of the nanocrystals can be calculated using the Scherrer equation:

$$\tau = (K\lambda)/(\beta \cos \theta)$$

where τ is the mean size of the ordered (crystalline) domains, which may be smaller or equal to the grain size, K is the shape factor with a typical value of 0.9, λ is the x-ray wavelength, β is the line broadening full width at half maximum (FWHM) peak height in radians, and θ is the Bragg angle.¹⁷⁰ From this equation, it is easy to find that the narrower the peak, the larger the crystalline size. The crystalline size then can be calculated along different directions. Besides, for rutile and anatase TiO₂ nanocrystals,

they have a tetragonal structure. The lattice plane spacing d between adjacent (hkl) planes and the unit cell parameters have the following relationship:

$$\frac{1}{d^2} = \frac{h^2 + k^2}{a^2} + \frac{l^2}{c^2}$$

where a and c are the unit cell lengths.

The essential features of an x-ray spectrometer can be simplified in Figure 2.3.¹⁷¹ X-ray was generated from an evacuated x-ray tube, where electrons bombard a metal (typically Cu). The crystal is usually cut or cleaved to make sure the particular set of reflecting planes of known spacing is parallel to its surface. Both the crystal and the detector can be rotated. In actual use, the incident beam and the crystal intersect at angle θ and the detector is put at the corresponding angle 2θ .¹⁷¹ Some spectrometers are installed with an incident beam monochromator or other optics to improve the functionality.¹⁷²

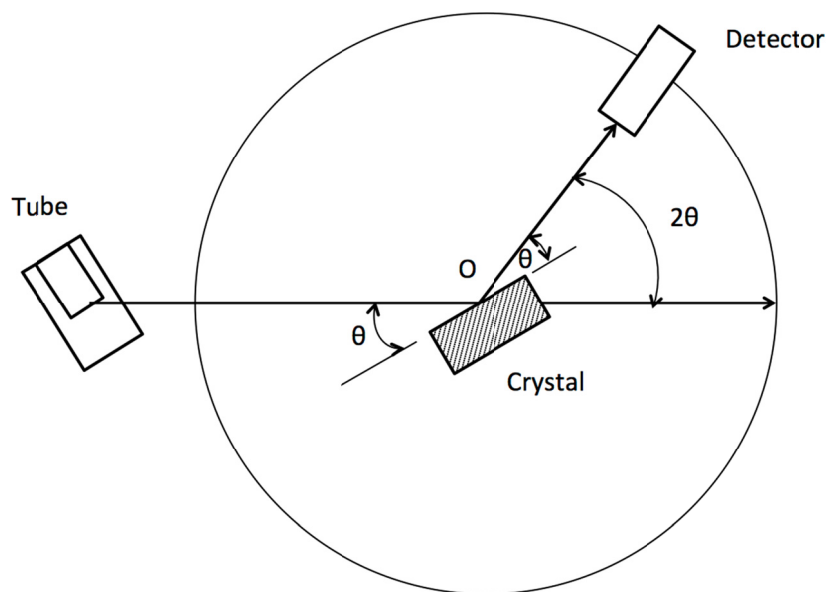


Figure 2.3.¹⁷¹ Simplified x-ray spectrometer.

For the actual measurements in this dissertation, two types of XRD machines were used. The hydrogenated TiO₂ nanocrystals and the reference pure TiO₂ nanocrystals were characterized by Philips X'Pert Pro diffractometer (Phillips, Andover, MA). The other samples were performed using a Rigaku Miniflex Powder XRD machine (Rigaku Americas, The Woodlands, TX). Both machines used Cu K_α as the x-ray sources (wave length = 1.5418 Å) and the 2-theta range was from 15° to 80° with a step width of 0.08 and count time of 3 sec/step. Using the data obtained from XRD, the polymorphs, parameter changes of lattice plane spacing, unit cell length, and the grain size of the TiO₂ nanocrystals were analyzed.

2.3.3 Raman Spectroscopy

Raman spectroscopy is a spectroscopic technique used to detect vibrational, rotational, and other low-frequency modes in a system.¹⁷³ It is a useful tool to investigate the structural properties of nanoparticles, because it provides not only the basic phase identification but also the information about the subtle alterations that are caused by nanoscale structural changes and micromechanical behavior.¹⁷⁴ It relies on inelastic scattering (also called Raman scattering) of monochromatic light from a laser. The principle of Raman spectroscopy can be seen in Figure 2.4. The incident beam interacts with molecular vibrations, phonons or other excitations in the sample, generating the Rayleigh scattering beams (same wavelength with incident beam, will be filtered out) and the Raman scattering beams (new wavelength).¹⁷⁴

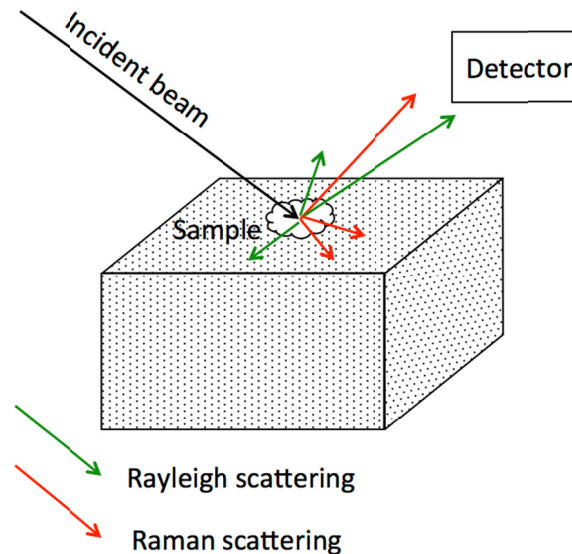


Figure 2.4. The principle of Raman spectroscopy.

With the interaction with laser beam (amplitude E_0 , frequency ν), the polarization of the dipoles will be excited in solids:¹⁷⁴

$$\vec{P} = \vec{\alpha} \times \vec{E}_0 \cos 2\pi\nu_{las}t$$

where \vec{P} is the dipole moment, $\vec{\alpha}$ is the polarizability tensor. Using Taylor approximation, $\vec{\alpha}$ can be individually described as functions of the normal vibration coordinates Q :¹⁷⁴

$$\alpha_{ij} = \alpha_{ij}^0 + \left(\frac{\partial \alpha_{ij}}{\partial Q} \right)_{Q=Q_0} \times Q \quad (i, j = x, y \text{ or } z)$$

Hence, dipole moment can be rewritten as:¹⁷⁴

$$\begin{aligned} P_j &= \sum_j \alpha_{ij} \times E_j \\ &= \sum_j \left[\alpha_{ij}^0 E_{0j} \cos(2\pi\nu_{las}t) + \frac{E_{0j} Q_0}{2} \left(\frac{\partial \alpha_{ij}}{\partial Q} \right)_{Q=Q_0} \right. \\ &\quad \left. \times [\cos(2\pi(\nu_{las} - \nu_{vib})t) + \cos(2\pi(\nu_{las} + \nu_{vib})t)] + \dots \right] \end{aligned}$$

From this equation, the light scattering could be predicted: Rayleigh scattering ($\nu = \nu_{las}$) and Raman scattering ($\nu = \nu_{las} \pm \nu_{vib}$). Raman scattering can be divided into

Stokes Raman scattering ($\nu = \nu_{las} - \nu_{vib}$) and anti-Stokes Raman scattering ($\nu = \nu_{las} + \nu_{vib}$).

For anatase TiO₂, there are six Raman active modes with frequencies at 144 cm⁻¹ (E_{g(1)}, strong intensity), 197 cm⁻¹ (E_{g(2)}, weak intensity), 399 cm⁻¹ (B_{1g(1)}, medium intensity), 513 cm⁻¹ (A_{1g}, medium intensity), 519 cm⁻¹ (B_{1g(2d)}, medium intensity), and 639 cm⁻¹ (E_{g(3)}, medium intensity).¹¹¹ Besides, as reported before, the Raman peaks show increased broadening and systematic frequency shifts as the particle size decreases.¹¹¹ In addition, for the amorphous phase, there is always a large luminescence background.¹⁷⁵ Furthermore, Raman is sensitive to both the crystalline phase and the amorphous phase, while XRD is primarily sensitive to the crystalline phase.¹⁷⁶ Thus, in this dissertation, Raman could be served as an additional technique to examine the structural changes after surface modification. The Raman spectra of the pure TiO₂ nanocrystals and the surface-modified TiO₂ nanocrystals were compared. Therefore, the possible structures for the modified layers could be deduced.

In this dissertation, the Raman spectra were collected on an EZRaman-N benchtop Raman spectrometer (Enwave Optronics, Inc., Irvine, CA). The Raman spectrometer was equipped with a 300 mW diode laser and the excitation wavelength was 785 nm. The spectrum range was from 100 cm⁻¹ to 3100 cm⁻¹. The spectrum collection time was 4 seconds and was averaged over three measurements to improve the signal-to-noise ratio.

2.3.4 FTIR¹⁷⁷

FTIR is the technique used to obtain the infrared spectrum of the sample. Different compounds have different IR spectra. It is a useful tool to identify organic compounds.

Although the IR spectrum is characteristic for the entire molecule, certain chemical bonding groups could give the same frequency no matter what the rest structure of the molecule is. This is the basis for identification of both organic compounds and other compounds that contain certain chemical groups. FTIR and Raman are quite similar. But different from Raman spectroscopy, (in FTIR) molecules can only absorb the photon energy that is equal to energy level differences in the molecule. Hence, the two techniques are complementary.

The schematic FTIR spectrometer is shown in Figure 2.5. Radiation containing all IR wavelengths is split into two beams: fixed length beam and variable length beam. A sequence of constructive and destructive interferences will be generated and form an interferogram when varying the distances between path lengths. Fourier transformation then converts this interferogram into FTIR spectrum.

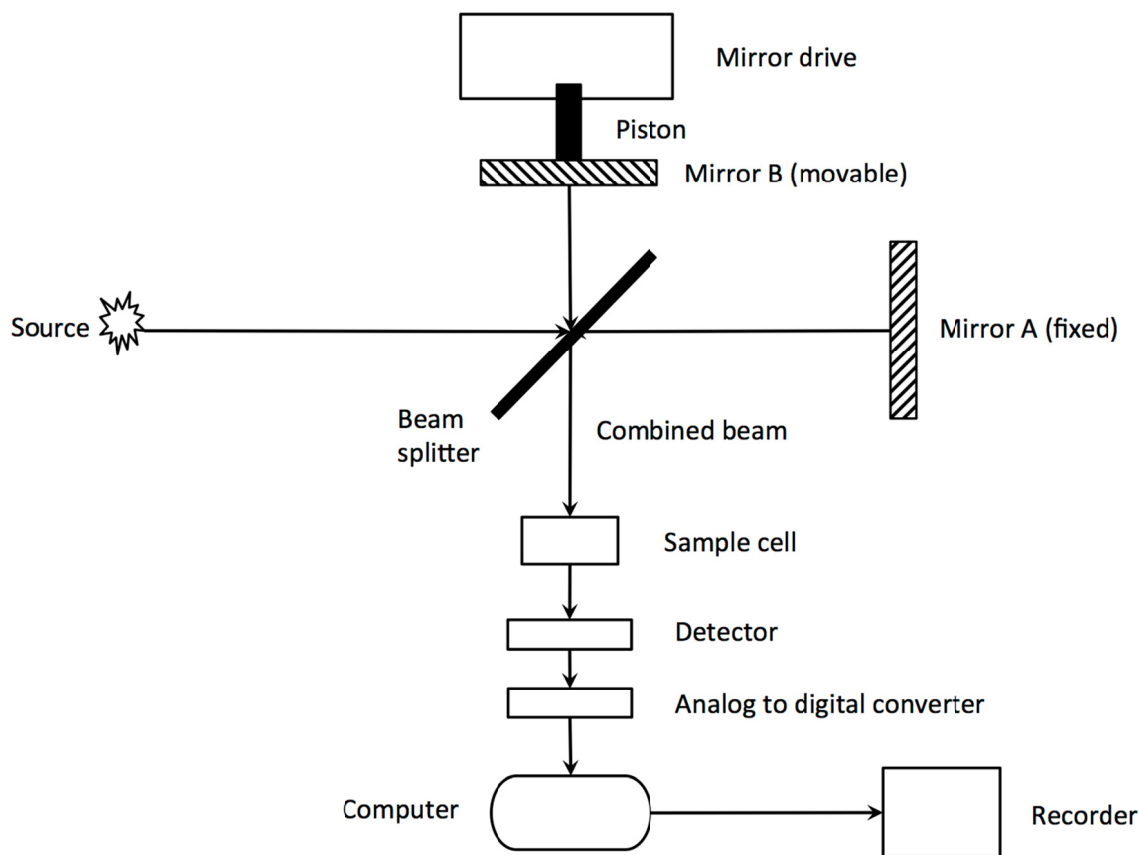


Figure 2.5.¹⁷⁷ The schematic of an FTIR spectrometer.

In general, the pure TiO₂ nanocrystals have a sharp peak below 1000 cm⁻¹ due to O-Ti-O vibrations in the TiO₂ lattice.¹⁷⁸ Besides, if there is any contamination or organic residue left after surface modification, it could be detected from FTIR spectra. By comparing FTIR spectra of the pure and the surface-modified TiO₂ nanocrystals, subtle differences may be observed. Therefore, it could be served as another tool to identify the structure.

In this dissertation, The FTIR spectra were collected using a Thermo-Nicolet iS10 FTIR spectrometer (Thermo Fisher Scientific, Waltham, MA) with an attenuated total

reflectance unit. Background was collected before every sample collection and the scan number was set to be 64.

2.3.5 TGA¹⁷⁹

TGA is the experimental technique to measure the mass change of the sample during heating process. This mass change can be caused by chemical reactions or physical changes. It can be used to study the chemical reaction, thermal behavior of reaction, and water loss of drugs among others.

Figure 2.6 shows the principal components and ancillary connections in TGA apparatus. By balance mechanism and mass measurement, the accurate mass change of the sample can be obtained during the temperature elevation process.

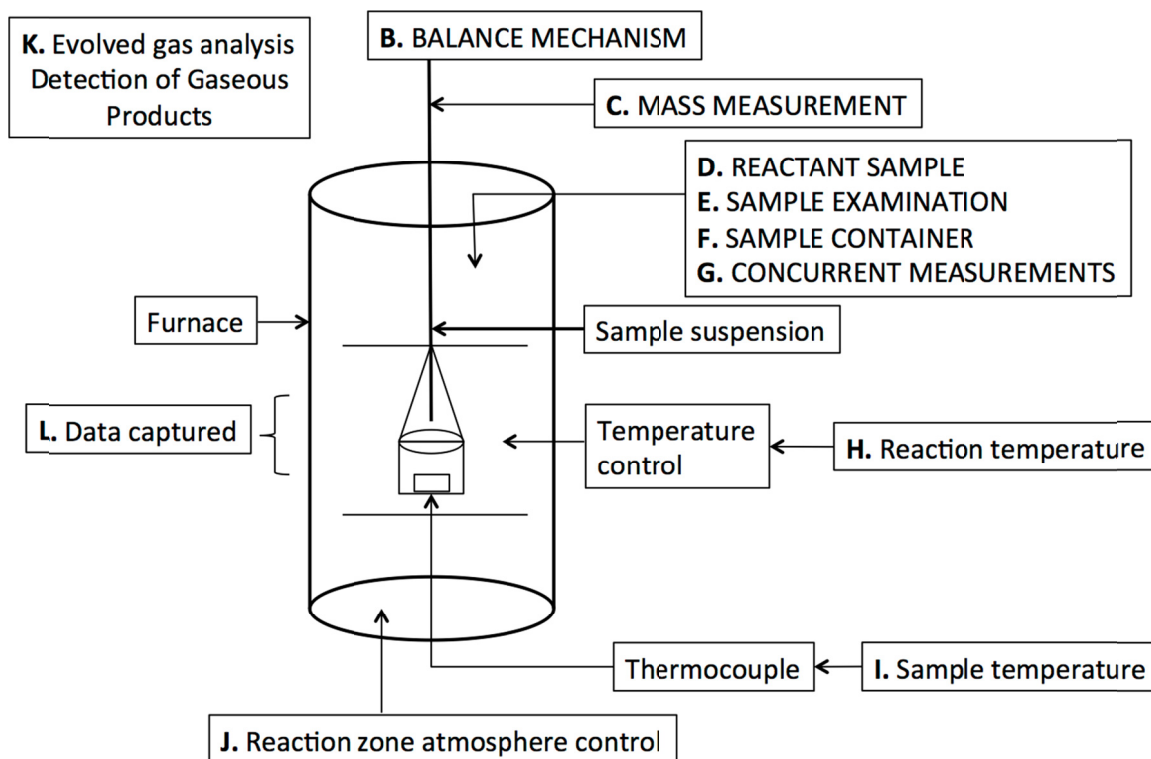


Figure 2.6.¹⁷⁹ The principal components and ancillary connections in TGA apparatus.

For carbon-coated samples, TGA was used to find out how much carbon was coated on the surface of TiO₂ nanocrystals. If there is carbon coated on the surface, a weight loss difference between the pure TiO₂ nanocrystals and the carbon-coated TiO₂ nanocrystals will occur during the heating process, as the carbon layer will decompose at a high temperature. By calculating the weight changes, the amount of carbon loaded on the surface can be analyzed. The experiments were performed on an SDT-Q600 analyzer (TA Instruments Inc., New Castle, DE) in a flowed air environment. The temperature range was set from room temperature to 1000 °C at a ramp rate of 5 °C/min. Weight changes could be found during the heating process.

2.3.6 ^1H -NMR Spectroscopy¹⁷⁷

^1H -NMR is also called proton magnetic resonance. It is used to measure the hydrogen environment of the sample. Due to the nuclear spin of ^1H , in an external magnetic field, there are two energy levels and a slight excess of proton population in the lower energy state in accordance with the Boltzmann distribution as shown in Figure 2.7.

I is quantum spin number. α, β are the two states. ΔE is given by:

$$\Delta E = \left(\frac{h\gamma}{2\pi} \right) B_0$$

where h is Planck's constant, γ is the magnetogyric ratio, a fundamental nuclear constant.

It can be expressed by:

$$\gamma = \frac{2\pi\mu}{hI}$$

where μ is the magnetic moment.

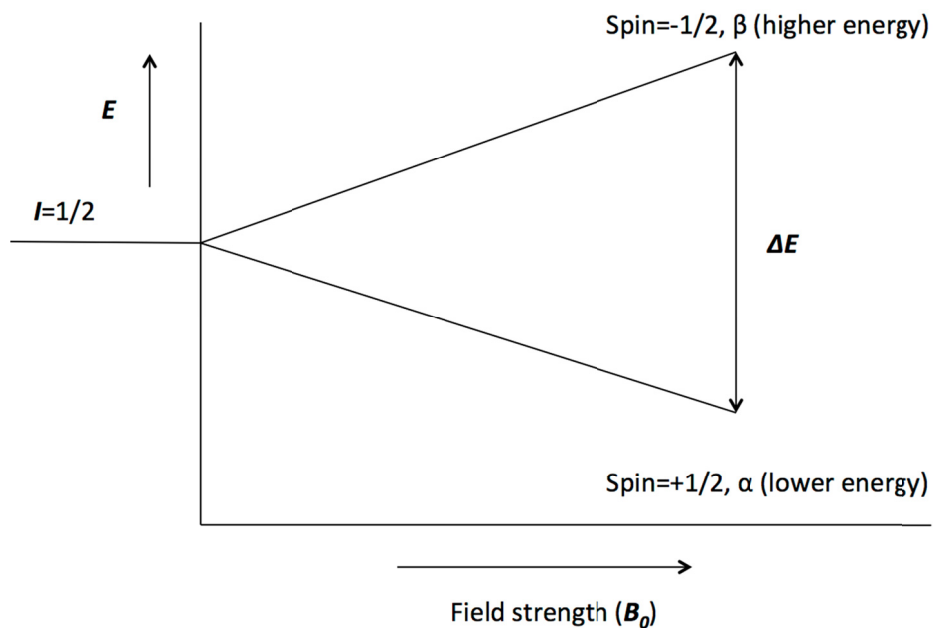


Figure 2.7.¹⁷⁷ Two proton energy levels in a magnetic field of magnitude B_0 .

When frequency ν_1 and magnetic field B_0 meet the following relationship ($\Delta E = h\nu$), the system is in resonance. The proton absorbs energy and raises to a higher energy state, and a spectrum can be obtained.

$$\nu_1 = \left(\frac{\gamma}{2\pi}\right) B_0$$

There are two kinds of relaxations. Relaxation indicates the process of re-equilibration after applying some perturbation. The time spent for longitudinal magnetization to reach equilibrium magnetization is called the spin-lattice relaxation time constant (T_1). It is related to the transfer of energy from the “excited” protons to the

surrounding protons. The time constant for perpendicular magnetization to reach equilibrium is called the transverse relaxation time constant (T_2). It concerns the transfer among the precessing protons. In general cases, because T_2 is long enough and T_1 is short enough, the relative number of different kinds of protons can be determined by the peak area.

Because protons in a molecule are shielded by the electron clouds, different protons with different chemical environments have different chemical shift positions. In this dissertation, ^1H -NMR was measured for the pure TiO_2 nanocrystals and the hydrogenated TiO_2 nanocrystals to compare the different chemical environment of hydrogen. The NMR experiments were performed on an 8.45T Oxford magnet with a three-channel Tecmag Apollo NMR console, using a home-built, doubly tuned, MAS solid-state NMR probe with a 3.2 mm stator assembly from Revolution NMR. The magic angle spinning (MAS) rate was 12kHz, the proton excitation pulse during the Bloch decay experiment was ~ 50 kHz, and the spectra were externally referenced to adamantane. Each spectrum was acquired with 16 scans and the subtraction was performed after normalizing the peak at ~ 6 ppm. Both the pure TiO_2 nanocrystals and the hydrogenated TiO_2 nanocrystals were evacuated at room temperature overnight to remove the surface adsorbed water from the atmosphere.

2.3.7 ESR Spectroscopy¹⁸⁰

ESR concerns the resonant absorption of microwave radiation by paramagnetic systems in the presence of an applied magnetic field. It is a technique to study the

unpaired electrons. When paramagnetic substances are put in a magnetic field, energy levels of an electron will be split as shown in Figure 2.8. ΔE can be expressed as:

$$\Delta E = g\mu_B B_0$$

where g represents g-factor and μ_B is Bohr magneton.

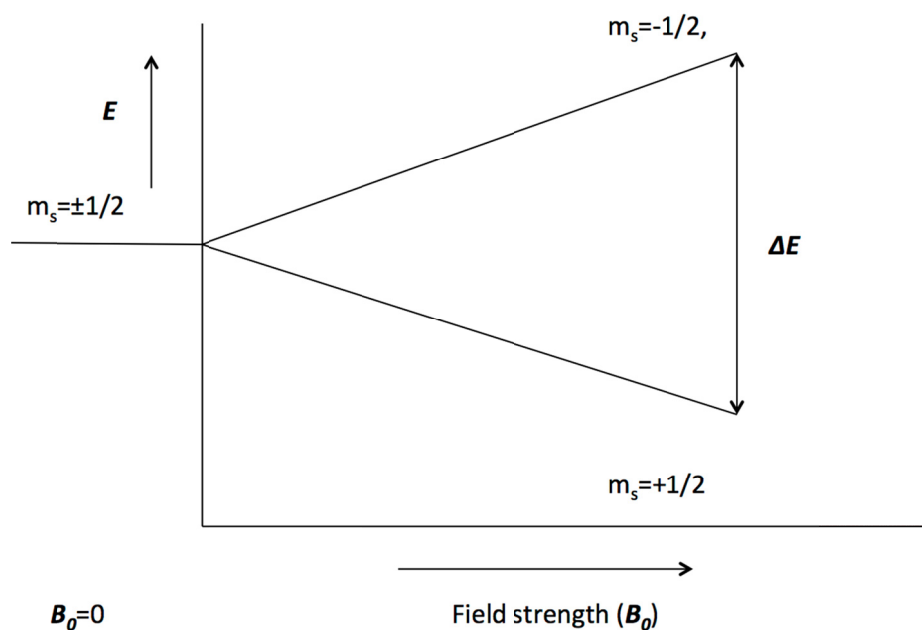


Figure 2.8. Zeeman splitting of energy levels of an electron placed in a magnetic field B_0 .

Similar as $^1\text{H-NMR}$, when frequency ν and magnetic field B_0 meet the following relationship, the system is in resonance. A spectrum can be obtained as the system absorbs the energy.

$$\Delta E = h\nu = g\mu_B B_0$$

ESR was used to examine whether oxygen vacancies were created during the process of vacuum treatment. The ESR spectra were collected on a Benchtop Micro-ESRTM spectrometer (Active Spectrum, Foster City, CA), at a microwave frequency of 9.70 GHz at room temperature without light irradiation. The ESR data were calibrated in relation to $g = 2.0066$ of 2,2,6,6-tetramethyl-4-hydroxylpiperidine-1-oxyl. The scanning time was 30 s per sweep, and the spectrum was averaged after 30 sweeps. Quartz ESR tubes with an inner diameter of about 5.8 mm was used.

2.3.8 XPS

XPS gives the chemical bonding and valance band information of the sample. It is obtained by irradiating a sample with monoenergetic x-rays and analyzing the electrons emitted. The emitted electrons have the following kinetic energies:

$$E_k = h\nu - E_B - \phi_s$$

where $h\nu$ is the energy of the photon. E_B is the binding energy of the atomic orbital from that the electron originates, and ϕ_s is the spectrometer work function.

The T $2p$, O $1s$, and C $1s$ XPS spectra of pure and modified TiO₂ nanocrystals were measured by XPS on a PHI 5400 XPS system (ULVAC-PHI, Inc., Japan) equipped with a conventional (non-monochromatic) Al anode x-ray source with K α radiation. Small

amount of TiO₂ nanocrystals were pressed onto conductive carbon tape for XPS measurements. The binding energies from the samples were calibrated, with respect to the C 1s peak, from the carbon tape at 284.6 eV.

2.4 Electrode Preparation

Half-cells were fabricated as follows.¹⁸¹ The materials used in the fabrication of these half-cells include acetylene black (AB), polyvinylidene fluoride (PVDF), and N-methylpyrrolidone (NMP). The preparation of the TiO₂ electrodes was conducted in an argon-filled glove box. The electrode mixture (82 wt% TiO₂, 8 wt% AB, and 10 wt% PVDF) was steadily dispersed in NMP using a Polytron PT10-35 homogenizer at 2700 rpm for 30 minutes. The slurry was cast on a battery-grade copper sheet using a doctor blade. After being dried overnight, the electrodes were punched to 1/2" diameter discs and dried in vacuo at 110 °C overnight before being assembled into coin cells. The electrode loading was controlled at around 1.2 mg TiO₂/cm².

2.5 Coin Cell Fabrication and Testing

2.5.1 Coin Cell Fabrication

Coin cell assembly was prepared in standard 2325 hardware under a dry argon atmosphere. The separator was from Celgard (product 2400). 1M lithium hexafluorophosphate (LiPF₆) in ethylene carbonate (EC): diethyl carbonate (DEC) (1:2 weight ratio) was used as the electrolyte solution, and lithium as the counter electrode.

Figure 2.9 shows the schematic of a coin cell constructed with TiO_2 as an electrode material.

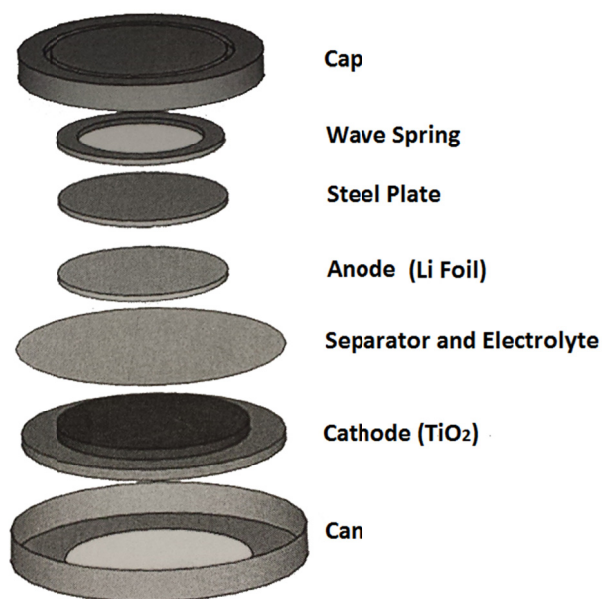


Figure 2.9. Schematic of a coin cell constructed with TiO_2 as an electrode material.

2.5.2 Coin Cell Testing

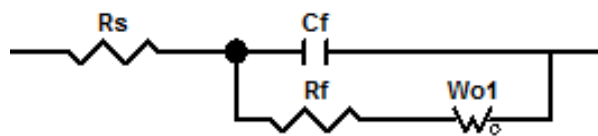
For the modified TiO_2 nanocrystals and the reference pure TiO_2 nanocrystals, cells were discharged to 1.0 V and charged to 3.0 V after 15 min resting for the first cycle at C/25 (calculated from a specific capacity value of 335 mAh/g) using a Maccor battery cycler at 30 °C. For the second cycle, cells were discharged to 1.0 V and charge to 3.0 V at C/5. Then the cells were cycled at 1C from 1.0 V to 3.0 V. One data point was recorded every 10 mV of voltage change. For the first 18 cycles of the rate performance

test, the charge and discharge rates were changed simultaneously, and for the following cycles only the charge rates were changed while the discharge rate was kept at 1C.

2.6 Electrochemical Impedance Spectroscopy (EIS)

2.6.1 Introduction of EIS

EIS is a technique for understanding electrochemical systems. By measuring cell impedance in the form of real and imaginary components and phase angle, it is possible to simulate the electrochemical processes, such as the electronic/ionic conduction in the electrode and electrolytes, interfacial charging either at the surface films or the double-layer, charge transfer processes, and the mass transfer effects in the cell by equivalent circuit.¹⁸² The classical equivalent circuit can be depicted in Scheme 2.1. R_s represents the ohmic resistance, including the bulk resistance of the electrolyte, separator, and electrode. C_f represents the double layer capacitance the electrode interface. R_f is charge transfer resistance and W_{ol} is Warburg impedance representing the mass transfer effects interfering with the charge transfer processes. However, the actual process is much more complicated than the above equivalent circuit, especially for the surface-modified TiO₂ nanocrystals. New equivalent circuits should be established based on the classical one according to different modification methods.



Scheme 2.1. Classical equivalent circuit of the lithium-ion battery.

2.6.2 EIS Measurement

EIS was measured with a Biologic potentiostat/EIS instrument. The frequency range was between 1 MHz and 10 mHz. The voltage modulation applied was 100 mV.

CHAPTER 3
DESIGN, PREPARATION AND PROPERTIES OF THE HYDROGENATED
TITANIUM DIOXIDE NANOCRYSTALS

(The main content of this chapter was published in Nano Energy, 2013, 2, 826-835 entitled “Hydrogenated surface disorder enhances lithium ion battery performance” and Journal of Materials Chemistry A, 2013, 1, 2983-2989 entitled “Revealing the structural properties of hydrogenated black TiO₂ nanocrystals” as research article.)

3.1 Introduction

Anatase TiO₂ nanocrystal was used as a starting material to study the battery performances of the surface-modified TiO₂. As discussed before, for ordinary anatase TiO₂, only half capacity could be reached as the capacity fade because of the structural deformation.^{113,114,149,150} Lots of effects, including size reduction and morphology modification, have been made in order to improve the performances.¹³ Lu et al.¹⁸³ reported the hydrogenated TiO₂ nanotubes with significantly improved electrochemical performances as electrode materials for supercapacitors. The enhancement in capacitance was proposed to be caused by the combined contribution from the improved donor density and the increased density of surface hydroxyl groups.¹⁸³

Chen et al.¹⁷⁶ reported that by hydrogenation under a high pressure and an elevated temperature, the pure TiO₂ nanocrystals (white) would turn out to be the hydrogenated TiO₂ nanocrystals (black). The arrangement of the atoms on the surface layers surrounding the crystalline TiO₂ core was changed during this process.¹⁷⁶ The overlap of the oxygen *p*- and titanium *d*-orbitals, along with a mixing of the hydrogen *s*-orbitals with those of TiO₂ induced mid-gap electronic levels above the valence band of TiO₂, where the H atoms were partially bonded to both O atoms and Ti atoms.¹⁷⁶ For the hydrogenated TiO₂ nanocrystals, the highly crystalline core was covered by a highly disordered layer. This crystalline/disordered core/shell structure performed excellently as a photocatalyst for decomposing organic pollutions and generating hydrogen due to its better charge separation capacity after the light absorption.¹⁷⁶

In this chapter, the hydrogenated TiO₂ nanocrystals were prepared by hydrogenating the pure TiO₂ nanocrystals. A disordered amorphous layer was generated during the process. This layer was supposed to be beneficial to the charge transfer process. Low-resolution TEM and high-resolution TEM, XRD, Raman, FTIR, XPS, and ¹H-NMR were used to characterize the structure of the two TiO₂ nanocrystals. Obvious structural differences could be obtained and further analyzed. Electrodes were made by the pure TiO₂ nanocrystals and the hydrogenated TiO₂ nanocrystals to compare their battery performances, including discharge capacity, Coulombic efficiency, and rate performance. The hydrogenated TiO₂ nanocrystals showed better battery performances than the pure TiO₂ nanocrystals. The relationships between the structure and the battery performances were also studied.

3.2 Preparation

The pure TiO₂ nanocrystals were synthesized through a hydrothermal method. The hydrogenated TiO₂ nanocrystals were prepared by placing the pure TiO₂ nanocrystals in a sealed sample chamber under vacuum for 1 hour followed by hydrogenation under a 20.0 bar H₂ atmosphere at about 200 °C for 5 days. The experiment methods were described in Chapter 2 in detail.

3.3 Results and Discussions of Characterization

3.3.1 Low-Resolution TEM and High-Resolution TEM

Figure 3.1 shows the low-resolution TEM and high-resolution TEM of (A and B) the pure TiO₂ nanocrystals and (C and D) the hydrogenated TiO₂ nanocrystals. The low-resolution TEM (Figure 3.1 (A) and Figure 3.1 (C)) suggested that both samples had a similar average size around 10 nm and the sizes distributed well. The high-resolution TEM (Figure 3.1 (B) and Figure 3.1 (D)) provided a deeper understanding of the nanocrystals. The average crystal sizes of both samples were around 10 nm in diameter. The pure TiO₂ nanocrystals were highly crystallized throughout the whole particle, while the hydrogenated TiO₂ nanocrystals showed a crystalline core with a disordered amorphous shell whose thickness was around 0.4-1.0 nm.

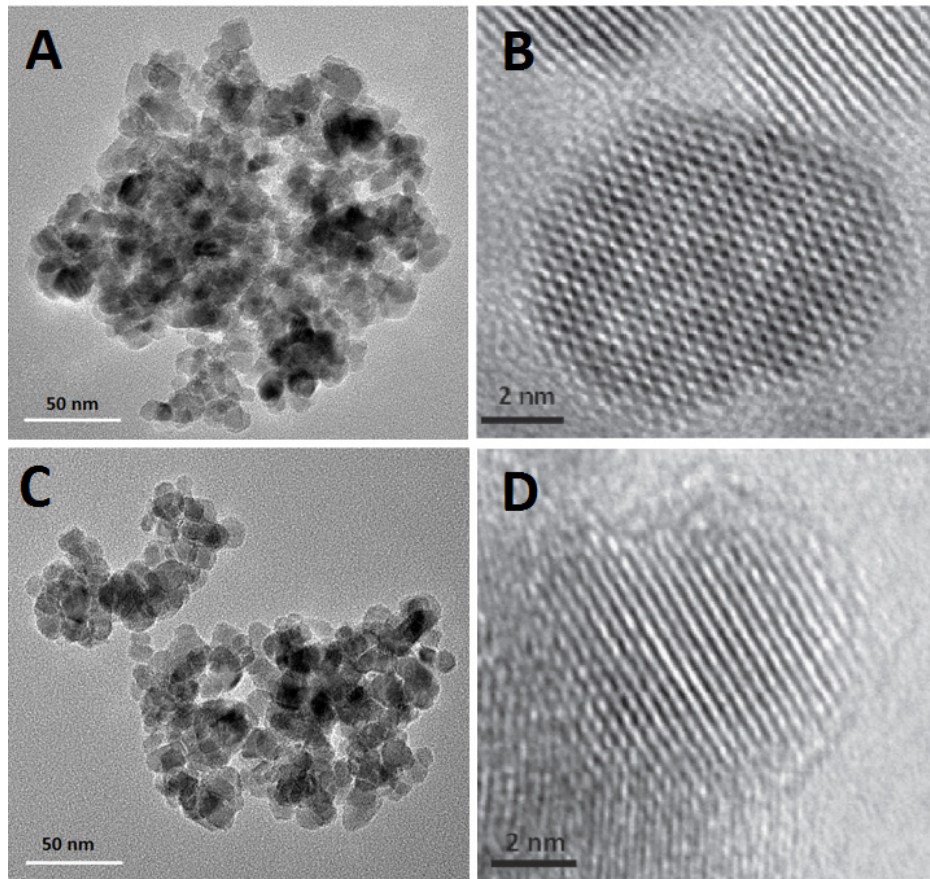


Figure 3.1. Low-resolution and high-resolution TEM images of (A and B) the pure TiO₂ nanocrystals and (C and D) the hydrogenated TiO₂ nanocrystals.

3.3.2 XRD

The XRD patterns of the pure TiO₂ nanocrystals and the hydrogenated TiO₂ nanocrystals are shown in Figure 3.2. The strong typical diffraction peaks of the pure TiO₂ nanocrystals and the hydrogenated TiO₂ nanocrystals indicated that both samples were anatase crystals. The changes in the plane spacing of various lattice planes of the hydrogenated TiO₂ nanocrystals could be obtained by subtracting and normalizing with

the plane spacing values of the bulk anatase TiO₂. The results can be seen in Figure 3.3. From the figure it was easy to find out that for the pure TiO₂ nanocrystals, the values of the plane spacing of planes (211), (204), (101), (200), and (220) were larger than the bulk anatase TiO₂, while the values of plane spacing of plane (116), (215), (001), and (105) were smaller than the bulk anatase TiO₂. After hydrogenation, all the values of the plane spacing decreased and they were smaller than those of the bulk anatase TiO₂. The absolute values of the plane spacing and the directional size can be found in Table 3.1. As mentioned before, the unit cell parameter a and c could be calculated through the relationship with adjacent planes. The changes of a , c , and volume v (Figure 3.4) of the pure TiO₂ nanocrystals and the hydrogenated TiO₂ nanocrystals were also calculated by subtracting and normalizing with the values of the bulk anatase TiO₂. These results are shown in Table 3.2. Compared with the bulk anatase TiO₂ (a : 3.7892 Å, c : 9.5370 Å, and volume v : 136.93 Å³), the unit cell parameter a of the pure TiO₂ nanocrystals was expanded 0.0385%, the unit cell parameter c was contracted 0.2321%, and the cell volume v was contracted 0.1534%. After hydrogenation, the unit cell parameter a contracted 0.1566% compared to bulk anatase TiO₂. The unit cell parameter c and cell volume v contracted further 0.1779% and 0.4901%, respectively. The unit cell parameter a of the hydrogenated black TiO₂ nanocrystals was contracted 0.1180%, the unit cell parameter c was contracted 0.4097%, and the cell volume v was contracted 0.6427% compared to bulk anatase TiO₂. Overall, after hydrogenation, the unit cell of TiO₂ contracted.

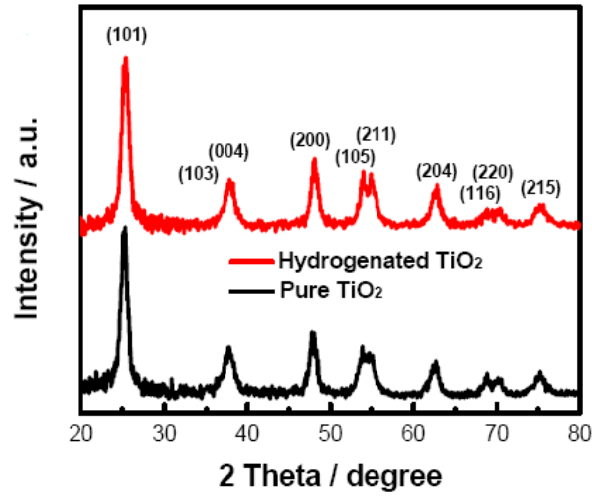


Figure 3.2. XRD patterns of the pure TiO_2 nanocrystals and the hydrogenated TiO_2 nanocrystals.

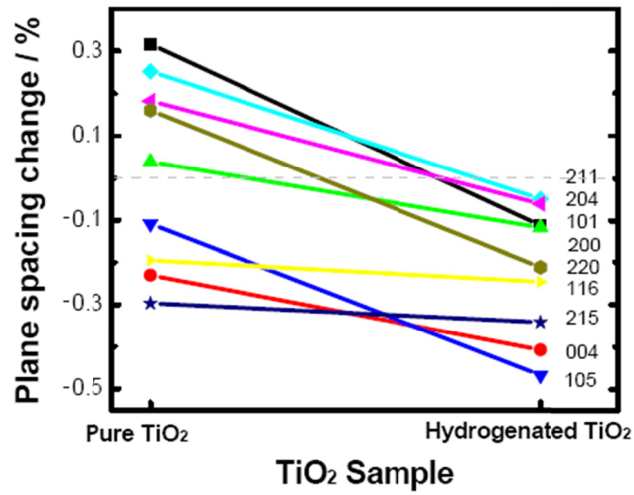


Figure 3.3. Changes in the plane spacing of various lattice planes in the pure TiO_2 nanocrystals and the hydrogenated TiO_2 nanocrystals.

Table 3.1. Size of the pure TiO₂ nanocrystals and the hydrogenated TiO₂ nanocrystals derived from XRD data.

Peak index	Angle		FWHM		Plane distance		Directional size	
	/degree		/degree		/Å		/Å	
	Pure ^a	HG ^b						
101	25.21	25.32	0.98	1.04	3.53254	3.51744	83.13096	78.35180
004	37.82	37.89	1.31	1.33	2.37872	2.37448	64.15308	63.20161
200	48.00	48.08	1.11	1.15	1.89533	1.89236	78.40433	75.70077
105	53.87	54.08	0.99	1.01	1.70184	1.69573	90.07959	88.37828
211	54.89	55.07	1.05	1.04	1.67261	1.66757	85.32144	86.21228
204	62.50	62.67	1.43	1.22	1.48601	1.48238	65.0333	76.29633
116	68.81	68.85	1.07	1.32	1.36433	1.36364	90.05787	73.01891
220	70.13	70.43	1.30	1.31	1.34185	1.33687	74.71894	74.28533
215	75.23	75.27	1.26	1.67	1.26304	1.26247	79.65742	60.11698

^aPure means the pure TiO₂ nanocrystals.

^bHG means the hydrogenated TiO₂ nanocrystals.

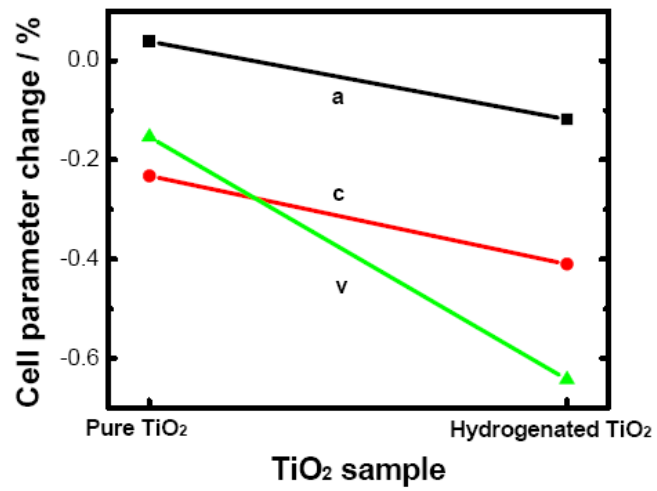


Figure 3.4. Changes in unit cell parameters a and c with unit cell volume v of the pure TiO₂ nanocrystals and the hydrogenated TiO₂ nanocrystals.

Table 3.2. Unit cell parameters of the pure TiO₂ nanocrystals and the hydrogenated TiO₂ nanocrystals.

	Cell parameter $a/\text{\AA}$	Cell parameter $c/\text{\AA}$	Cell volume $v/\text{\AA}^3$
Bulk TiO ₂	3.7892	9.5370	136.93
Pure TiO ₂	3.79066	9.51486	136.72
Hydrogenated TiO ₂	3.78473	9.49793	136.05

By using the Scherrer equation, the directional crystalline grain sizes were calculated. The values and figure are shown in Table 3.1 and Figure 3.5, respectively. For example, for the pure TiO₂ nanocrystals, the average length was 8.3 nm along (101), and 6.4 nm along (004). After hydrogenation, the average length of the TiO₂ nanocrystals along various directions decreased, except along (211) and (204) direction. The length along (204) increased from 6.503 nm to 7.630 nm and along (211) increased from 8.532 nm to 8.621 nm. Among these decreased lengths, the lengths along (215) and (116) decreased most, from 7.966 nm to 6.012 nm and from 9.006 nm to 7.302 nm, respectively. The length along (101), (105), and (220) decreased the least. These length changed along various directions suggested that the morphology and shape might have been changed dramatically after hydrogenation. In particular, the size of the crystalline phase of the hydrogenated TiO₂ nanocrystals contracted 5.75% (0.478 nm), 1.48% (0.095 nm), 3.44% (0.270 nm), 1.89% (0.170 nm), 18.92% (1.704 nm), 0.58% (0.043 nm), and 24.54% (1.955 nm) along the (101), (004), (200), (105), (116), (220), and (215) directions, respectively. As the hydrogenated TiO₂ nanocrystals showed the crystalline

anatase phase according to XRD spectrum, it could be deduced that from different directions the thickness of the disordered amorphous layer caused by hydrogenation ranged from ~ 0.1 nm to ~ 2 nm, which was roughly consistent with the high-resolution TEM results shown in Figure 3.1 (D).

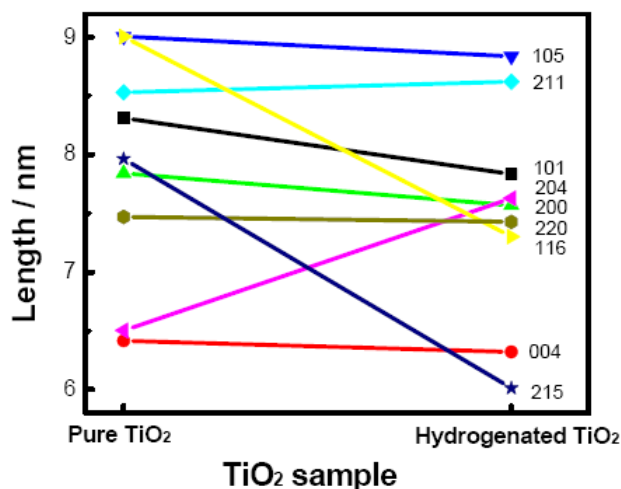


Figure 3.5. Average crystalline length along different directions of the pure TiO₂ nanocrystals and the hydrogenated TiO₂ nanocrystals.

3.3.3 Raman

The Raman spectra of the pure TiO₂ nanocrystals and the hydrogenated TiO₂ nanocrystals are shown in Figure 3.6.¹⁷⁶ Five Raman active modes (144.6 cm⁻¹, 199.1 cm⁻¹, 397.8 cm⁻¹, 519.2 cm⁻¹ (519 cm⁻¹ superimposed with 517 cm⁻¹), and 641.6 cm⁻¹) could be found in the spectrum of the pure TiO₂ nanocrystals. However, for the hydrogenated TiO₂ nanocrystals, besides the typical anatase peaks, there were additional peaks at 246.9 cm⁻¹, 294.2 cm⁻¹, 352.9 cm⁻¹, 690.1 cm⁻¹, 765.5 cm⁻¹, 849.1 cm⁻¹, and 938.3 cm⁻¹. As

these peaks did not belong to rutile, anatase or brookite, their generations indicated that the phase had been changed after hydrogenation. The disordered amorphous layer could be speculated to contribute to these peaks combining the results of the high-resolution TEM (Figure 3.1 (D)). Furthermore, the anatase peaks of the hydrogenated TiO₂ nanocrystals were broader than those of the pure TiO₂ nanocrystals. That could be attributed to the decrease of the particle size and it was consistent with the XRD results.

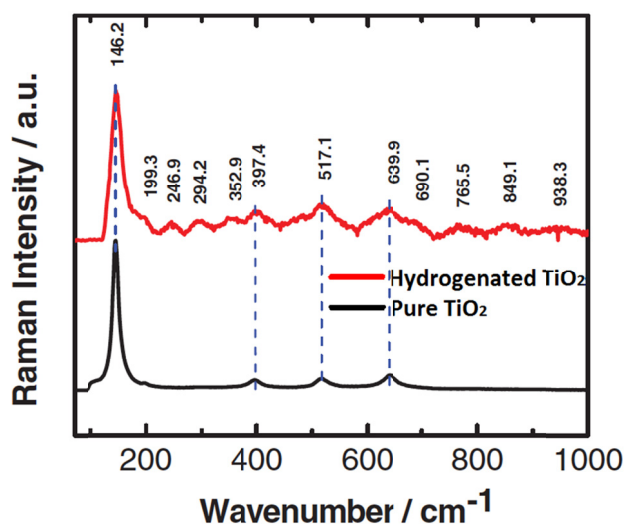


Figure 3.6. Raman spectra of the pure TiO₂ nanocrystals and the hydrogenated TiO₂ nanocrystals.¹⁷⁶

3.3.4 FTIR

Figure 3.7 shows the FTIR reflectance spectra of the pure TiO₂ nanocrystals and the hydrogenated TiO₂ nanocrystals. Both samples displayed a sharp and large absorption band at around 1000 cm⁻¹ due to the O-Ti-O vibrations in the TiO₂ lattice.¹⁷⁸ Besides,

they both had absorption band around 1640 cm^{-1} that could be attributed to the O-H bending of the molecularly physisorbed water from the opening environment.^{178,184,185} Near 3400 cm^{-1} , they showed OH absorption bands due to a bridging OH group possessing acidic properties.¹⁸⁶ The peaks at around 3730 cm^{-1} and 3640 cm^{-1} were resulted from the O-H stretching and wagging modes.¹⁸⁶ The hydrogenated TiO_2 nanocrystals possessed a weaker peak than the pure TiO_2 nanocrystals, which suggested that the hydrogen incorporated into the TiO_2 did not passivate a significant number of O dangling bonds. In addition, the broader peak of the hydrogenated TiO_2 nanocrystals suggested the OH groups experienced a more complex environment on the disordered surface than that of the pure TiO_2 nanocrystals.

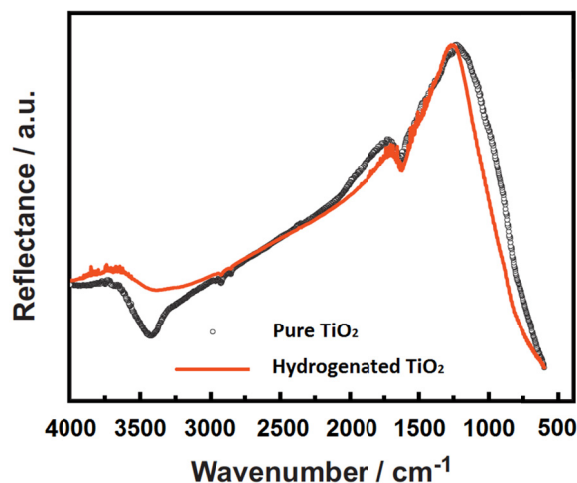


Figure 3.7. FTIR reflectance spectra of the pure TiO_2 nanocrystals and the hydrogenated TiO_2 nanocrystals.

3.3.5 XPS

The C *1s*, Ti *2p*, and O *1s* XPS of the pure TiO₂ nanocrystals and the hydrogenated TiO₂ nanocrystals are shown in Figure 3.8 (A), Figure 3.8 (B), and Figure 3.8 (C) respectively.¹⁷⁶ The binding energies from the samples were calibrated with respect to the C *1s* peak from the carbon tape at 284.6 eV. Both samples showed the C *1s* peak that could be attributed to the atmospheric carbon deposition on the surfaces of the samples during the measurement (Figure 3.8 (A)). The pure TiO₂ nanocrystals and the hydrogenated TiO₂ nanocrystals had the same Ti *2p* spectra (Figure 3.8 (B)), which meant that Ti atoms had the similar bonding environment after hydrogenation. TiO₂ were not doped with carbon or other impurities,¹⁷⁶ which further proved that no additional carbons were introduced by hydrogenation. The O *1s* XPS spectra are shown in Figure 3.8 (C). A big difference could be seen between the pure TiO₂ nanocrystals and the hydrogenated TiO₂ nanocrystals. The pure TiO₂ nanocrystals possessed one O *1s* peak at 530.0 eV, which was typical for TiO₂. However for the hydrogenated TiO₂ nanocrystals, two peaks (530.0 eV and 530.9 eV) were needed to fit the original data. One peak was at 530.0 eV, same as the pure TiO₂ nanocrystals. The other peaks was at 530.9 eV, which could be attributed to the Ti-OH species.¹⁷⁶ From the analysis, it was not difficult to know that the black color of the hydrogenated TiO₂ nanocrystals was not caused by possibly introduced carbon in the surface. It was caused by the disordered surface nature.

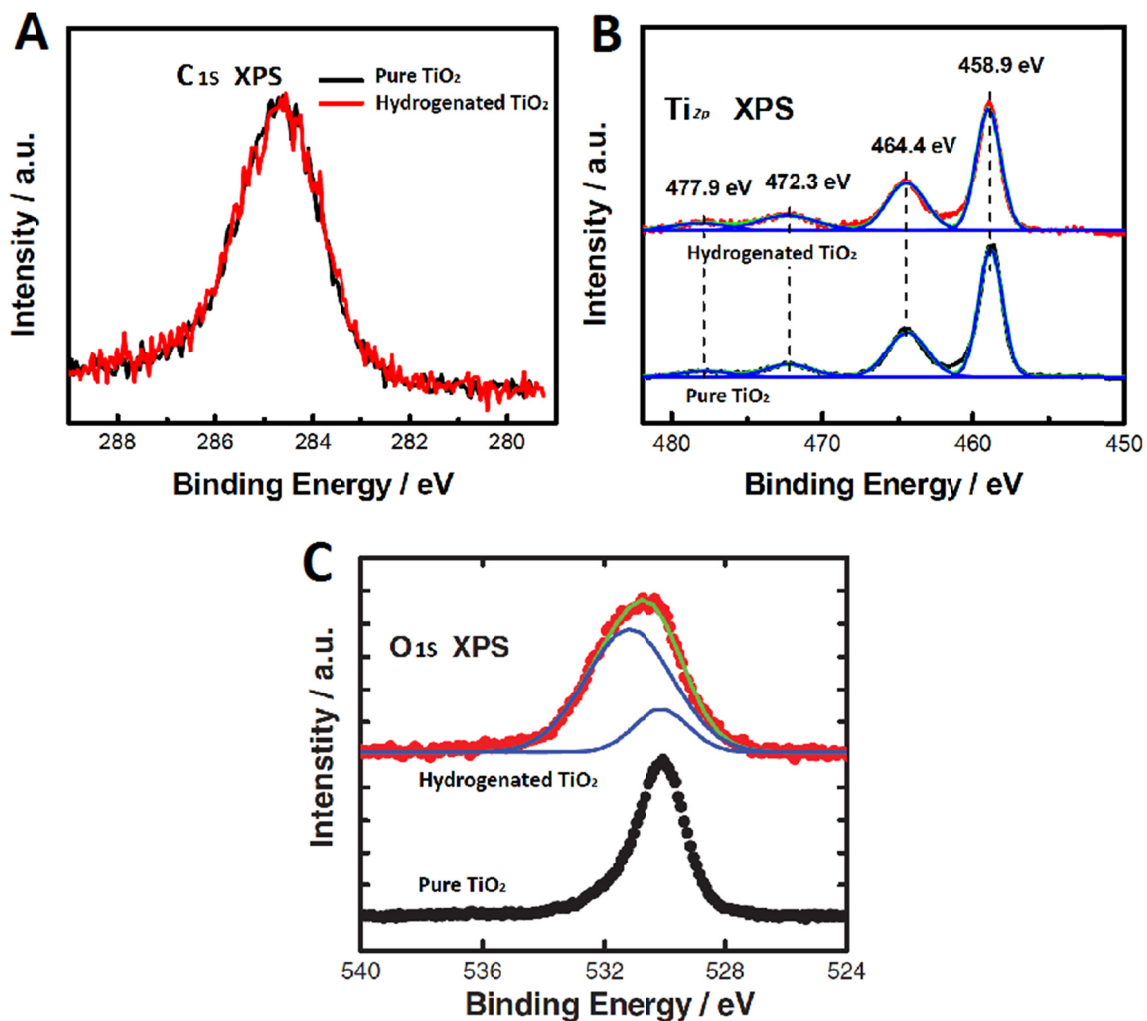


Figure 3.8.¹⁷⁶ (A) Ti 2p (B) C 1s (C) O 1s XPS of the pure TiO₂ nanocrystals and the hydrogenated TiO₂ nanocrystals.

3.4 Results and Discussions of Cycling Performances

3.4.1 Discharge Capacity

The variations of discharge capacity versus cycle number for the first 500 cycles of the pure TiO₂ nanocrystals and the hydrogenated TiO₂ nanocrystals are shown Figure 3.9

(A). The first cycle was conducted at C/25 rate, and the second cycle was conducted at C/5 rate, and the remaining cycles were conducted at 1C rate. The initial discharge capacity of the hydrogenated TiO₂ nanocrystals was 250 mAh/g at C/25 rate, 5.5% higher than the value of the pure TiO₂ nanocrystals (237 mAh/g). For the second cycle, the discharge capacity of the hydrogenated TiO₂ nanocrystals was 201 mAh/g at C/5 rate, 24.1% higher than that of the pure TiO₂ nanocrystals (162 mAh/g). For the third cycle, the discharge capacity of the hydrogenated TiO₂ nanocrystals was 159 mAh/g at 1C rate, 15.2% higher than that of the pure TiO₂ nanocrystals (138 mAh/g). The discharge capacity of the hydrogenated TiO₂ nanocrystals decreased more slowly than that of the pure TiO₂ nanocrystals in the first 150 cycles before leveling off. After 150 cycles, the discharge capacity of the hydrogenated TiO₂ nanocrystals was 133 mAh/g at 1C rate, 23.1% higher than that of the pure TiO₂ nanocrystals (108 mAh/g). By the end of 500 cycles, the discharge capacity of the hydrogenated TiO₂ nanocrystals was 105 mAh/g at 1C rate, 12.9% higher than that of the pure TiO₂ nanocrystals (93 mAh/g). Interestingly, for the first 10 cycles, the pure TiO₂ nanocrystals experienced a drastic fluctuation in the discharge capacity as shown in Figure 3.9 (B).

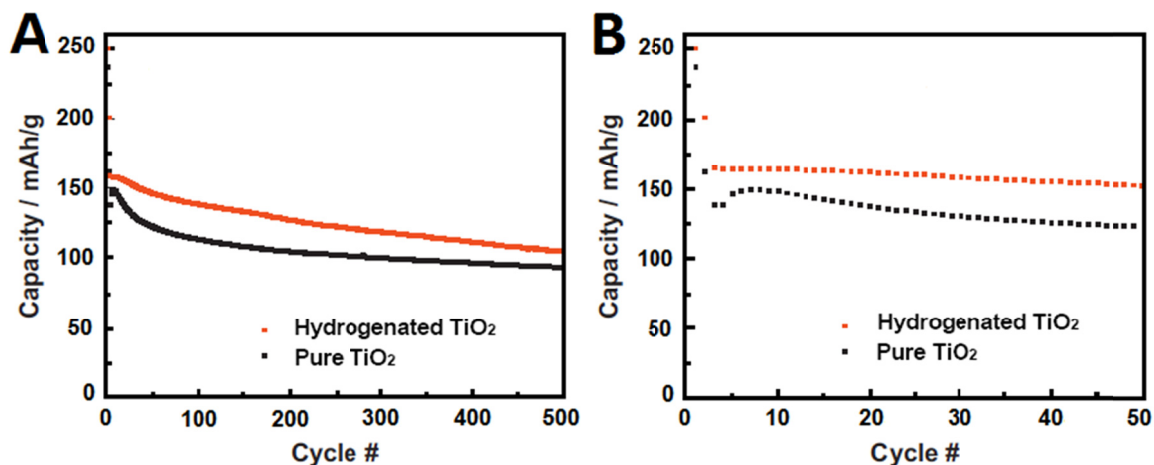


Figure 3.9. Variation of discharge capacity versus cycle number for (A) the first 500 cycles and (B) the first 50 cycles of the pure TiO₂ nanocrystals and the hydrogenated TiO₂ nanocrystals.

3.4.2 Coulombic Efficiency

The variations of the Coulombic efficiency along with the charge/discharge versus cycle number for the first 500 cycles of the pure TiO₂ nanocrystals and the hydrogenated TiO₂ nanocrystals are shown in Figure 3.10 (A) and Figure 3.10 (B), respectively. Both samples had a steady efficiency after around 50 cycles. A closer look at the first 20 cycles showed that the pure TiO₂ nanocrystals had a low Coulombic efficiency for the first cycle. Then the efficiency fluctuated in the next 3 cycles, and followed by a slight decrease in the next 16 cycles (Figure 3.10 (C)). As for the hydrogenated TiO₂ nanocrystals, the Coulombic efficiency was also low for the first cycle, but it did not undergo a fluctuation in the next cycles, instead, it increased in the next 4 cycles and remained steadily in the next 16 cycles (Figure 3.10 (D)). By the end of 500 cycles, the Coulombic efficiency of the pure TiO₂ nanocrystals was around 99.6% while the value of

the hydrogenated TiO_2 nanocrystals was 99.9%. Apparently, the hydrogenated TiO_2 nanocrystals performed better than the pure TiO_2 nanocrystals in terms of the Coulombic efficiency. The difference could be attributed to a better structural accommodation of the lithium-ions in the disordered amorphous layer of the hydrogenated TiO_2 nanocrystals during the charge/discharge processes.

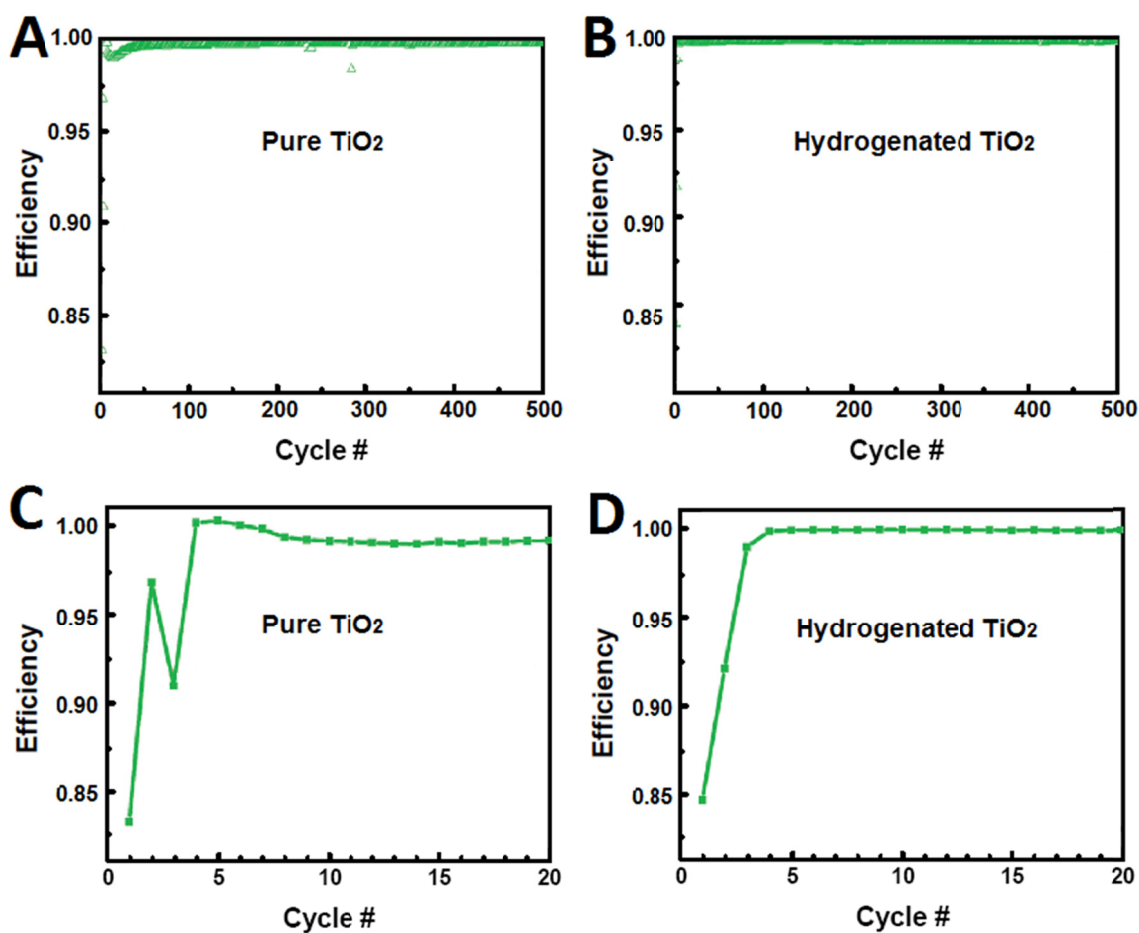


Figure 3.10. Variation of Coulombic efficiency along with the charge/discharge versus cycle number of the pure TiO_2 nanocrystals (A: the first 500 cycles; C: the first 20 cycles) and the hydrogenated TiO_2 nanocrystals (B: the first 500 cycles; D: the first 20 cycles).

3.4.3 Rate Performance

The rate performances of the pure TiO₂ nanocrystals and the hydrogenated TiO₂ nanocrystals are shown in Figure 3.11 and Table 3.3. For the first 18 cycles of the rate performance test, the charge and discharge rates were changed simultaneously, and for the following cycles only the charge rates were changed while the discharge rate was kept at 1C. For both samples, as the charge rate increased, the discharge capacity decreased accordingly. For example, for the first 18 cycles, the capacity of the pure TiO₂ nanocrystals was 144 mAh/g at 1C rate, 65 mAh/g at 10C rate, and 7 mAh/g at 50C rate. As for the hydrogenated TiO₂ nanocrystals, the capacity was 150 mAh/g at 1C rate, 79 mAh/g at 10C rate, and 16 mAh/g at 50C rate. Apparently, the hydrogenated TiO₂ nanocrystals possessed larger capacity than the pure TiO₂ nanocrystals at the same rate. For the next 18 cycles, the discharge capacity of both samples increased compared to the case where both the charge/discharge rates were the same. Except for 1C rate, the hydrogenated TiO₂ nanocrystals performed better than the pure TiO₂ nanocrystals in this situation. The capacity of the pure TiO₂ nanocrystals was 157 mAh/g at 1C rate, 105 mAh/g at 10C rate, and 35 mAh/g at 50C rate. As for the hydrogenated TiO₂ nanocrystals, the capacity was 155 mAh/g at 1C rate, 127 mAh/g at 10C rate, and 16 mAh/g at 56C rate. Obviously, the hydrogenated TiO₂ had better performance at high rates than the pure TiO₂ nanocrystals, which meant that the disordered amorphous layer acted positively for the improvement of rate performance. This improvement might have been possibly caused by the lower energy barrier of the transport of lithium-ions during the charge/discharge processes in the disordered amorphous surface.¹⁸⁷ Similar result was

found by previous work of the higher lithium-ion capacity and capacity retention of the amorphous TiO₂ nanotubes than those of the crystalline TiO₂ nanotubes.¹⁸⁸

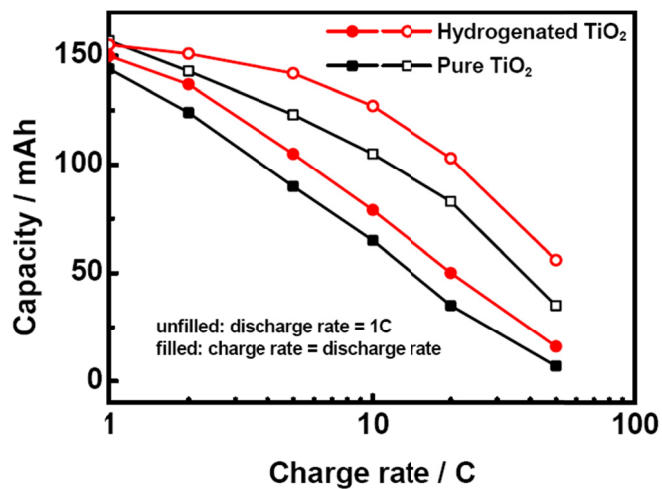


Figure 3.11. Comparison of the discharge capacities of the pure TiO₂ nanocrystals and the hydrogenated TiO₂ nanocrystals at various charge rates.

Table 3.3. Rate performance of the pure TiO₂ nanocrystals and the hydrogenated TiO₂ nanocrystals at various charge rates.

		Sample	1C	2C	5C	10C	20C	50C
Discharge capacity/ mAh/g	1-18 cycles	Pure ^a	144	124	90	65	35	7
	(Symmetric ^b)	HG ^c	150	137	105	79	50	16
	19-36 cycles	Pure ^a	157	143	123	105	83	35
	(Asymmetric ^d)	HG ^c	155	151	142	127	103	56

^aPure means the pure TiO₂ nanocrystals.

^bSymmetric means charge rate equals discharge rate.

^cHG means the hydrogenated TiO₂ nanocrystals.

^dAsymmetric means discharge rate equals 1C.

3.4.4 Analysis of Galvanostatic Charge/Discharge Profiles

The galvanostatic charge/discharge profiles for the first cycle at C/25 rate, 35th cycle at 1 C rate, and 100th cycle at 1C rate for the electrode made of the pure TiO₂ nanocrystals and the hydrogenated TiO₂ nanocrystals are shown in Figure 3.12 (A) and Figure 3.12 (B), respectively. The hydrogenated TiO₂ nanocrystals were not only having the higher charge/discharge capacity than the pure TiO₂ nanocrystals in these cycles, but also possessing larger charge/discharge plateaus and smaller potential differences between the charge and discharge cycle. The average potential difference between the charge and discharge cycle of the hydrogenated TiO₂ nanocrystals was about 0.11 V, 42.1% smaller than that of the pure TiO₂ nanocrystals (0.19 V). The smaller potential differences indicated the smoother charge transfer in the disordered amorphous layer, which meant that the charge transfer resistance was decreased. It might have been caused by the weaker chemical bonding between the transferred charge and the host matrix in the

hydrogenated TiO₂ nanocrystals. The larger charge/discharge plateaus suggested the bulk intercalation ability increased, which might have been caused by the larger charge transfer depth. These results indicated that the disordered amorphous layer benefited the charge transfer in the nanocrystals.

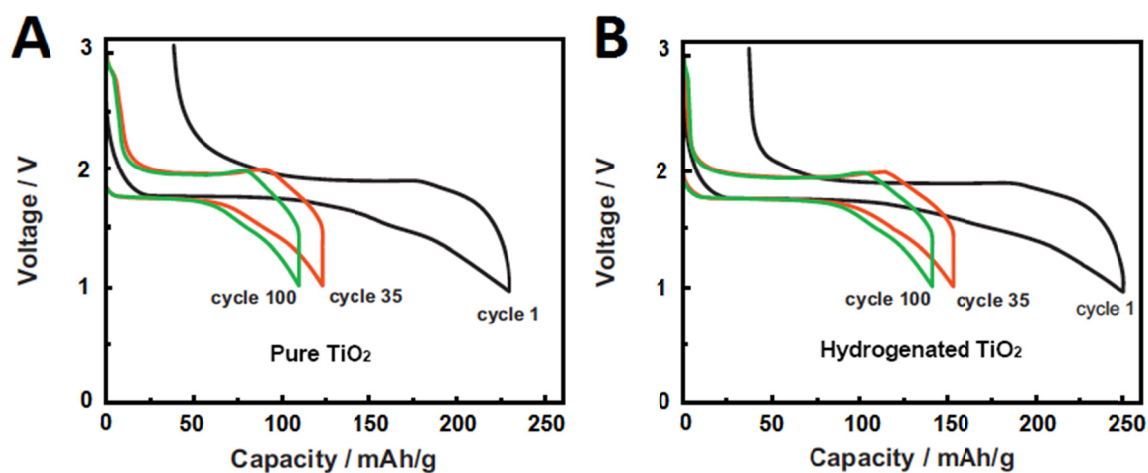


Figure 3.12. Galvanostatic charge/discharge profiles for the first cycle at C/25 rate, 35th cycle at 1 C rate, and 100th cycle at 1C rate for the electrode made of (A) the pure TiO₂ nanocrystals and (B) the hydrogenated TiO₂ nanocrystals.

As for the high-rate performance, Figure 3.13 (A) and Figure 3.13 (B) showed the galvanostatic charge/discharge profiles at various charge rates for the electrode made of the pure TiO₂ nanocrystals and the hydrogenated TiO₂ nanocrystals, respectively. Same as low rate performance, in general, the hydrogenated TiO₂ nanocrystals showed higher discharge capacity than the pure TiO₂ nanocrystals at the same rate. Besides, the hydrogenated TiO₂ nanocrystals had larger charge/discharge plateaus between the charge/discharge cycles at each charge rate, which indicated that charge transferred more

smoothly in the hydrogenated TiO₂ nanocrystals than in the pure TiO₂ nanocrystals. The special disordered amorphous surface structure of the hydrogenated TiO₂ nanocrystals could be the reason to explain this phenomenon.

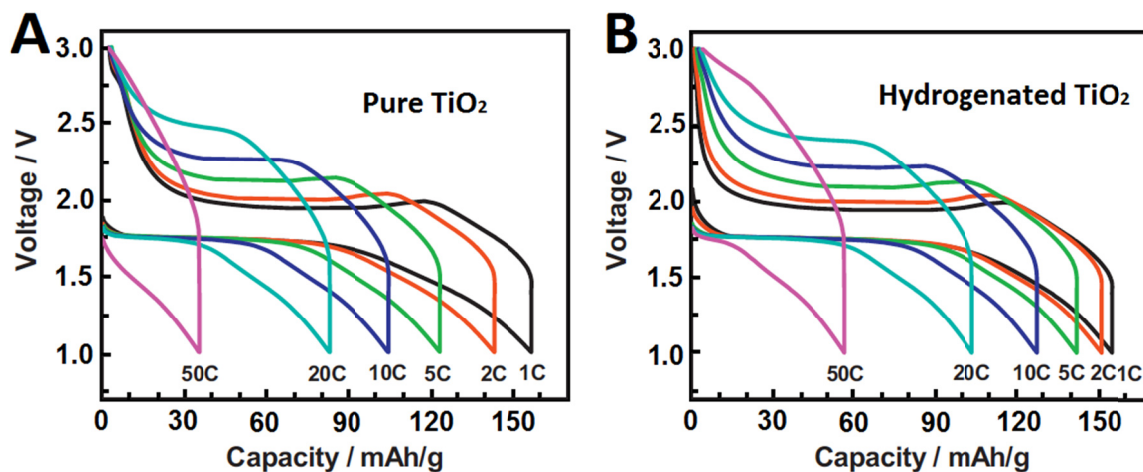


Figure 3.13. Galvanostatic charge/discharge profiles at various charge rates (discharge rate = 1C) for the electrode made of (A) the pure TiO₂ nanocrystals and (B) the hydrogenated TiO₂ nanocrystals.

3.5 Relationships between Structure and Battery Performances

As illustrated in Figure 3.14, after hydrogenation, a disordered amorphous layer outside the crystalline core was generated. Furthermore, although both samples displayed almost a same particle size according to the TEM images (Figure 3.1), the crystalline domain of the hydrogenated TiO₂ nanocrystals contracted and the thickness of the disordered amorphous layer was around 0.1-2 nm according to XRD analysis. These results were agreed with the Raman spectra (Figure 3.6). XPS (Figure 3.8) further

concluded that the black color of the hydrogenated TiO_2 nanocrystals was caused by the disordered surface nature. It was not resulted from the possibly introduced carbon in the surface. Both samples were used as an electrode material in half-cells and their cycling performances were tested. The hydrogenated TiO_2 nanocrystals performed better than the pure TiO_2 nanocrystals in terms of discharge capacity, Coulombic efficiency, and rate performance, which indicated that the disordered amorphous layer could have facilitated the charge transfer and the capacity retention of the electrodes.

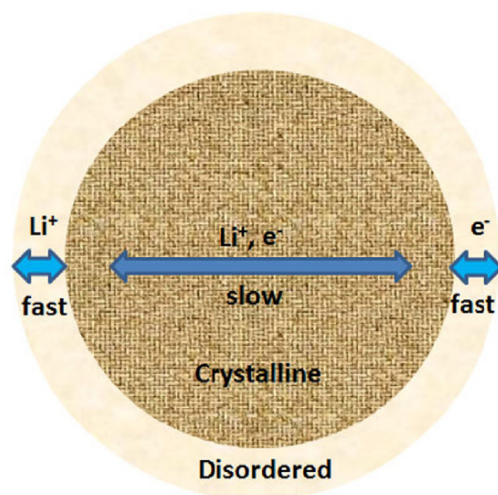


Figure 3.14. Illustration of the hydrogenated TiO_2 layer to facilitate the fast charge transfer and the capacity retention.

3.5.1 Structural Tolerance

As can be seen in Figure 3.1 (D), the hydrogenated TiO_2 nanocrystals provided a large rough surface, which might have edges and corners on the atomic level that were

more favorable for the ion adsorption due to the possible surface dangling bonding available. Furthermore, for the hydrogenated TiO₂ nanocrystals, as the surface was disordered, the lattice was poorly defined with the thermodynamically metastable energetic states as compared to the pure TiO₂ nanocrystals. This would enhance the penetration of lithium-ions into the lattice of the host matrix, resulting in lower lithium-ion transport resistance. It was consistent with the cycling test results. Considering the structure rigidity, as the pure TiO₂ nanocrystals had an ordered rigid surface, it might not have provided a good interface to accommodate lithium-ions, causing a low discharge capacity (Figure 3.9 and Figure 3.12 (A)), a variable Coulombic efficiency (Figure 3.10 (C)), and a poor rate performance (Figure 3.11 and Figure 3.13 (A)). Also, due to the large structural distortion tolerance, the hydrogenated TiO₂ nanocrystals might have accommodated lithium-ions much more easily, providing a high discharge capacity (Figure 3.9 and Figure 3.12 (B)), a stable efficiency (Figure 3.10 (D)), and a good rate performance (Figure 3.11 and Figure 3.13 (B)).

As mentioned before, for anatase TiO₂ used as an anode material for the lithium-ion battery, the unit volume will increase around 4% as the *c*-axis decreases and the *b*-axis increases by symmetry change, which causes a rapid capacity fade.¹⁵⁰ Thus, $x = 0.5$ is considered to be the maximum intercalation value for anatase.^{113,114} For the hydrogenated TiO₂ nanocrystals, it showed great improvement of discharge capacity as well as Coulombic efficiency and rate performance compared to the pure TiO₂ nanocrystals, although it did not perform beyond the limitation of 0.5. According to the previous XRD analysis, compared with bulk TiO₂, the unit cell parameter *a*, *c*, and cell volume *v* of the

hydrogenated TiO₂ nanocrystals reduced 0.1180% to 3.78473 Å, 0.4100% to 9.49793 Å, and 0.6427% to 136.05 Å³, respectively. The large structural distortion due to the increase of the unit cell volume and the unit cell was thus relieved to some extent due to the structural alteration in the hydrogenated TiO₂ nanocrystals during the hydrogenation process. This kind of release in stress might have caused better structural stability of the TiO₂ host for the intercalation/extraction processes of lithium-ions. Thus, it could be considered to be another reason for better cycling performances.

3.5.2 Hydrogen Mobility

3.5.2.1 FTIR

In order to further understand why the disordered amorphous layer of the hydrogenated TiO₂ nanocrystals helped the transport of lithium-ions in the host matrix, a deeper look at the FTIR is needed (Figure 3.7). As discussed before, the hydrogen incorporated into the TiO₂ did not passivate a significant number of O dangling bonds. The hydrogenated TiO₂ nanocrystals possessed a more complex environment of OH (broader peak around 3400 cm⁻¹) on the disordered surface than that of the pure TiO₂ nanocrystals. In addition to the inhomogeneous effect mentioned above, the homogeneous (lifetime) effect due to the rapid exchange among sites might have also resulted in the linewidth difference. Such exchange could have provided much faster hydrogenation diffusion rate from surface to the bulk. As the exchange of protons and lithium-ions was observed in the lithium intercalation materials,^{189,190} the faster hydrogen

diffusion rates suggested that the diffusion rate of lithium-ions was also faster, as the hydrogen could be more easily replaced by the lithium-ions in the hydrogenated TiO₂ nanocrystals than in the pure TiO₂ nanocrystals. Thus, the hydrogenated TiO₂ nanocrystals were supposed to have better cycling performances than the pure TiO₂ nanocrystals. The speculation was consistent with the results of cycling performance tests.

3.5.2.2 ¹H-NMR

The high mobility of the hydrogen in the hydrogenated TiO₂ nanocrystals was also verified by ¹H-NMR study. The ¹H-NMR spectra of the pure TiO₂ nanocrystals and the hydrogenated TiO₂ nanocrystals are shown in Figure 3.15. Both samples showed a large peak at +5.7 ppm. The hydrogenated TiO₂ nanocrystals displayed it a little broader than the pure TiO₂ nanocrystals, which might have been caused by the incorporation of H at bridging sites at the rutile-like phase produced during the hydrogenation process, or due to the bridging sites located on different crystallographic planes on the surface. Furthermore, the hydrogenated TiO₂ nanocrystals possessed two additional narrow peaks at +0.73 ppm and -0.03 ppm. These two peaks were small and sharp, which suggested that the amounts of hydrogen of these kinds were low and, in addition, there were dynamic exchanges between ¹H (fast motions) in different environments. The rapid isotropic diffusion and rapid exchange between different proton environments could be examples of such dynamic exchange mechanisms.^{191,192} These two peaks were associated with H located in the disordered amorphous layer after hydrogenation. Thus, the presence

of hydrogenated disordered amorphous layer of the TiO_2 nanocrystals might have provided an explanation for the enhanced hydrogen mobility. The higher hydrogen mobility in the hydrogenated TiO_2 nanocrystals suggested that the mobility of lithium-ions was higher compared to the pure TiO_2 nanocrystals, as the hydrogen could be easily replaced by the lithium-ions. The analysis was consistent with the FTIR spectra, and it was further proved by the results of cycling performance tests.

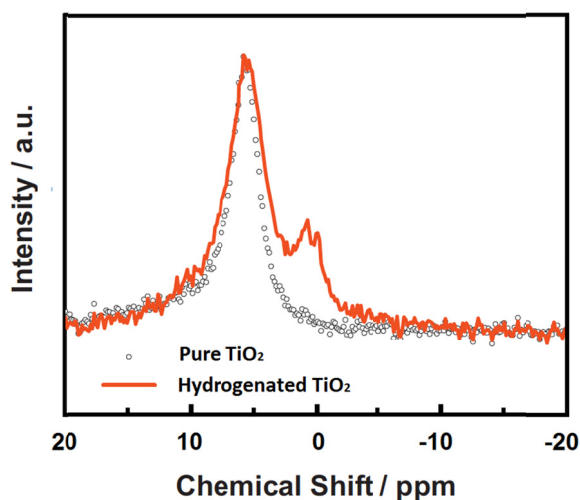


Figure 3.15. ^1H magic-angle spinning solid state NMR spectra of the pure TiO_2 nanocrystals and the hydrogenated TiO_2 nanocrystals.

3.6 Summary

In summary, hydrogenation was used as a modification method to improve the battery performances of TiO_2 nanocrystals. After hydrogenation, the pure TiO_2 nanocrystals were converted into the hydrogenated TiO_2 nanocrystals. A disordered

amorphous layer outside the crystalline core was generated. Compared with the pure TiO₂ nanocrystals, the hydrogenated TiO₂ nanocrystals displayed a better discharge capacity (105 mAh/g after 500 cycles), a near 100% Coulombic efficiency without noticeable degradation, and an improved high-rate performance.

From the analysis of the galvanostatic charge/discharge profiles, it indicated that the disordered amorphous layer of the hydrogenated TiO₂ nanocrystals possessed a weaker chemical bonding between the transferred charge and host matrix. It also provided a larger charge transfer depth. The large structural tolerance of the hydrogenated TiO₂ nanocrystals could be one possible explanation. In addition, the faster ion exchange and hydrogen mobility in the disordered amorphous layer might have provided another explanation of better charge transfer efficiency and capacity retention efficiency. This concept of the surface-disordered structure on the outer layer of the crystalline electrode materials provides an alternative solution in searching for high performance electrode materials.

CHAPTER 4
DESIGN, PREPARATION AND PROPERTIES OF THE VACUUM-TREATED
TITANIUM DIOXIDE NANOCRYSTALS

*(The main content of this chapter was published in Nano Letters, 2013, 13, 5289-5296
entitled “Built-in electric field-assisted surface-amorphized nanocrystals for
high-rate lithium-ion battery” as research article.)*

4.1 Introduction

Anatase TiO₂ nanocrystals were also used as a kind of starting material here. Shin et al.¹¹² synthesized the oxygen-deficient TiO_{2-δ} nanoparticles that displayed a high-rate capacity of lithium storage prepared by hydrogen reduction. They proposed that the well-balanced Li⁺/e⁻ transport was the key factor for the improved performances.¹¹² The formation of the oxygen vacancies played an important role in increasing the electronic conductivity that benefited charge transfer then improved the battery performances.¹¹² Aschauer and Selloni¹⁹³ recently suggested that the subsurface oxygen vacancies on the reduced anatase were the favorable adsorption sites for hydrogen atoms from density functional theory calculations. Oxygen vacancies can be created by higher-temperature heating and/or ultra-higher vacuum, high-energy particle bombardment,¹⁹⁴ γ-ray¹⁹⁵, or ultraviolet irradiation.¹⁰²

In this chapter, the pure TiO₂ nanocrystals went through a vacuum treatment to convert to the vacuum-treated TiO₂ nanocrystals, expecting to have oxygen vacancies in the outer layer of TiO₂ nanocrystals. Low-resolution TEM and high-resolution TEM, XRD, Raman, FTIR, ESR, and XPS were used to characterize the structure of the pure TiO₂ nanocrystals and the vacuum-treated TiO₂ nanocrystals. Electrodes were made by both samples to compare their discharge capacity, Coulombic efficiency, and rate performance. The vacuum-treated TiO₂ nanocrystals showed better battery performances than the pure TiO₂ nanocrystals. EIS was used to analyze the electrochemical processes inside the cell. The relationships between the structure and the battery performances were also studied.

4.2 Preparation

The pure TiO₂ nanocrystals were synthesized through a hydrothermal method. The vacuum-treated TiO₂ nanocrystals were prepared by placing the pure TiO₂ nanocrystals in a vacuum chamber at 500 °C for 4 hours. The ramping and cooling rates of temperature were 10 °C /min. The experiment methods were described in Chapter 2 in detail.

4.3 Results and Discussions of Characterization

4.3.1 Low-Resolution TEM and High-Resolution TEM

The low-resolution, high-resolution TEM, and selected area electron diffraction (SAED) patterns of the pure TiO₂ nanocrystals and the vacuum-treated TiO₂ nanocrystals are shown in Figure 4.1. The low-resolution TEM images showed that both samples had a similar size around 10 nm (Figure 4.1 (A) and Figure 4.1 (D)). In addition, the aggregation and overlap could be observed. The high-resolution TEM images provided a deeper understanding of the nanocrystals (Figure 4.1 (B) and Figure 4.1 (E)). The pure TiO₂ nanocrystals were highly crystallized throughout the whole particle, while the vacuum-treated TiO₂ nanocrystals showed a crystalline core with an amorphous shell that was around 1-2 nm. The SAED pattern of the pure TiO₂ nanocrystals showed clear anatase diffraction rings made of clean diffraction dots (Figure 4.1 (C)), suggesting that the pure TiO₂ nanocrystals were highly crystallized. As for the vacuum-treated TiO₂ nanocrystals, there was a thick and milky diffraction background besides the anatase diffraction rings (Figure 4.1 (D)), indicating that the vacuum-treated TiO₂ nanocrystals probably contained amorphous or disordered phases.^{196,197} The result was consistent with the high-resolution TEM observation (Figure 4.1 (E)).

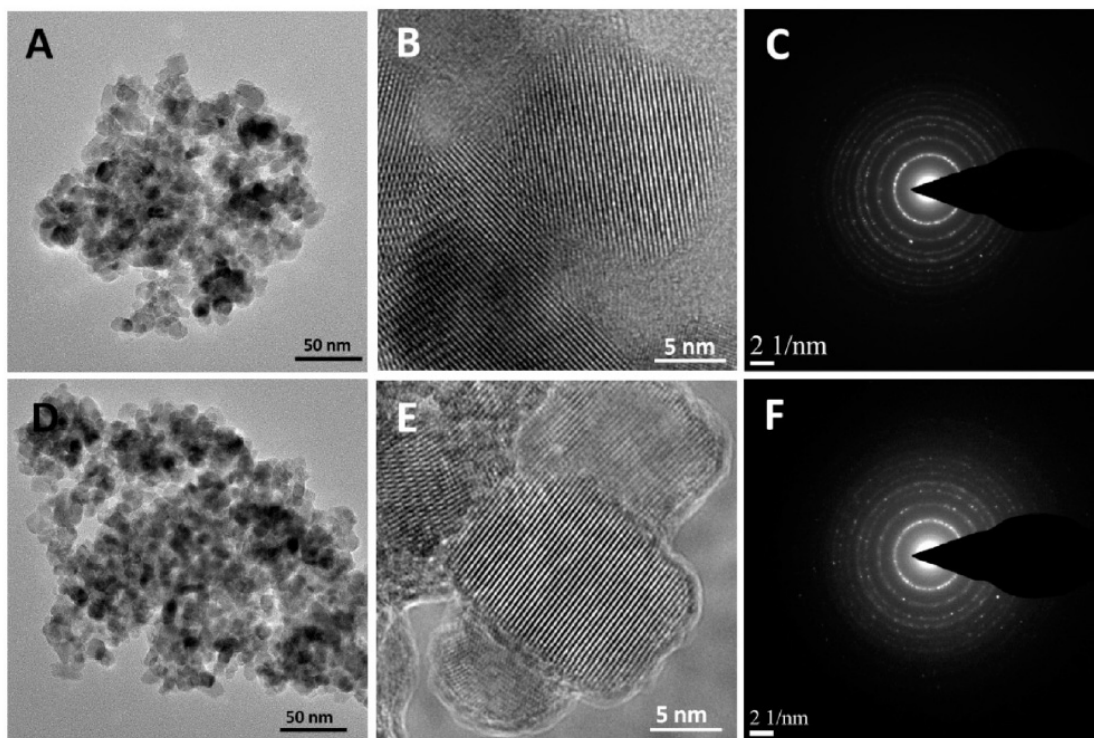


Figure 4.1. Low-resolution, high-resolution TEM, and SAED patterns of (A–C) the pure TiO₂ nanocrystals and (D–F) the vacuum-treated TiO₂ nanocrystals.

4.3.2 XRD

The XRD patterns of the pure TiO₂ nanocrystals and the vacuum-treated TiO₂ nanocrystals are shown in Figure 4.2. The strong typical diffraction peaks of both samples indicated that they were anatase crystals. The directional crystalline grain sizes were calculated by the Scherrer equation. Both samples had a particle size around 10 nm. That meant after vacuum-treatment, there was not much change of the main phase and the size.

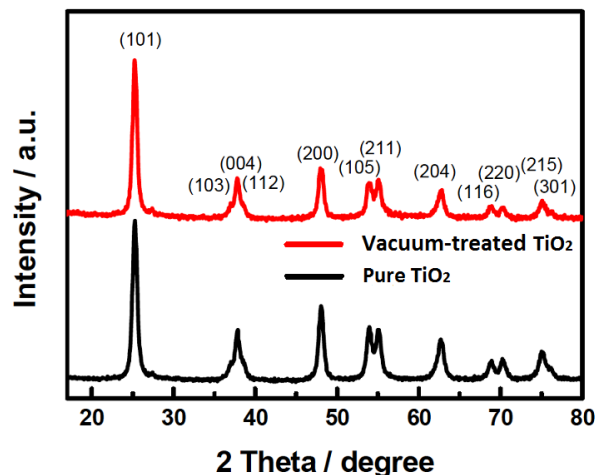


Figure 4.2. XRD patterns of the pure TiO₂ nanocrystals and the vacuum-treated TiO₂ nanocrystals.

4.3.3 Raman

The Raman spectra of the pure TiO₂ nanocrystals and the vacuum-treated TiO₂ nanocrystals are shown in Figure 4.3. A big difference could be seen between the two samples. For the pure TiO₂ nanocrystals, as discussed before, five Raman active modes could be found in the spectrum of the pure TiO₂ nanocrystals. However, for the vacuum-treated TiO₂ nanocrystals, it showed only a weak peak at around 147.9 cm⁻¹ (E_g) and a large luminescence background that suggested an amorphous phase might have been generated by the vacuum treatment. As the XRD patterns of the vacuum-treated TiO₂ nanocrystals showed that they were crystals, it could be deduced that the amorphous phase only appeared in the outer layer, as the Raman was more sensitive to the surface structure than the XRD.^{176,198,199} It complied with the analysis of the high-resolution TEM image of the vacuum-treated TiO₂ nanocrystals (Figure 4.1 (E)).

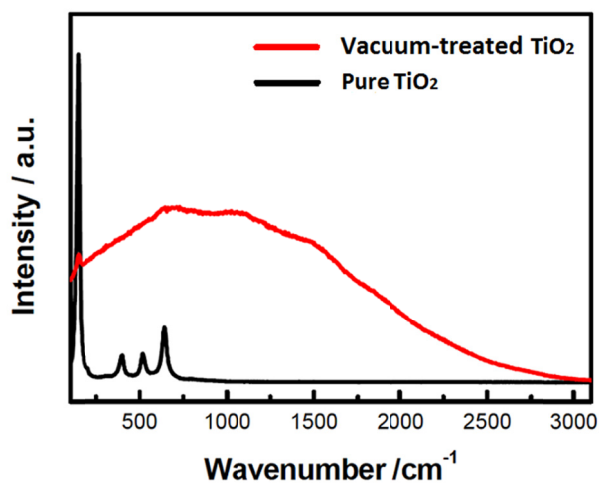


Figure 4.3. Raman spectra of the pure TiO₂ nanocrystals and the vacuum-treated TiO₂ nanocrystals.

4.3.4 FTIR

FTIR was used to check if there were any organic residues or any contaminations during the process of the vacuum treatment of the samples. Figure 4.4 shows the FTIR reflectance spectra of the pure TiO₂ nanocrystals and the vacuum-treated TiO₂ nanocrystals. Both samples displayed a similar spectrum. They had a sharp and large peak below 1000 cm⁻¹ due to the O-Ti-O vibrations in the TiO₂ lattice, an absorption band around 1640 cm⁻¹ that could be attributed to the O-H bending of the molecularly physisorbed water from the opening environment, as well as a broad peak OH absorption from 3000 cm⁻¹ to 3500 cm⁻¹.^{178,184-186} A careful observation suggested that the OH absorption band of the pure TiO₂ nanocrystals was larger than the vacuum-treated TiO₂ nanocrystals, which indicated a slight change of the surface of the TiO₂ nanocrystals after

vacuum-treatment. The FTIR proved that both samples were free of possible contaminations during these treatments.

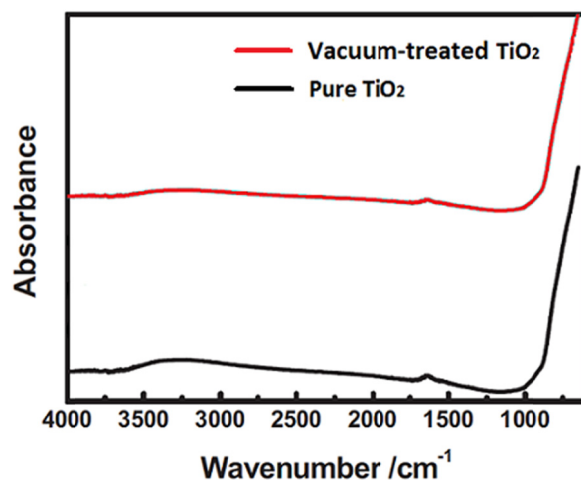


Figure 4.4. FTIR reflectance spectra of the pure TiO₂ nanocrystals and the vacuum-treated TiO₂ nanocrystals.

4.3.5 ESR

In order to check whether the oxygen vacancies were successfully created by the vacuum treatment, ESR measurement was performed for the pure TiO₂ nanocrystals and the vacuum-treated TiO₂ nanocrystals (Figure 4.5). For the pure TiO₂ nanocrystals, there were no signals in the spectrum, while for the vacuum-treated TiO₂ nanocrystals, strong signal at $g = 2.004$ could be found. The signal could be possibly assigned to the electrons trapped on the oxygen vacancies, which meant that the oxygen vacancies were successfully created.²⁰⁰ It is known that oxygen vacancies are normally created under an

ultrahigh vacuum environment at a high temperature, normally above 600 °C.²⁰¹ In our experiments, oxygen vacancies were created under a relatively low vacuum level (1-2 mTorr) and a low temperature (500 °C). It could be ascribed to the reduction of energies required to remove the oxygen from the lattice by nanoscale thermodynamic effect.^{109,202}

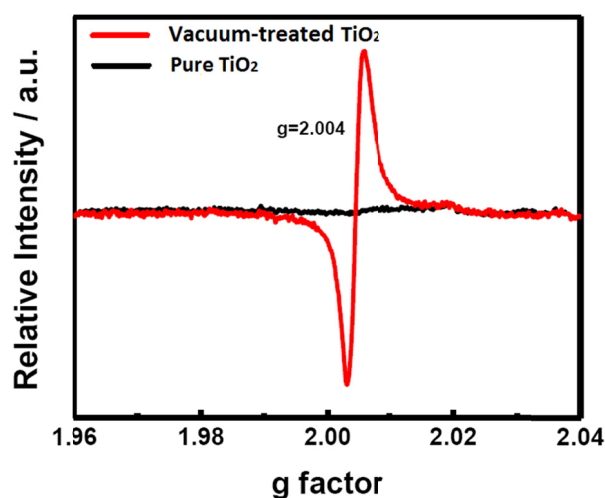
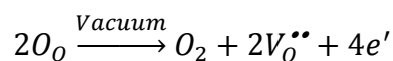


Figure 4.5. ESR spectra of the pure TiO₂ nanocrystals and the vacuum-treated TiO₂ nanocrystals.

Using the Kröger-Vink nomenclature, the formation of the oxygen vacancies under the vacuum process can be expressed as follows:



where O_o and $V_o^{\bullet\bullet}$ represent lattice oxygen and oxygen vacancy, respectively.

4.3.6 XPS

The C *1s*, XPS survey, Ti *2p*, and O *1s* of the pure TiO₂ nanocrystals and the vacuum-treated TiO₂ nanocrystals are shown in Figure 4.6 (A), Figure 4.6 (B), Figure 4.6 (C), and Figure 4.6 (D), respectively. The binding energies from the samples were calibrated with respect to C *1s* peak at 284.6 eV. Both samples showed the C *1s* peak that could be attributed to the atmospheric carbon deposition on the surfaces of the samples during the measurement (Figure 4.6 (A)). The XPS survey showed that both samples had no additional species (Figure 4.6 (B)), which indicated that there was no contamination introduced during the sample preparation process. As for Ti *2p* (Figure 4.6 (C)), the two samples did not have much difference. Both of them showed the typical Ti⁴⁺ features with Ti *2p*_{3/2} peak at around 459.0 eV and Ti *2p*_{1/2} peak centered at around 464.4 eV.^{176,203-205} For both samples, there was no Ti³⁺ peak (at around 457.0 eV), which indicated that the Ti³⁺ defect did not form in these preparation processes. The O *1s* core-level XPS spectra of both samples were quite similar as shown in Figure 4.6 (D). There was a peak around 530.5 eV that could be attributed to the O²⁻ ions in the O-Ti-O lattice, and the OH contents of the two samples could be generally ignored.^{176,204,205} The vacuum treatment did not change the chemical bonding environment of Ti *2p* and O *1s*. The location of the oxygen vacancies was more likely in the amorphous outer layer when considering the highly crystallized phases were almost identical. The large structural alternation was observed in the outer layer of the vacuum-treated TiO₂ nanocrystals. The formation of the amorphous phases could be attributed to the lattice relaxation or

reorganization after the possible formation of the oxygen vacancies during the vacuum treatment under a high temperature.¹⁹⁹

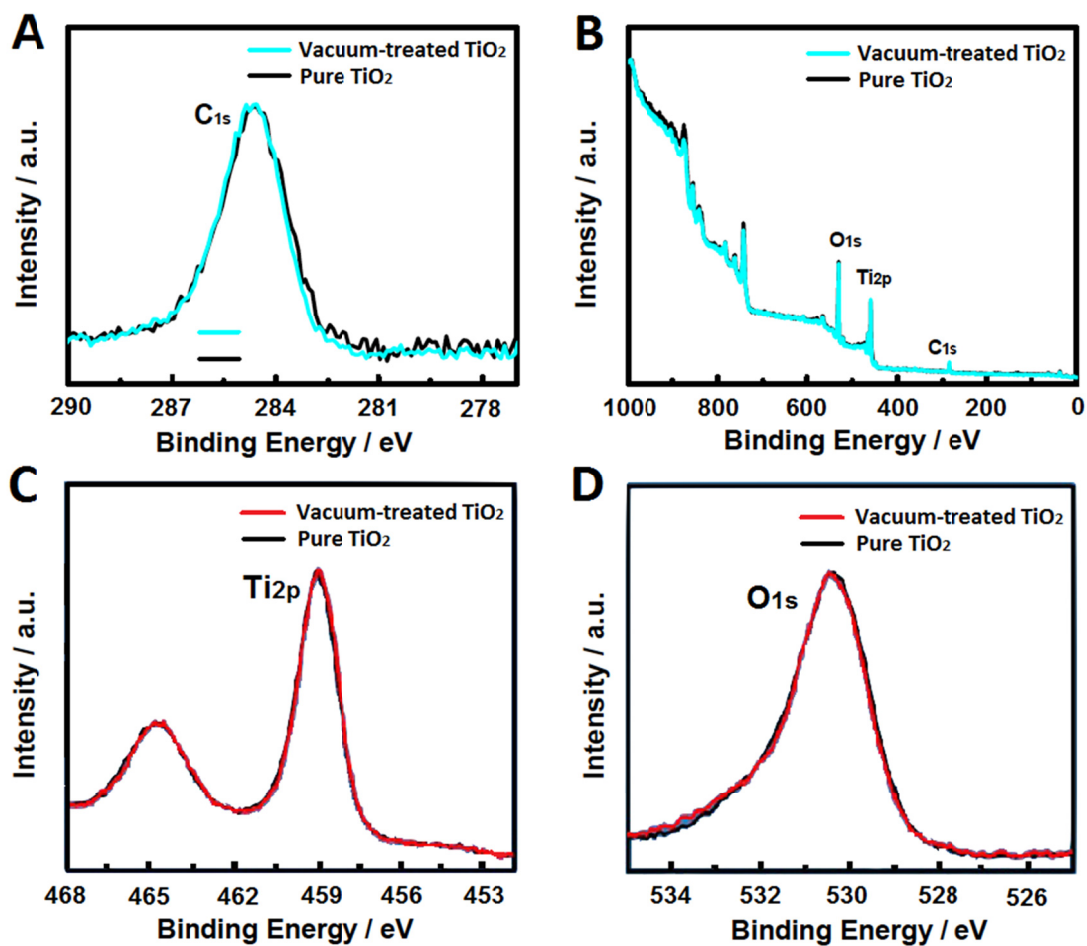


Figure 4.6. (A) XPS survey and (B) C *1s* (C) O *1s* (D) Ti *2p* of the pure TiO₂ nanocrystals and the vacuum-treated TiO₂ nanocrystals.

4.4 Results and Discussions of Cycling Performances

4.4.1 Discharge Capacity

The variations of discharge capacity versus cycle number for the first 500 cycles of the pure TiO₂ nanocrystals and the vacuum-treated TiO₂ nanocrystals are shown in Figure 4.7 (A). The first cycle was conducted at C/25 rate, and the second cycle was conducted at C/5 rate, and the remaining cycles were conducted at 1C rate. The initial discharge capacity of the vacuum-treated TiO₂ nanocrystals was 270 mAh/g at C/25 rate, 13.9% higher than the pure TiO₂ nanocrystals (237 mAh/g). For the second cycle, the discharge capacity of the vacuum-treated TiO₂ nanocrystals was 206 mAh/g at C/5 rate, 27.2% higher than that of the pure TiO₂ nanocrystals (162 mAh/g). For the third cycle, the discharge capacity of the vacuum-treated TiO₂ nanocrystals was 173 mAh/g at 1C rate, 25.4% higher than that of the pure TiO₂ nanocrystals (138 mAh/g). By the end of 500 cycles, the discharge capacity of the vacuum-treated TiO₂ nanocrystals was 131 mAh/g at 1C rate, 40.9% higher than that of the pure TiO₂ nanocrystals (93 mAh/g). Interestingly, the vacuum-treated TiO₂ nanocrystals experienced a fluctuation during 200-300 cycles while the pure TiO₂ nanocrystals underwent a fluctuation in the first 10 cycles (Figure 4.7 (B)).

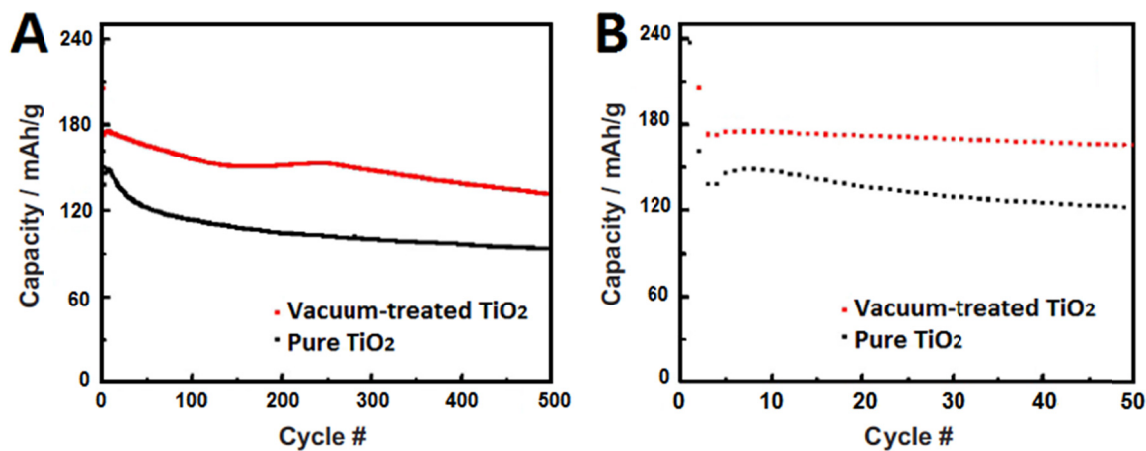


Figure 4.7. Variation of discharge capacity versus cycle number for (A) the first 500 cycles and (B) the first 50 cycles of the pure TiO₂ nanocrystals and the vacuum-treated TiO₂ nanocrystals.

4.4.2 Coulombic Efficiency

The variations of Coulombic efficiency along with the charge/discharge versus cycle number for the first 500 cycles of the pure TiO₂ nanocrystals and the vacuum-treated TiO₂ nanocrystals are shown in Figure 4.8 (A) and Figure 4.8 (B), respectively. Both samples had a steady efficiency after around 50 cycles. A closer look at the first 20 cycles of both the pure TiO₂ nanocrystals and the vacuum-treated TiO₂ nanocrystals showed that there was a fluctuation difference between the two samples in the first 20 cycles (Figure 4.8 (C) and Figure 4.8 (D)). As discussed before, the pure TiO₂ nanocrystals went through a large fluctuation in the first 4 cycles, and then followed by a slight decrease in the next 16 cycles (Figure 4.8 (C)). However, the vacuum-treated TiO₂ nanocrystals only experienced a small fluctuation and followed by a steady maximum efficiency in the next 16 cycles. The smaller fluctuation could be attributed to a better structural

accommodation of lithium-ions during the charge/discharge processes. By the end of 500 cycles, the Coulombic efficiency of the pure TiO₂ nanocrystals was around 99.6%, while the value of the vacuum-treated TiO₂ nanocrystals was around 99.9%. The vacuum-treated TiO₂ nanocrystals had better Coulombic efficiency than the pure TiO₂ nanocrystals. Similarly, it could be attributed to the special structure in the surface layer of the vacuum-treated TiO₂ nanocrystals.

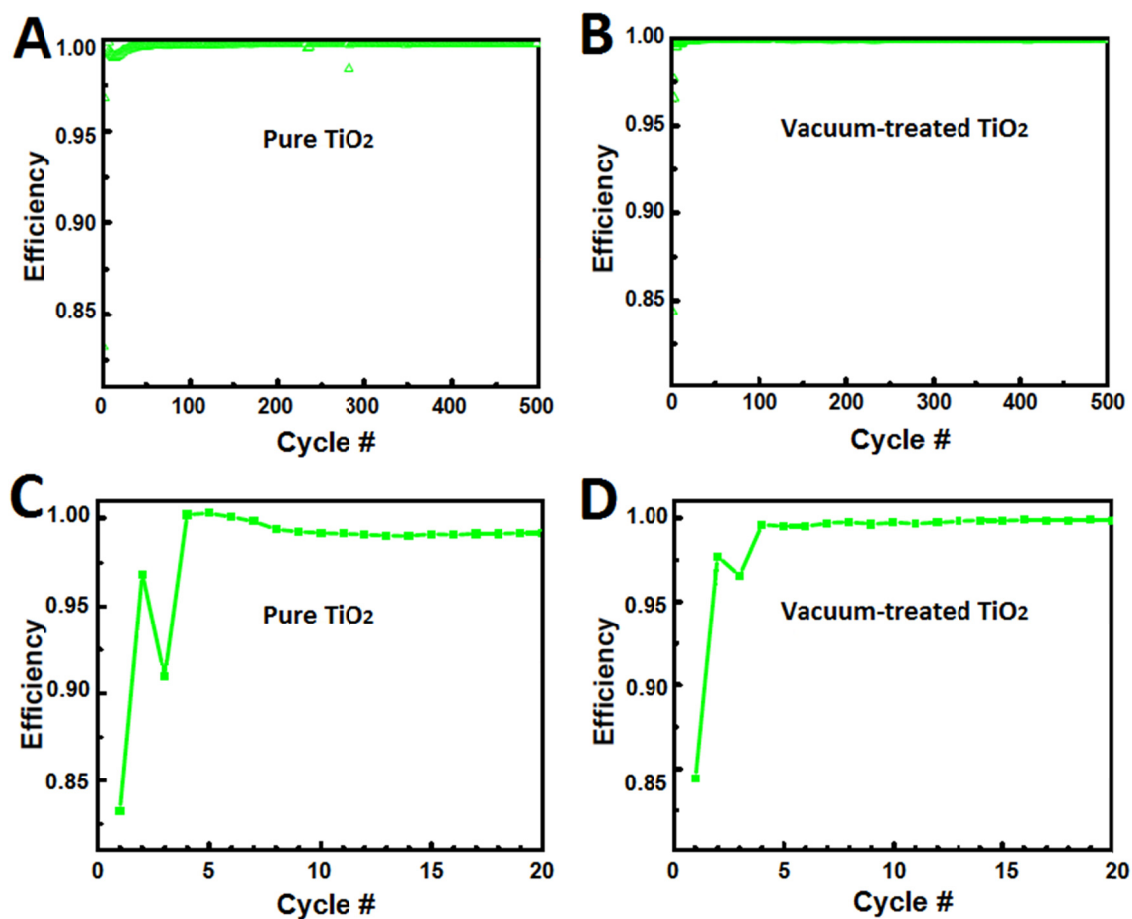


Figure 4.8. Variation of Coulombic efficiency along with the charge/discharge versus cycle number of the pure TiO₂ nanocrystals (A: the first 500 cycles, C: the first 20 cycles) and the vacuum-treated TiO₂ nanocrystals (B: the first 500 cycles, D: the first 20 cycles).

4.4.3 Rate Performance

The rate performances of the pure TiO₂ nanocrystals and the vacuum-treated TiO₂ nanocrystals are shown in Figure 4.9 and Table 4.1. For the first 18 cycles of the rate performance test, the charge and discharge rates were changed simultaneously, and for the following cycles only the charge rates were changed while the discharge rate was kept at 1C. As expected, for both samples, the discharge capacity decreased as the charge rate increased, and the vacuum-treated TiO₂ nanocrystals had better performance at high rates than the pure TiO₂ nanocrystals. For example, for the first 18 cycles, the capacity of the vacuum-treated TiO₂ nanocrystals was 75 mAh/g at 20C rate and 33 mAh/g at 50C rate, 114.3% and 371.4% higher than that of the pure TiO₂ nanocrystals (35 mAh/g at 20C rate, 7 mAh/g at 50C rate), respectively. To reach a capacity of 150 mAh/g, the pure TiO₂ nanocrystals will take around 1 hour (1C rate) to charge, while for the vacuum-treated TiO₂ nanocrystals, it will only take less than 30 minutes (> 2C rate). For the next 18 cycles, when the discharge rate was kept at 1C rate and the charge capacity changed, the discharge capacity of both samples increased compared to the case where both the charge/discharge rates were the same. The vacuum-treated TiO₂ nanocrystals had much higher discharge capacity than the pure TiO₂ nanocrystals, especially for the high rates. For example, the capacity of the pure TiO₂ nanocrystals was 83 mAh/g at 20C rate and 35 mAh/g at 50C rate, while for the vacuum-treated TiO₂ nanocrystals, the value was 159 mAh/g at 2C rate and 120 mAh/g at 50C rate. The increase was 91.6% and 242.9%, respectively. Obviously, the vacuum-treated TiO₂ nanocrystals had a higher rate performance than the pure TiO₂ nanocrystals, which could be possibly caused by the

lower lithium-ion transport resistance during the charge/discharge processes, and the larger capacity was resulted from the larger charge diffusion depth within the TiO_2 nanocrystals under the same testing conditions. It was in agreement with previous findings.¹⁸⁸

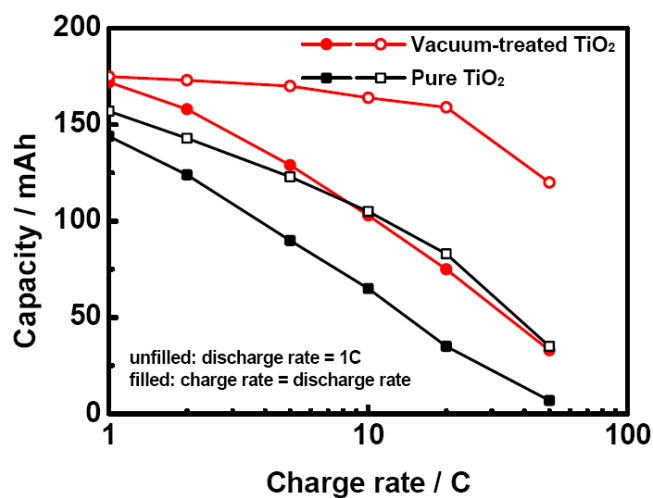


Figure 4.9. Comparison of the discharge capacities of the pure TiO_2 nanocrystals and the vacuum-treated TiO_2 nanocrystals at various charge rates.

Table 4.1. Rate performance of the pure TiO₂ nanocrystals and the vacuum-treated TiO₂ nanocrystals at various charge rates.

		Sample	1C	2C	5C	10C	20C	50C
Discharge capacity/ mAh/g	1-18 cycles	Pure ^a	144	124	90	65	35	7
	(Symmetric ^b)	Vac ^c	172	158	129	103	75	33
	19-36 cycles	Pure ^a	157	143	123	105	83	35
	(Asymmetric ^d)	Vac ^c	175	173	170	164	159	120

^aPure means the pure TiO₂ nanocrystals.

^bSymmetric means charge rate equals discharge rate.

^cVac means the vacuum-treated TiO₂ nanocrystals.

^dAsymmetric means discharge rate equals 1C.

4.4.4 Analysis of Galvanostatic Charge/Discharge Profiles

The galvanostatic charge/discharge profiles for the first cycle at C/25 rate, 35th cycle at 1 C rate, and 100th cycle at 1C rate for the electrode made of the pure TiO₂ nanocrystals and the vacuum-treated TiO₂ nanocrystals are shown in Figure 4.10 (A) and Figure 4.10 (B), respectively. Besides the larger charge/discharge capacity, the vacuum-treated TiO₂ nanocrystals had larger charge/discharge plateaus and smaller potential differences between the charge and discharge cycle than the pure TiO₂ nanocrystals in these cycles. The average potential difference between the charge and discharge cycle of the vacuum-treated TiO₂ nanocrystals was about 0.11 V, 42.1% smaller than that of the pure TiO₂ nanocrystals (0.19 V). Same analysis as the hydrogenated TiO₂ nanocrystals, the smaller potential differences indicated the decreased charge transfer resistance. It might have been caused by the weaker chemical bonding between the transferred charge and the host matrix in the vacuum-treated TiO₂ nanocrystals. Thus, lithium-ions

transported more easily in the amorphous layer than in the crystalline core. The larger charge/discharge plateaus suggested the bulk intercalation ability increased, which might have been caused by a larger charge transfer depth. The special outer layer introduced by the vacuum treatment might have facilitated the charge transfer in the nanocrystals.

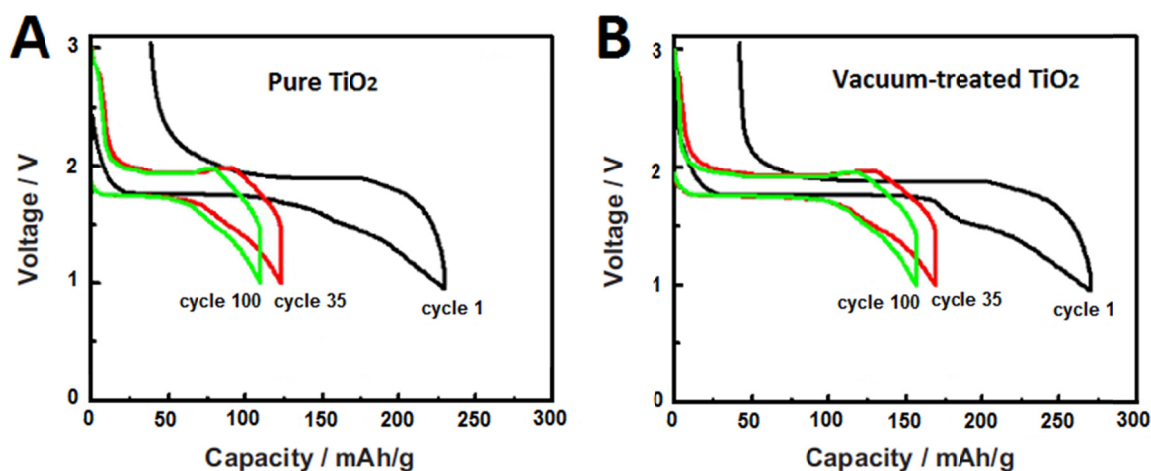


Figure 4.10. Galvanostatic charge/discharge profiles for the first cycle at C/25 rate, 35th cycle at 1 C rate, and 100th cycle at 1C rate for the electrode made of (A) the pure TiO₂ nanocrystals and (B) the vacuum-treated TiO₂ nanocrystals.

Figure 4.11 (A) and Figure 4.11 (B) showed the galvanostatic charge/discharge profiles at various charge rates for the electrode made of the pure TiO₂ nanocrystals and the vacuum-treated TiO₂ nanocrystals, respectively. Apparently, at various rates, the vacuum-treated TiO₂ nanocrystals showed higher discharge capacity and larger charge/discharge plateaus between the charge/discharge cycles at each charge rate than the pure TiO₂ nanocrystals at the same rate. Again, it indicated that charge transfer was smoother in the vacuum-treated TiO₂ nanocrystals than in the pure TiO₂ nanocrystals. It

was also caused by the special amorphous surface structure of the vacuum-treated TiO₂ nanocrystals.

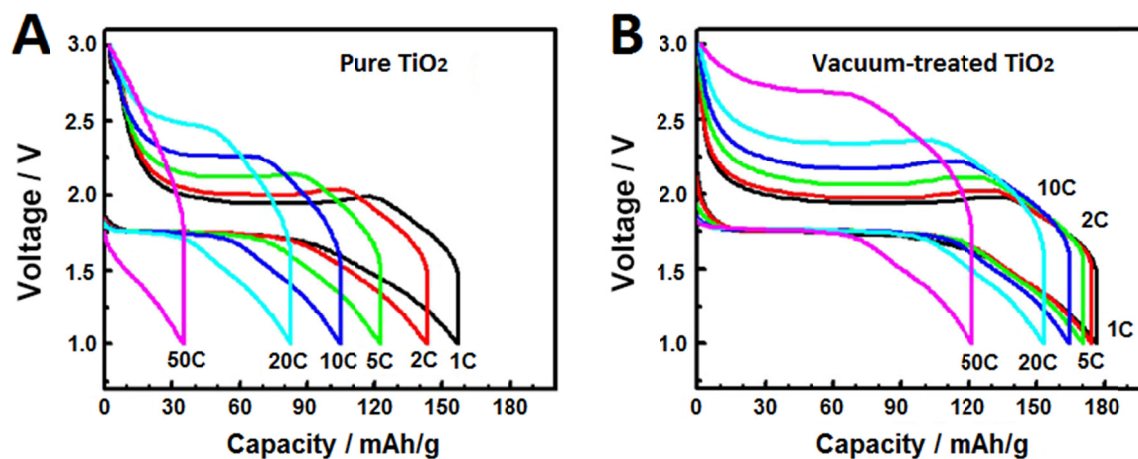


Figure 4.11. Galvanostatic charge/discharge profiles at various charge rates (discharge rate = 1C) for the electrode made of (A) the pure TiO₂ nanocrystals and (B) the vacuum-treated TiO₂ nanocrystals.

In order to further understand why the vacuum-treated TiO₂ nanocrystals performed better than the pure TiO₂ nanocrystals in these cycling tests, the comparison of the galvanostatic charge/discharge profiles for the pure TiO₂ nanocrystals and the vacuum-treated TiO₂ nanocrystals at charge rate of 20C is shown in Figure 4.12. The discharge curve for the nanoporous anatase electrode could be divided into three voltage regions: region A (> 1.75 V), region B (\approx 1.75 V), and region C (< 1.75 V).^{91,121} In region A, the voltage went through a monotonic drop to around 1.75 V. It was attributed to the homogeneous insertion of lithium-ions into the bulk, up to a solid-solution limit of lithium-ions in TiO₂.⁹¹ When the voltage dropped to around 1.75 V, it went into region B.

In this region, there was a bi-phase plateau with the lithium-rich phases ($\text{Li}_{0.2}\text{TiO}_2$ / $\text{Li}_{0.4}\text{TiO}_2$) coexisting with the lithium-poor phase (anatase TiO_2).⁹¹ Then the voltage fell below 1.75 V to reach region C, which was caused by the reversible storage of lithium-ions at the particle interface.⁹¹ As the voltage was higher than 1.75 V, although the two phases could accommodate more lithium-ions ($x > 0.5$), the phases no longer dissolved lithium-ions reversibly.⁹¹ In Figure 4.12, the vacuum-treated TiO_2 nanocrystals had a larger region B (voltage plateau) and region C than the pure TiO_2 nanocrystals. Shin et al.⁹¹ reported that reducing the particle size could increase the bulk intercalation and the interfacial storage capacities, resulting in increase of region B (due to the shorter diffusion length) and region C (due to the larger interfacial area). According to the TEM (Figure 4.1) and XRD results, both samples had a similar particle size. Thus, the increase of region B and region C was not mainly caused by the particle size. The newly introduced vacuum-treated layer of the vacuum-treated TiO_2 nanocrystals might have played a key role in the improvement. That meant the outer layer containing the oxygen vacancies of the vacuum-treated TiO_2 nanocrystals enhanced bulk intercalation by increasing the diffusion coefficient of lithium-ions. This outer layer also helped the interfacial storage capacities by increasing the surface area.

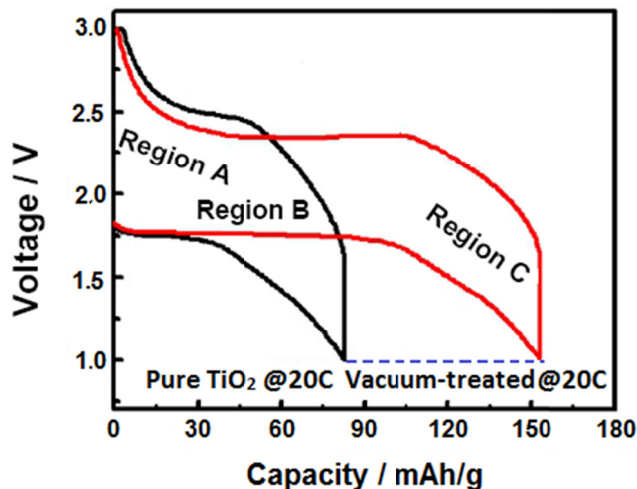


Figure 4.12. Comparison of the galvanostatic charge/discharge profiles for the pure TiO₂ nanocrystals and the vacuum-treated TiO₂ nanocrystals at charge rate of 20C.

4.5 EIS Analysis

In order to understand the charge transfer process across the cell, an electrochemical impedance study was performed on both samples at the same condition (Figure 4.13). All cells were cycled for two cycles and fully discharged to 1 V before EIS measurements. The equivalent circuit modeling used to fit the EIS is shown in Scheme 4.1, and the corresponding components in the circuit and the battery are shown in Figure 4.14. The fitting results are listed in Table 4.2. R_S represents the ohmic resistance, including the bulk resistance of the electrolyte, the separator, and the electrode. R_1 represents the charge transfer resistance at the carbon/TiO₂ electrode interface. R_2 represents the lithium-ion transport resistance at the carbon/TiO₂ electrode interface. R_{cd} represents the interfacial charge transfer resistance of the interface between the surface layers and the bulk for the pure TiO₂ nanocrystals, or the interface between the amorphous surface

layers and the bulk for the vacuum-treated TiO₂ nanocrystals. W_oR is the Warburg charge diffusion resistance in the TiO₂ electrode. W_oT is Warburg diffusion time, which equals L^2/D in the electrode, where L is the length of the diffusion layer in the electrode and D is the diffusion coefficient in the electrode. W_oP is the Warburg exponent. C_1 represents the space charge capacitance the carbon/TiO₂ electrode interface. C_2 is the double layer charge capacitance at the carbon/TiO₂ electrode interface. C_d represents the space charge capacitance at the interface between the surface layer (< 0.5 nm) and the bulk for the pure TiO₂ nanocrystals, or the interface between the amorphous surface layer (< 1-2 nm) and the bulk for the vacuum-treated TiO₂ nanocrystals.

The fitting results showed that the ohmic resistance of the vacuum-treated TiO₂ nanocrystals was a little higher (4.4 Ω) than that of the pure TiO₂ nanocrystals (3.1 Ω). The resistances of charge transfer and lithium-ion transport were largely reduced for the vacuum-treated TiO₂ nanocrystals compared to the pure TiO₂ nanocrystals. The decrease/increase of charge transfer resistance at the interface for each component was accompanied by the decrease/increase of capacitance for that component (i.e., $R_1 \sim C_1$, $R_2 \sim C_2$, and $R_{cd} \sim C_d$). The charge transfer resistance (R_1) at the carbon/TiO₂ electrode interface was reduced by the amorphous surface layer from 28.9 Ω to 6.9 Ω, accompanied by the space charge capacitance (C_1) decreased from 4.2E-5 F to 9.5E-7 F. The lithium-ion transport resistance (R_2) was reduced by the amorphous surface layer from 34.9 Ω to 12.7 Ω, accompanied by the double layer charge capacitance (C_2) decreased from 0.02 F to 4.4E-5 F. The interfacial charge transfer resistance of the interface between the surface layers and the bulk for the pure TiO₂ nanocrystals (R_{cd}) was

lower (2.2Ω) than that of the interface between the amorphous surface layers and the bulk for the vacuum-treated TiO_2 nanocrystals (8.0Ω), accompanied by the increase of charge capacitance (C_d) from $1.1\text{E-}6 \text{ F}$ to $5.4\text{E-}6 \text{ F}$. These results indicated that the lower charge capacitance or accumulation (C_1 and C_2) at the interface led to a lower charge transfer resistance (R_1 and R_2) or a breakdown of the formation of charge accumulation at these interfaces could reduce charge transfer resistance. It was possibly caused by the better adsorption and penetration into the amorphous surface layer. The higher space charge capacitance (C_d) at the interface between the amorphous surface layer and the bulk for the vacuum-treated TiO_2 nanocrystals than that of the pure TiO_2 nanocrystals suggested the charge accumulated between these layers. As for the Warburg charge diffusion resistance (W_o-R), the vacuum-treated TiO_2 nanocrystals had a much smaller value (82.6Ω) than the pure TiO_2 nanocrystals (1287Ω), which indicated that the charge transfer was much easier for the vacuum-treated TiO_2 nanocrystals. As the charge transfer process was mainly limited by the most reluctant bulk diffusion in the electrode, the much smaller resistance (W_o-R) in the vacuum-treated TiO_2 nanocrystals electrode was supposed to have a much better rate performance. Overall, the charge accumulation layer at the interfaces was broken down for charge transfer due to the breakdown of charge accumulation, and the charge transfer resistance in the bulk was largely reduced, so the performances of the lithium-ion battery was expected to be largely improved for the vacuum-treated TiO_2 nanocrystals. This speculation was consistent with the results of the cycling performance tests.

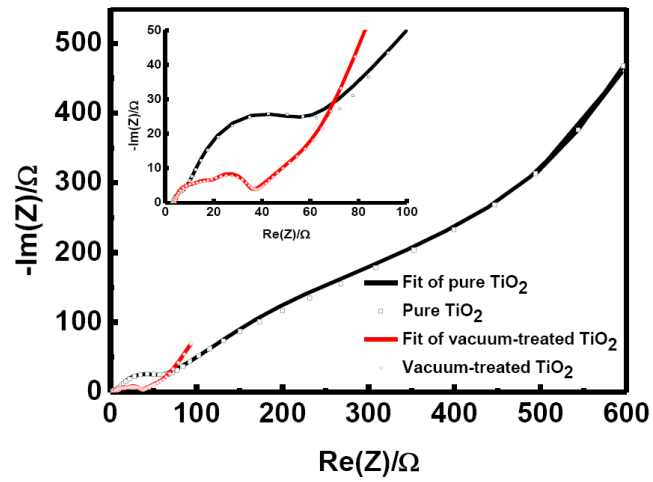
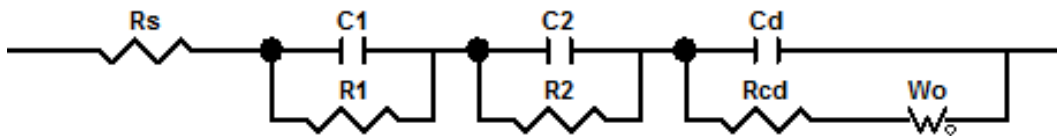


Figure 4.13. EIS of the pure TiO_2 nanocrystals and the vacuum-treated TiO_2 nanocrystals.



Scheme 4.1. The equivalent circuit modeling used to fit the EIS.

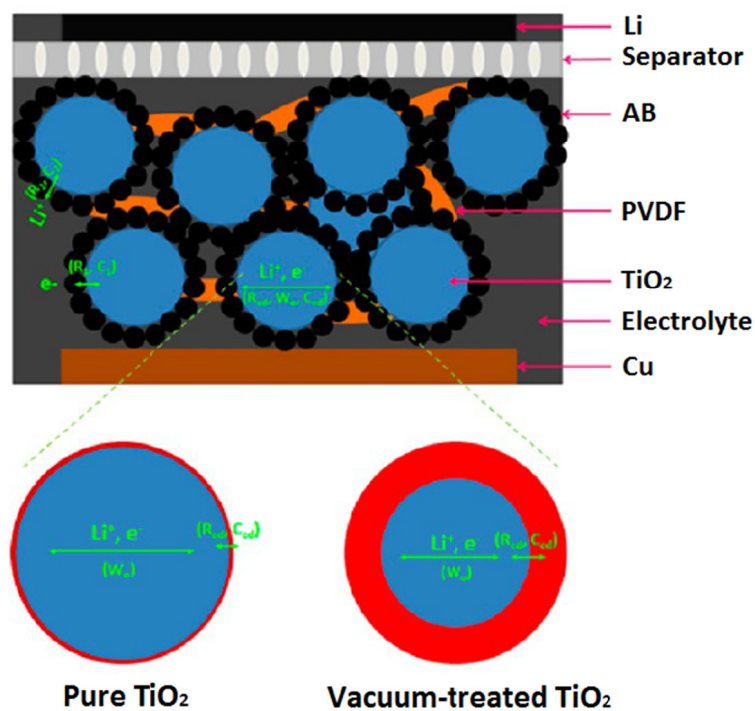


Figure 4.14. The corresponding components in the circuit and the battery.

Table 4.2. The fitted EIS results from the equivalent circuits.

	R_S/Ω	R_1/Ω	R_2/Ω	R_{Cd}/Ω	W_o-R	W_o-T	W_o-P	C_1/F	C_2/F	C_d/F
Pure ^a	3.1	28.9	34.9	2.2	1287	67.3	0.39	4.2E-5	0.02	1.1E-6
Vac ^b	4.3	6.9	12.7	8.0	82.6	17.8	0.35	9.5E-7	4.4E-5	5.4E-6

^aPure means the pure TiO₂ nanocrystals.

^bVac means the vacuum-treated TiO₂ nanocrystals.

4.6 Relationships between Structure and Battery Performances

As shown in Figure 4.15, the vacuum-treated TiO₂ nanocrystals containing an amorphous outer layer outside the crystalline core was obtained by the vacuum treatment of the pure TiO₂ nanocrystals. According to the TEM (Figure 4.1) and XRD results, both samples had a similar particle size around 10 nm. Different from the pure TiO₂ nanocrystals, the vacuum-treated TiO₂ nanocrystals were reconstructed with an amorphous outer layer with a thickness around 1-2 nm. The Raman spectra (Figure 4.3) further proved this conclusion. The ESR measurement checked the creation of the oxygen vacancies on the surface of the vacuum-treated TiO₂ nanocrystals. The XPS (Figure 4.6) provided the information that both samples had similar Ti 2*p* and O 1*s* spectra. It indicated that the differences between the two samples existed in the outer of the vacuum-treated TiO₂ nanocrystals, while the main structures were almost identical. Both samples were used as an electrode material in half-cells and their cycling performances were tested thereafter. The vacuum-treated TiO₂ nanocrystals had better battery performances than the pure TiO₂ nanocrystals in terms of discharge capacity, Coulombic efficiency, and rate performance. It meant that the amorphous outer layer introduced by the vacuum treatment could have facilitated the charge transfer and the capacity retention of the electrodes.

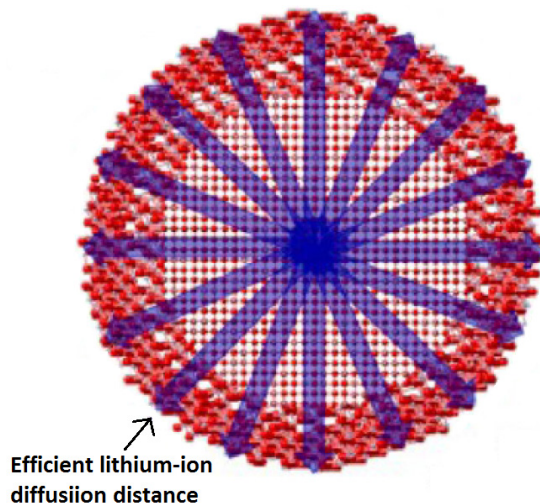


Figure 4.15. Illustration of the vacuum-treated TiO_2 containing the amorphous layer to facilitate charge transfer and the capacity retention.

4.6.1 Structural Tolerance

As can be seen in the high-resolution TEM (Figure 4.1 (E)), the vacuum-treated TiO_2 nanocrystals had a large rough surface. Similar to the hydrogenated TiO_2 nanocrystals, there might have edges and corners on the atomic level that were more favorable for ion adsorption due to the possible surface dangling bonding available. Furthermore, as the surface of the vacuum-treated TiO_2 nanocrystals was disordered, the lattice might have less thermodynamically metastable energetic states than the pure TiO_2 nanocrystals. Thus, the penetration of lithium-ions into the lattice of the host matrix might have been enhanced, and further resulted in lower lithium-ion transport resistance. This inference was consistent with the cycling performance tests. As for the pure TiO_2 nanocrystals, they had an ordered rigid surface that might not have provided a good interface to accommodate lithium-ions, causing low a discharge capacity (Figure 4.7 and

Figure 4.10 (A)), a variable Coulombic efficiency (Figure 4.8 (C)), and a poor rate performance (Figure 4.9 and Figure 4.11 (A)). Due to the large structural distortion tolerance, the vacuum-treated TiO₂ nanocrystals might have accommodated lithium-ions much more easily, providing a high discharge capacity (Figure 4.7 and Figure 4.10 (A)), a stable Coulombic efficiency (Figure 4.8 (D)), and a good rate performance (Figure 4.9 and Figure 4.11 (B)).

4.6.2 Built-in Electric Field (BIEF)

As indicated by the ESR results (Figure 4.5), the oxygen vacancies were successfully created during the vacuum treatment, resulting in an oxygen-vacancy adequate amorphous layer TiO_{2-x} shell and a crystalline stoichiometric TiO₂ core. The nonstoichiometric TiO_{2-x} is a well-known *n*-type semiconductor,^{201,206-208} while the stoichiometric TiO₂ is a typical *i*-type semiconductor.^{201,208} Then, the TiO_{2-x}/TiO₂ shell/core will form an *n-i* heterojunction in the disordered/crystalline interface.²⁰⁸ A BIEF will be introduced across the interface. The direction of the BIEF will point to the core from the outer layer. Thus, under this field, the intercalation process of lithium-ions into TiO₂ nanocrystals will become much easier (Figure 4.16 (A)). When lithium-ions have been fully intercalated into the TiO₂ nanocrystals, the core will become Li_yTiO₂, a presumably intrinsic semiconductor. However, the disordered outer layer can hold much less lithium-ions than the crystalline core due to the existence of the oxygen vacancies. It will become Li_{y-2x-δ}TiO_{2-x}, a relative *p*-type semiconductor to Li_yTiO₂. Again, a new BIEF will be formed in the core/shell interface. The direction of the BIEF will point out

to the disordered layer from the crystalline core. It will facilitate the transport of lithium-ions from the core to the shell, helping the extraction of lithium-ions (Figure 4.16 (B)). At the same time, the movement of electrons is less favored under the BIEF. As electron diffusion coefficients are a few magnitudes higher than that of lithium-ions, it would only induce a smaller increase of electron resistance and gain a large reduction in the lithium-ion diffusion resistance. Overall, the charge transfer resistance will be largely lowered because of the BIEF. As discussed before in the EIS analysis, the Warburg charge diffusion resistance (W_oR) of the vacuum-treated TiO₂ nanocrystals was much smaller (82.6 Ω) than the pure TiO₂ nanocrystals (1287 Ω). That meant the BIEF did help to reduce the charge transfer resistance in the equivalent circuit modeling. As the charge transfer resistance process was mainly limited by the most reluctant bulk diffusion in the electrode, the much smaller resistance (W_oR) in the vacuum-treated TiO₂ nanocrystals electrode induced much battery rate performance. This result was further proved by the results of the actual tests. In summary, the enhancement mechanism of the diffusion of lithium-ions in the TiO₂ nanocrystals under the help of the BIEF makes sense. Moreover, this mechanism opens a new concept for lithium-ion rechargeable battery research toward high power application. Additionally, this BIEF mechanism can also successfully explain the large enhancement of the battery performances of the previously reported crystalline/amorphous, core/shell, high capacity and high current silicon nanowire battery electrodes,²⁰⁹ and the recent high-rate, oxygen deficient TiO_{2-δ} nanoparticles¹¹² as well.

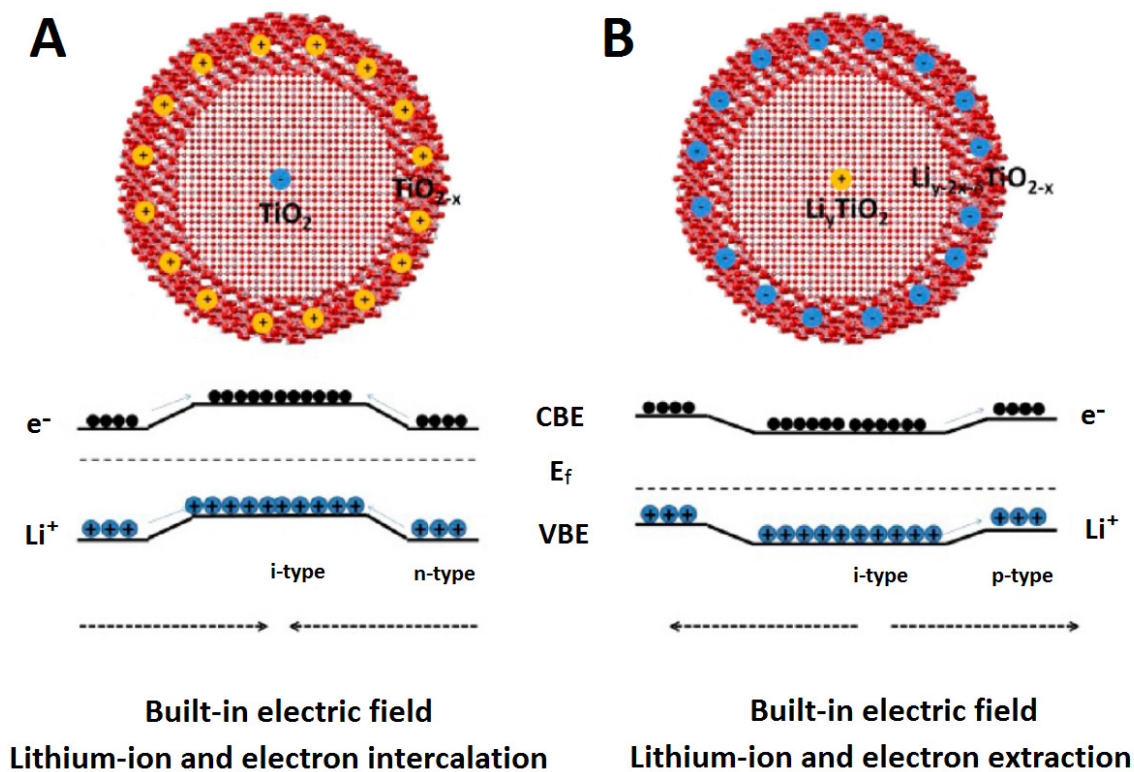


Figure 4.16. The illustration of the facilitation of charge transfer under the BIEF during (A) intercalation and (B) extraction processes.

4.7 Summary

In summary, through the vacuum treatment, the pure TiO_2 nanocrystals were converted to the vacuum-treated TiO_2 nanocrystals with a disordered amorphous outer layer containing oxygen vacancies covered on the crystalline core. The vacuum treatment was used as another modification method to improve the battery performances of TiO_2 nanocrystals. Compared with the pure TiO_2 nanocrystals, the vacuum-treated TiO_2 nanocrystals displayed a better discharge capacity (131 mAh/g after 500 cycles), a near

100% Coulombic efficiency without noticeable degradation, and an improved high-rate performance.

From the analysis of the galvanostatic charge/discharge profiles, it indicated that the disordered amorphous layer of the vacuum-treated TiO₂ nanocrystals possessed a weaker chemical bonding between the transferred charge and host matrix. Besides, it provided a larger charge transfer depth. EIS was used to study the charge transfer process inside the cell. It was concluded that the charge accumulation layer at the interfaces was broken down for charge transfer due to breakdown of charge accumulation, and the charge transfer resistance in the bulk was largely reduced. Same as the hydrogenated TiO₂ nanocrystals, the large structural tolerance of the vacuum-treated TiO₂ nanocrystals could be one possible reason to explain the improvement. In addition, the oxygen vacancies created by the vacuum treatment helped form a BIEF that facilitated the transport of lithium-ions during the charge/discharge processes. The concept of creating BIEF within the nanocrystal electrode materials via reconstructing the surface of crystalline electrode materials into amorphous structures at the nanometer scale could be a new approach for improving the battery performances. Although the actual value of the BIEF with the nanocrystals was not measured, from classical semiconductor theories, the BIEF did exist between the stoichiometric crystalline core and the amorphous nonstoichiometric shell with oxygen vacancies. The magnitude of the BIEF is expected to depend on the oxygen vacancy content in the amorphous layer. The transport of lithium-ions is expected to depend on the thickness of the amorphous layer and the crystalline core. Thus, the optimization of these parameters would probably further improve the performances of the

electrode materials. The amorphous layer coupled with the oxygen vacancy is necessary to make the BIEF with the crystalline core of stoichiometric composition. Meanwhile, this concept could be also applied to other battery material system to help make high energy, high power batteries.

CHAPTER 5

DESIGN, PREPARATION AND PROPERTIES OF THE CARBON-COATED TITANIUM DIOXIDE NANOCRYSTALS

(The main content of this chapter was published in Nano Energy, 2014, 6, 109-118 entitled “Amorphous carbon-coated TiO₂ nanocrystals for improved lithium-ion battery and photocatalytic performance” as research article.)

5.1 Introduction

As discussed before, the low electronic conductivity (10^{-4} S/cm)²¹ in the solid phase and the low diffusion coefficient of lithium-ions (10^{-11} to 10^{-13} cm²/s)¹¹² are the two major difficulties that hinder the application of TiO₂. One method to improve the electronic conductivity is to add a conductive phase. Among them, the carbon coating is a widely used method.¹⁴¹

In this chapter, a thin layer of carbon coating was obtained by a vacuum decomposition-deposition process of the pure TiO₂ nanocrystals. This carbon layer was supposed to increase the conductivity of the TiO₂ nanocrystals, thereby the carbon-coated TiO₂ nanocrystals were supposed to have better battery performances. Low-resolution TEM and high-resolution TEM, XRD, Raman, FTIR, and TGA were used to characterize the structure of the pure TiO₂ nanocrystals and the carbon-coated TiO₂ nanocrystals. Electrodes were made by both samples to compare their discharge capacity, Coulombic

efficiency, and rate performance. The carbon-coated TiO₂ nanocrystals showed better battery performances than the pure TiO₂ nanocrystals. EIS was used to analyze the electrochemical processes inside the cell. The relationships between the structure and the battery performances were also studied.

5.2 Preparation

The carbon-coated TiO₂ nanocrystals were synthesized through a vacuum decomposition-deposition treatment process. The calcinated samples (the pure TiO₂ nanocrystals) and the uncalcinated samples were put separately into two beakers in the same vacuum chamber at 600 °C for 4 hours. The decomposition of the uncalcinated TiO₂ precursor deposited a thin-layer of amorphous carbon on the surface of the pure TiO₂ nanocrystals to obtain the carbon-coated TiO₂ nanocrystals. The experiment methods were described in Chapter 2 in detail.

5.3 Results and Discussions of Characterization

5.3.1 Low-Resolution TEM and High-Resolution TEM

The low-resolution, high-resolution TEM, and SAED patterns of the pure TiO₂ nanocrystals and the carbon-coated TiO₂ nanocrystals are shown in Figure 5.1. Low-resolution TEM images showed that both samples had a similar size around 10 nm (Figure 5.1 (A) and Figure 5.1 (C)). Also, the aggregations and overlaps could be observed. The SAED pattern of the pure TiO₂ nanocrystals indicated the samples were

highly crystallized. As for the carbon-coated TiO₂ nanocrystals, the thick and milky diffraction background besides the anatase diffraction rings suggested that the carbon-coated TiO₂ nanocrystals probably contained an amorphous carbon layer.^{196,197} The high-resolution TEM images of the pure TiO₂ nanocrystals (Figure 5.1 (B)) showed the samples were highly crystallized throughout the whole particle. As shown in Figure 5.1 (D), the carbon-coated TiO₂ nanocrystals might have been coated with a layer of carbon or embedded within an amorphous carbon matrix. This indicated that a carbon layer was successfully coated on the pure TiO₂ nanocrystals.

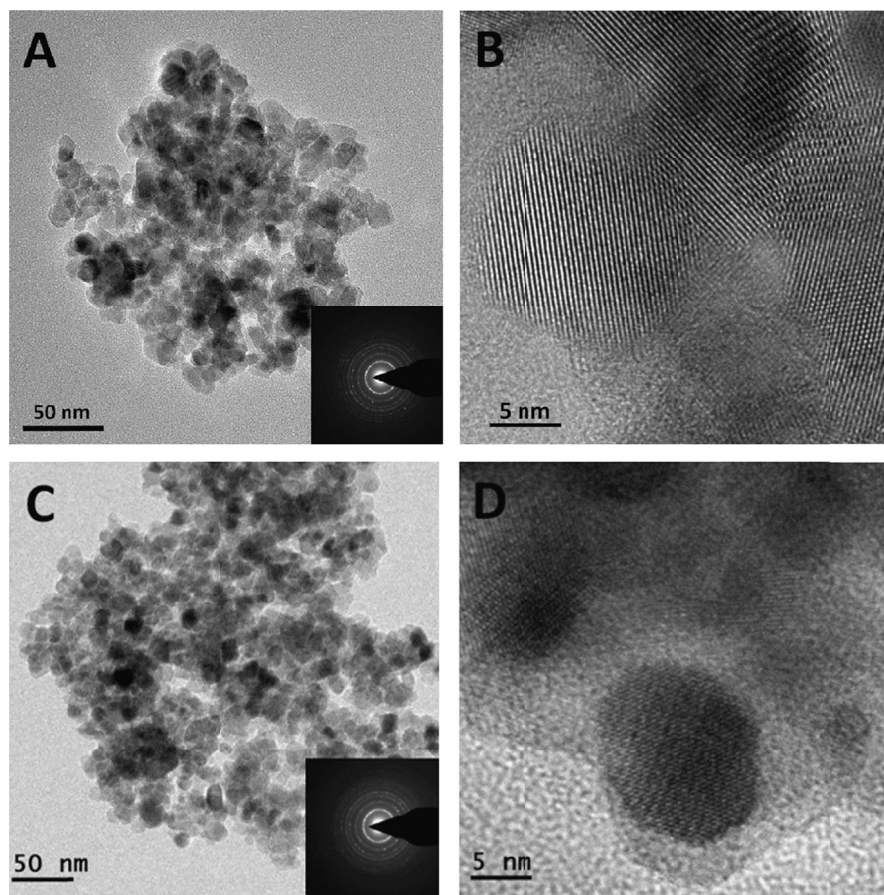


Figure 5.1. Low-resolution and high-resolution TEM images of (A and B) the pure TiO₂ nanocrystals and (C and D) the carbon-coated TiO₂ nanocrystals.

5.3.2 XRD

The XRD patterns of the pure TiO₂ nanocrystals and the carbon-coated TiO₂ nanocrystals are shown in Figure 5.2. The strong typical diffraction peaks of both samples indicated that they were anatase crystals. The directional crystalline grain sizes were calculated by the Scherrer equation. Both samples had a particle size around 10 nm.

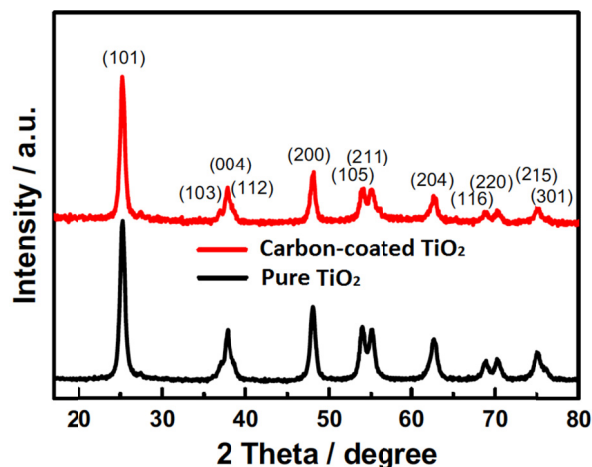


Figure 5.2. XRD patterns of the pure TiO₂ nanocrystals and the carbon-coated TiO₂ nanocrystals.

5.3.3 Raman

Figure 5.3 shows the Raman spectra of the pure TiO₂ nanocrystals and the carbon-coated TiO₂ nanocrystals. As discussed before, the pure TiO₂ nanocrystals showed five Raman active modes in the spectrum. However, for the carbon-coated TiO₂ nanocrystals, there was only a weak peak at around 148.7 cm⁻¹ (E_g) and a large featureless background, which indicated that an amorphous phase might have been generated during the vacuum decomposition-deposition treatment.^{176,198,199} The XRD patterns for the carbon-coated TiO₂ nanocrystals showed that they were crystals. However, the Raman spectra gave the different information. Thus, it was reasonable that the amorphous phase only existed in the outer layer, as the Raman was more sensitive to the surface structure than the XRD.^{176,198,199} It complied with the high-resolution TEM image of the carbon-coated TiO₂ nanocrystals (Figure 4.1 (D)).

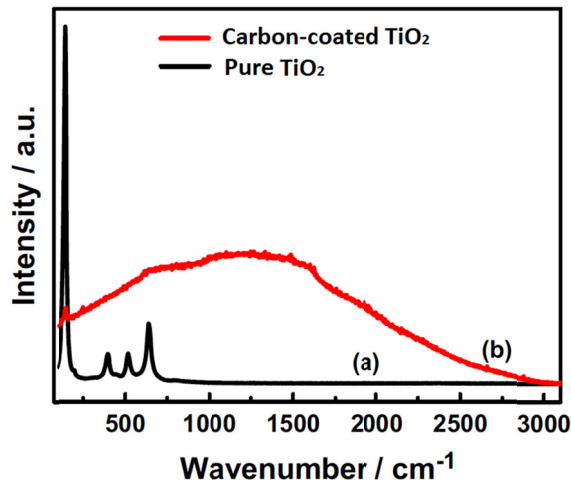


Figure 5.3. Raman spectra of the pure TiO₂ nanocrystals and the carbon-coated TiO₂ nanocrystals.

5.3.4 FTIR

In order to check if there were any organic residues or contaminations left in the amorphous carbon layer formed by decomposing the organic template and the TiO₂ precursor at a high temperature in vacuum, FTIR was measured for the pure TiO₂ nanocrystals and the carbon-coated TiO₂ nanocrystals. Figure 5.4 shows the FTIR reflectance spectra of the two samples. Both samples displayed a similar spectrum. Both of them had a sharp and large peak below 1000 cm⁻¹ due to the O-Ti-O vibrations in the TiO₂ lattice.¹⁷⁸ In addition, they had an absorption band around 1640 cm⁻¹ that could be attributed to the O-H bending of the molecularly physisorbed water from the opening environment, and a broad peak OH absorption from 3000 cm⁻¹ to 3500 cm⁻¹.^{178,184-186} Besides, the FTIR indicated that there were no organic residues left during these treatments for both samples.

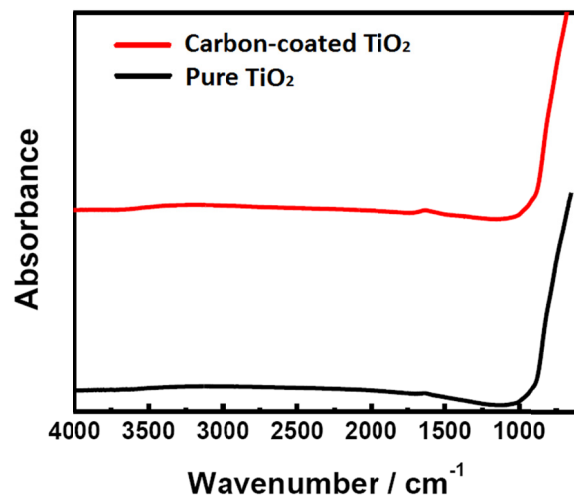


Figure 5.4. FTIR reflectance spectra of the pure TiO₂ nanocrystals and the carbon-coated TiO₂ nanocrystals.

5.3.5 TGA

The TGA spectra of the pure TiO₂ nanocrystals and the carbon-coated TiO₂ nanocrystals are shown in Figure 5.5. It was used to check the amount of carbon coated on the TiO₂ nanocrystals. When the temperature increased to 220 °C, both samples displayed a weight loss of 1.3 wt%, which could be caused by the water physically or chemically adsorbed on the surface or trapped inside the porous amorphous carbon layer. As the samples were heated to 412 °C, another 4.9 wt% weight loss was observed of the carbon-coated TiO₂ nanocrystals, while for the pure TiO₂ nanocrystals, the additional weight loss was 0.3 wt% (caused by loss of OH groups). According to the weight loss difference, the percentage of the amorphous carbon was about 4.6 wt%.

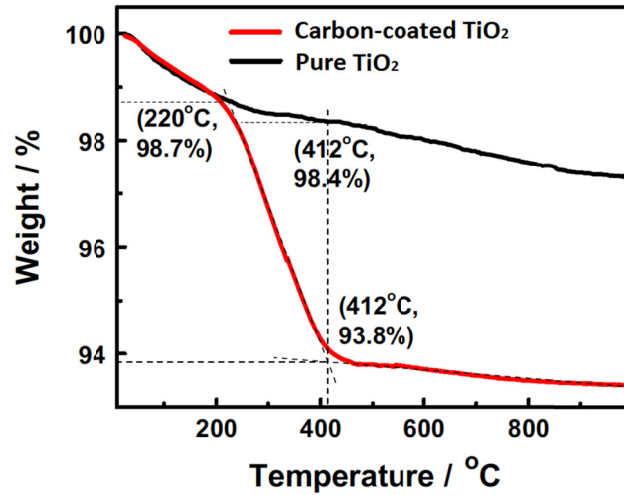


Figure 5.5. TGA spectra of the pure TiO₂ nanocrystals and the carbon-coated TiO₂ nanocrystals.

5.4 Results and Discussions of Cycling Performances

5.4.1 Discharge Capacity

The variations of discharge capacity versus cycle number for the first 100 cycles of the pure TiO₂ nanocrystals and the carbon-coated TiO₂ nanocrystals are shown Figure 5.6 (A). The first cycle was conducted at C/25 rate, and the second cycle was conducted at C/5 rate, and the remaining cycles were conducted at 1C rate. The initial discharge capacity of the carbon-coated TiO₂ nanocrystals was 278 mAh/g at C/25 rate, 17.2% higher than the pure TiO₂ nanocrystals (237 mAh/g). For the second cycle, the discharge capacity of the carbon-coated TiO₂ nanocrystals was 211 mAh/g at C/5 rate, 30.2% higher than that of the pure TiO₂ nanocrystals (162 mAh/g). For the third cycle, the discharge capacity of the carbon-coated TiO₂ nanocrystals was 178 mAh/g at 1C rate,

29.0% higher than that of the pure TiO₂ nanocrystals (138 mAh/g). By the end of 100 cycles, the discharge capacity of the carbon-coated TiO₂ nanocrystals was 166 mAh/g at 1C rate, 46.9% higher than that of the pure TiO₂ nanocrystals (113 mAh/g). The discharge capacity of the carbon-coated TiO₂ nanocrystals after 100 cycles at 1C rate was even higher than that of the initial capacity of the pure TiO₂ nanocrystals at C/5 rate: a 5 times rate performance increase. That meant the vacuum decomposition-deposition process that introduced a thin carbon layer on the crystalline core did largely improve the discharge capacity of the carbon-coated TiO₂ nanocrystals.

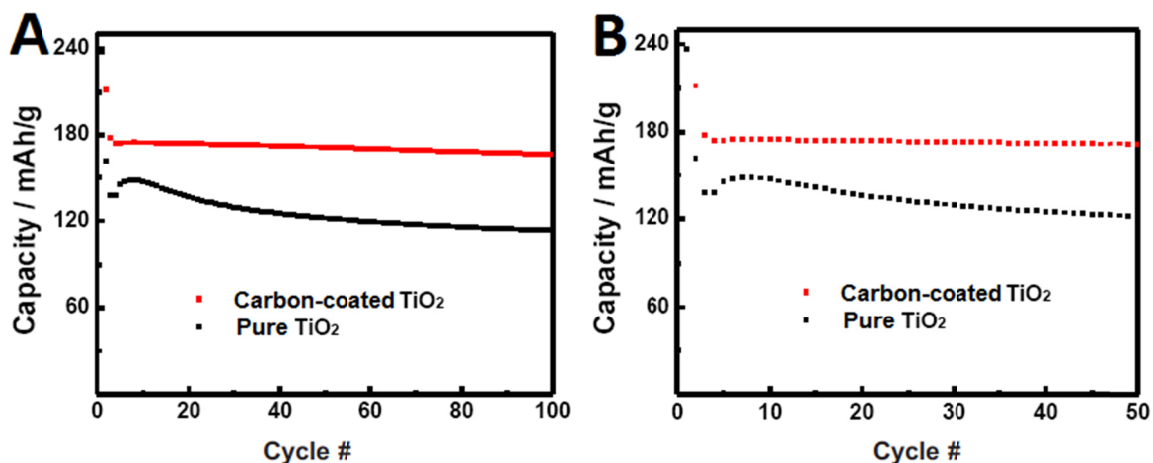


Figure 5.6. Variation of discharge capacity versus cycle number for (A) the first 100 cycles and (B) the first 50 cycles of the pure TiO₂ nanocrystals and the carbon-coated TiO₂ nanocrystals.

5.4.2 Coulombic Efficiency

The variations of Coulombic efficiency along with the charge/discharge versus cycle number for the first 100 cycles of the pure TiO₂ nanocrystals and the carbon-coated TiO₂ nanocrystals are shown in Figure 5.7 (A) and Figure 5.7 (B), respectively. The two samples experienced a steady efficiency after around 50 cycles. For the first 20 cycles of the carbon-coated TiO₂ nanocrystals, the Coulombic efficiency increased in the first 4 cycles and showed a steady trend after that, different from that of the TiO₂ nanocrystals (Figure 5.7 (C) and Figure 5.7 (D)). By the end of 100 cycles, the Coulombic efficiency of the pure TiO₂ nanocrystals was around 99.6%, while the value of the carbon-coated TiO₂ nanocrystals was around 99.7%. The better Coulombic efficiency of the carbon-coated TiO₂ nanocrystals than the pure TiO₂ nanocrystals could be attributed to the special surface structure of the carbon-coated TiO₂ nanocrystals.

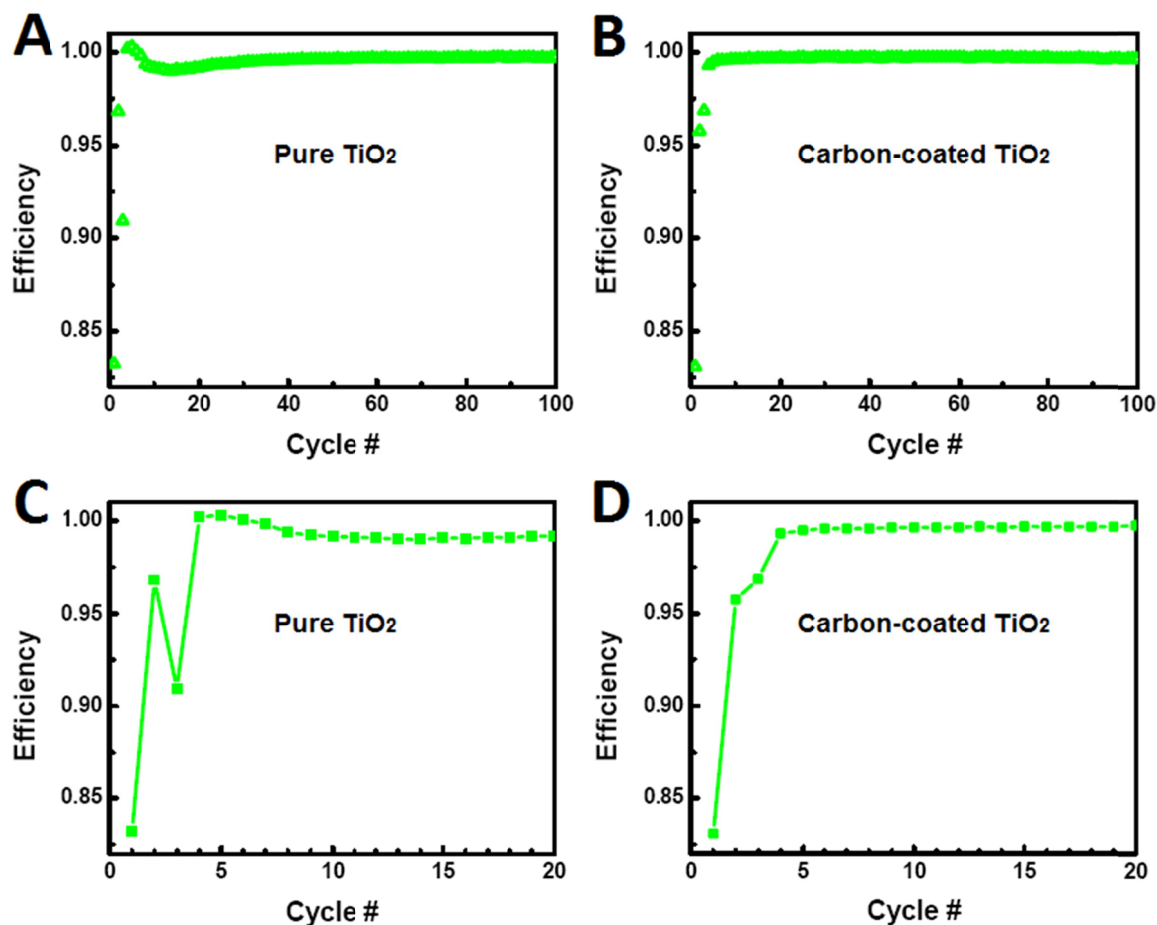


Figure 5.7. Variation of Coulombic efficiency along with the charge/discharge versus cycle number of the pure TiO₂ nanocrystals (A: the first 100 cycles, C: the first 20 cycles) and the carbon-coated TiO₂ nanocrystals. (B: the first 100 cycles, D: the first 20 cycles).

5.4.3 Rate Performance

The rate performances of the pure TiO₂ nanocrystals and the carbon-coated TiO₂ nanocrystals are shown in Figure 5.8 and Table 5.1. For the first 18 cycles of the rate performance test, the charge and discharge rates were changed simultaneously, and for the following cycles only the charge rates were changed while the discharge rate was kept

at 1C. As can be seen clearly, the discharge capacity decreased as the charge rate increased. Besides, the carbon-coated TiO₂ nanocrystals performed much better than the pure TiO₂ nanocrystals at the same rate condition, especially at high rates. For the first 18 cycles, the capacity of the carbon-coated TiO₂ nanocrystals was 58 mAh/g at 20C rate and 23 mAh/g at 50C rate, 65.7% and 228.6% higher than the value of the pure TiO₂ nanocrystals (35 mAh/g at 20C rate, 7 mAh/g at 50C rate), respectively. For the next 18 cycles, the discharge capacity of both samples increased compared to the case where both the charge/discharge rates were the same. Similar to the hydrogenated TiO₂ nanocrystals and the vacuum-treated TiO₂ nanocrystals, the carbon-coated TiO₂ nanocrystals had much higher discharge capacity than the pure TiO₂ nanocrystals, especially for the high rates. The capacity of the carbon-coated TiO₂ nanocrystals was 137 mAh/g at 20C rate and 103 mAh/g at 50C rate, 65.1% and 194.3% higher than the value of the pure TiO₂ nanocrystals (83 mAh/g at 20C rate, 35 mAh/g at 50C rate). The high charge rate makes fast charging possible. For example, it would take around 1 hour (1C rate) to charge for the pure TiO₂ nanocrystals, but only about 6 minutes (10C) for the carbon-coated TiO₂ nanocrystals. Apparently, the carbon-coated TiO₂ nanocrystals displayed a much better rate performance than the pure TiO₂ nanocrystals. It was possibly caused by the lower energy barrier of the transport of lithium-ions across the interface.

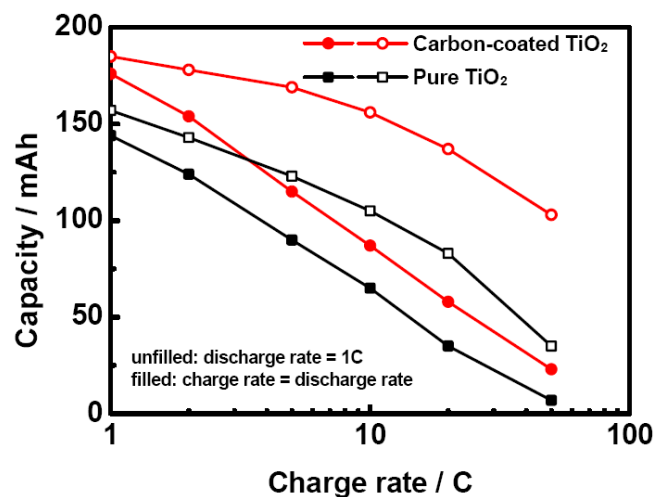


Figure 5.8. Comparison of the discharge capacities of the pure TiO₂ nanocrystals and the carbon-coated TiO₂ nanocrystals at various charge rates.

Table 5.1. Rate performance of the pure TiO₂ nanocrystals and the carbon-coated TiO₂ nanocrystals at various charge rates.

		Sample	1C	2C	5C	10C	20C	50C
Discharge capacity/ mAh/g	1-18 cycles	Pure ^a	144	124	90	65	35	7
	(Symmetric ^b)	Carbon ^c	176	154	115	87	58	23
	19-36 cycles	Pure ^a	157	143	123	105	83	35
	(Asymmetric ^d)	Carbon ^c	185	178	169	156	137	103

^aPure means the pure TiO₂ nanocrystals.

^bSymmetric means charge rate equals discharge rate.

^cCarbon means the carbon-coated TiO₂ nanocrystals.

^dAsymmetric means discharge rate equals 1C.

5.4.4 Analysis of Galvanostatic Charge/Discharge Profiles

The galvanostatic charge/discharge profiles for the first cycle at C/25 rate, 35th cycle at 1 C rate, and 100th cycle at 1C rate for the electrode made of the pure TiO₂ nanocrystals and the carbon-coated TiO₂ nanocrystals are shown in Figure 5.9 (A) and Figure 5.9 (B), respectively. It is easily seen that the carbon-coated TiO₂ nanocrystals had larger charge/discharge plateaus and smaller potential differences between the charge and discharge cycle than the pure TiO₂ nanocrystals in these cycles. The average potential difference between the charge and discharge cycle of the carbon-coated TiO₂ nanocrystals was about 0.10 V, 47.4% smaller than that of the pure TiO₂ nanocrystals (0.19 V). Same as the previous discussions, the smaller potential differences indicated the decreased charge transfer resistance and the larger charge/discharge plateaus suggested that the host matrix materials were effectively involved with the charge insertion/extraction during the charge/discharge processes. Overall, the charge transfer was smoother in the carbon-coated TiO₂ nanocrystals than that in the pure TiO₂ nanocrystals.

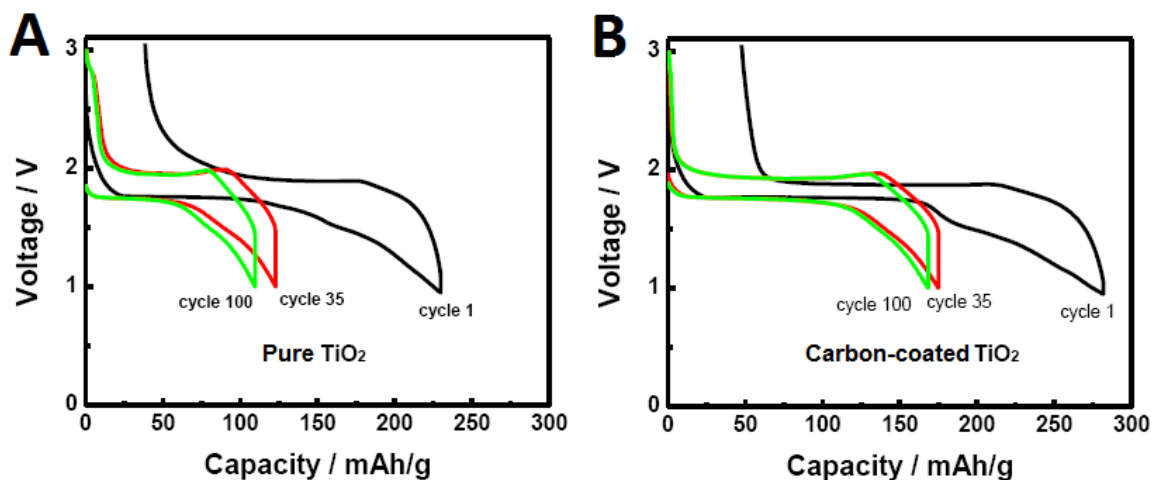


Figure 5.9. Galvanostatic charge/discharge profiles for the first cycle at C/25 rate, 35th cycle at 1 C rate, and 100th cycle at 1C rate for the electrode made of (A) the pure TiO₂ nanocrystals and (B) the carbon-coated TiO₂ nanocrystals.

The galvanostatic charge/discharge profiles at various charge rates for the electrode made of the pure TiO₂ nanocrystals and the carbon-coated TiO₂ nanocrystals are shown in Figure 5.10 (A) and Figure 5.10 (B), respectively. The carbon-coated TiO₂ nanocrystals showed both higher discharge capacity and larger charge/discharge plateaus between the charge/discharge cycles at each charge rate than the pure TiO₂ nanocrystals at the same rate. Again, that meant the charge transfer in the host matrix was smoother in the carbon-coated TiO₂ nanocrystals than in the pure TiO₂ nanocrystals.

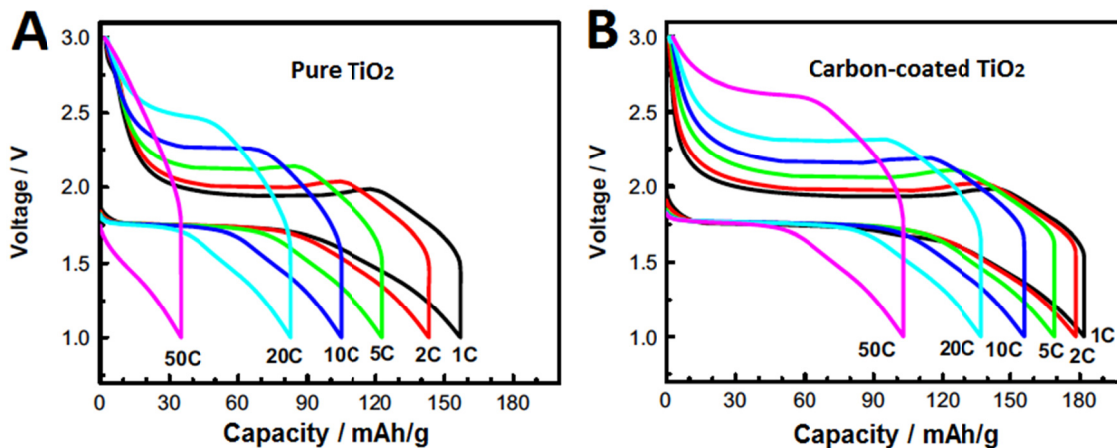


Figure 5.10. Galvanostatic charge/discharge profiles at various charge rates (discharge rate = 1C) for the electrode made of (A) the pure TiO₂ nanocrystals and (B) the carbon-coated TiO₂ nanocrystals.

Figure 5.11 shows the comparison of the galvanostatic charge/discharge profiles for the pure TiO₂ nanocrystals and the carbon-coated TiO₂ nanocrystals at charge rate of 20C. As discussed before, the discharge curve for the nanoporous anatase electrode could be divided into three voltage regions: region A (> 1.75 V), region B (≈ 1.75 V) and region C (< 1.75 V).^{91,121} In Figure 5.11, the carbon-coated TiO₂ nanocrystals had a larger region B (voltage plateau) and region C than the pure TiO₂ nanocrystals. As reported previously, the increase of region B (due to the shorter diffusion length) and region C (due to the larger interfacial area) could be attributed to the reduction of particle size.⁹¹ According to the TEM (Figure 5.1) and XRD results, both samples had a similar particle size. Thus, the increase of region B and region C of the carbon-coated TiO₂ nanocrystals over the pure TiO₂ nanocrystals was not mainly caused by particle size, but by the newly introduced layer of the carbon-coated TiO₂ nanocrystals. It could be seen

clearly that the rough surface of the carbon-coated layer from Figure 5.1 (D). The carbon-coated TiO₂ nanocrystals might have provided many edges and corners that could have increased the surface area for accommodating more lithium-ions during the charge/discharge processes. Further more, the thin carbon layer could have possibly increased the electric conductivity of the particle, thereby increasing the discharge capacity of the electrode.

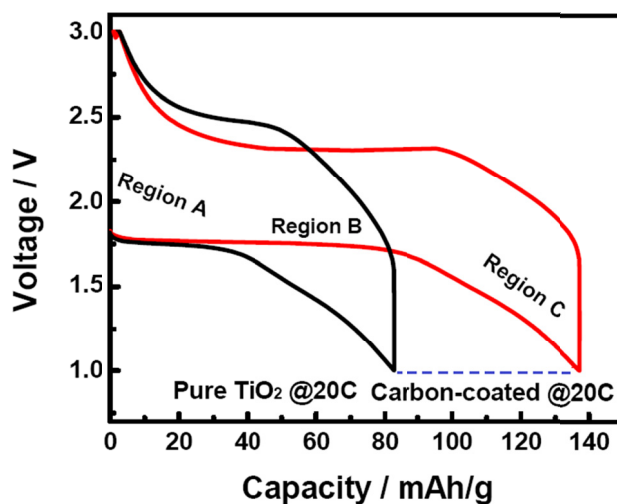


Figure 5.11. Comparison of the galvanostatic charge/discharge profiles for the pure TiO₂ nanocrystals and the carbon-coated TiO₂ nanocrystals at charge rate of 50C.

5.5 EIS Analysis

In order to analyze the charge transfer process across the cell, an electrochemical impedance study was performed on both samples at the same condition (Figure 5.12). All cells were cycled for two cycles and 50% discharged before EIS measurements. The equivalent circuit modeling used to fit the EIS is shown in Scheme 5.1. The fitting results

are listed in Table 5.2. R_S represents the ohmic resistance, including the bulk resistance of the electrolyte, separator, and the electrode. R_l represents the charge transfer resistance at the TiO₂/carbon/electrolyte interface. R_{cpe} represents the lithium-ion transport resistance at the TiO₂/carbon/electrolyte interface. W_o-R is the Warburg charge diffusion resistance in the TiO₂ electrode. W_o-T is Warburg diffusion time, which equals L^2/D in the electrode, where L is the length of the diffusion layer in the electrode and D is the diffusion coefficient in the electrode. W_o-P is the Warburg exponent. C_l is the space charge capacitance at the carbon/electrode interface. $CPE-T$ represents the time constant component of the constant phase element (CPE), which is approximate to the double layer charge capacitance in the TiO₂/electrolyte interface. $CPE-P$ represents the exponential part of the constant phase element.

The fitting results showed that the charge and lithium-ion transport resistances of the carbon-coated TiO₂ nanocrystals were smaller than those of the pure TiO₂ nanocrystals. The ohmic resistance of the carbon-coated TiO₂ nanocrystals was slightly reduced, which suggested that the electrical contact between the electrode materials and the copper coil of the carbon-coated TiO₂ nanocrystals was better than that of the pure TiO₂ nanocrystals. The charge transfer resistance (R_l) at the carbon/TiO₂ electrode interface was reduced by the carbon-coated surface layer from 5.6 Ω to 4.1 Ω, accompanied by the space charge capacitance (C_l) decreased from 1.60E-5 F to 1.56E-5 F. The lithium-ion transport resistance (R_{cpe}) was reduced by the carbon-coated surface layer from 104.7 Ω to 48.2 Ω, accompanied by a slight increase of double layer charge capacitance ($CPE-T$) from 1.70E-5 F to 1.72E-5 F. The Warburg charge diffusion resistance of the carbon-coated

TiO₂ nanocrystals was 41.6 Ω, while the value of the pure TiO₂ nanocrystals was 56.5 Ω. The smaller charge resistance could be attributed to the possible oxygen vacancy layer created during the vacuum decomposition-deposition process by the reduction of TiO₂ with carbon at a high temperature.²¹⁰ As oxygen vacancies have been shown to lower the charge transfer resistance, their existence could help improve the electronic conductivity.^{91,199} From the EIS analysis, because of the lower charge and lithium-ion transport resistances, the carbon-coated TiO₂ nanocrystals were supposed to possess better battery performances than the pure TiO₂ nanocrystals. This speculation was consistent with the battery test results.

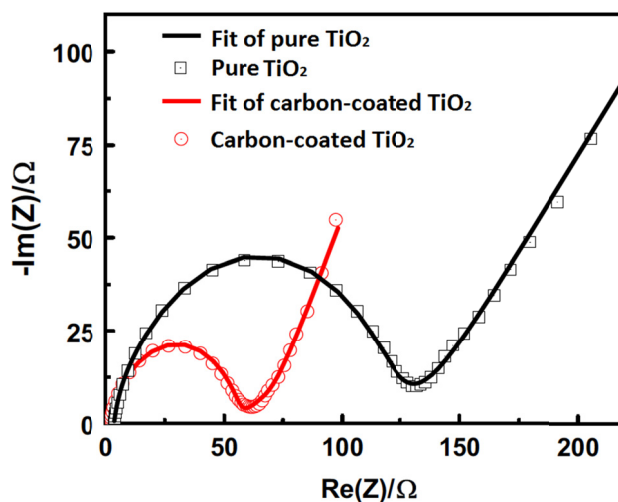
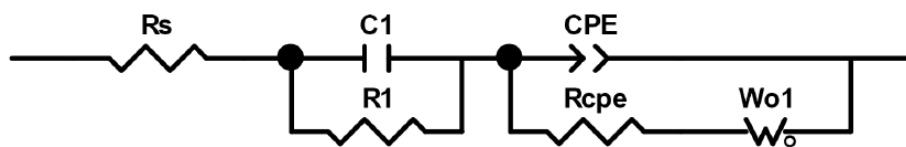


Figure 5.12. EIS of the pure TiO₂ nanocrystals and the carbon-coated TiO₂ nanocrystals.



Scheme 5.1. The equivalent circuit modeling used to fit the EIS.

Table 5.2. The fitted EIS results from the equivalent circuits.

	R_s/Ω	R_1/Ω	R_{cpe}/Ω	W_{o-R}	W_{o-T}	W_{o-P}	C_1/F	$CPE-T/F$	$CPE-P$
Pure ^a	3.73	5.6	104.7	56.6	3.3	0.26	1.60E-5	1.70E-5	0.86
Carbon ^b	2.17	4.1	48.2	41.6	9.1	0.33	1.56E-5	1.72E-5	0.88

^aPure means the pure TiO₂ nanocrystals.

^bCarbon means the carbon-coated TiO₂ nanocrystals.

5.6 Relationships between Structure and Battery Performances

As illustrated in Figure 5.13, a thin carbon layer was obtained for the carbon-coated TiO₂ nanocrystals by the vacuum decomposition-deposition treatment of the pure TiO₂ nanocrystals. According to the TEM (Figure 5.1) and XRD results, both samples had a similar particle size around 10 nm. Different from the pure TiO₂ nanocrystals, the carbon-coated TiO₂ nanocrystals were covered or embedded with an amorphous carbon outer layer. The Raman spectra (Figure 5.3) of both samples could easily differentiate the structural differences. The TGA results further quantitated the amount of the amorphous carbon (4.6 wt%). Both samples were used as an electrode material in half-cells and their cycling performances were tested thereafter. The carbon-coated TiO₂ nanocrystals had

better battery performances than the pure TiO_2 nanocrystals in terms of discharge capacity, Coulombic efficiency, and rate performance. It meant that the vacuum decomposition-deposition treatment could have facilitated the charge transfer and the capacity retention of the electrodes.

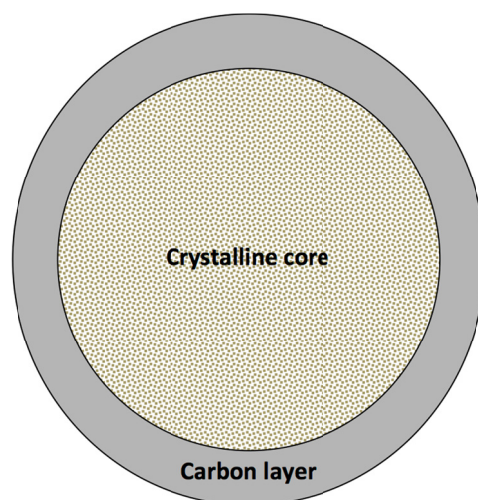


Figure 5.13. Illustration of a thin carbon layer on the crystalline core of the carbon-coated TiO_2 nanocrystals.

5.6.1 Structural Tolerance

As can be seen in the high-resolution TEM (Figure 5.1 (D)), the carbon-coated TiO_2 nanocrystals had a large rough surface. Similar to the hydrogenated TiO_2 nanocrystals and the vacuum-treated TiO_2 nanocrystals, in the carbon-coated TiO_2 nanocrystals, there might have many edges and corners that could have increased the surface area for accommodating more lithium-ions during the charge/discharge processes. Furthermore,

as the surface was disordered in the outer layer of the carbon-coated TiO₂ nanocrystals, the lattice might have less thermodynamically metastable energetic states than the pure TiO₂ nanocrystals. Thus, the penetration of lithium-ions into the lattice of the host matrix might have been enhanced. Therefore, the carbon-coated TiO₂ nanocrystals had lower lithium-ion transport resistance than the pure TiO₂ nanocrystals. The EIS analysis and the battery testing results further proved this speculation. However, for the pure TiO₂ nanocrystals, they had an ordered rigid surface that might not have provided a good interface to accommodate lithium-ions, causing a low discharge capacity (Figure 5.6 and Figure 5.9 (A)), a variable Coulombic efficiency (Figure 5.7 (C)), and a poor rate performance (Figure 5.8 and Figure 5.10 (A)). Also, due to the large structural distortion tolerance, the carbon-coated TiO₂ nanocrystals could have accommodated lithium-ions much more easily, providing high a discharge capacity (Figure 5.6 and Figure 5.9 (B)), a stable Coulombic efficiency (Figure 5.7 (D)), and a great rate performance (Figure 5.8 and Figure 5.10 (B)).

5.6.2 Carbon-Coated Layer

As low conductivity is one of the two major difficulties that hinder the intercalation and extraction of lithium-ions in TiO₂,²¹ the improvement of conductivity could have a positive influence on the battery performances. Hence, the carbon-coated TiO₂ nanocrystals that contained 4.6 wt% of amorphous carbon could be possible to improve the conductivity of the TiO₂ nanocrystals. Furthermore, as reported by Park et al.,¹⁴¹ the

thin carbon layer could serve as a dispersant to prevent agglomerations. This could also be another explanation for the improvement.

Similar to the vacuum-treated TiO₂ nanocrystals, the carbon-coated TiO₂ nanocrystals went through a vacuum treatment process. Thus, the oxygen vacancies might have been created by the reduction of TiO₂ with carbon at a high temperature.²¹⁰ As discussed in Chapter 5, the oxygen vacancies had shown the ability to lower the charge transfer resistance due to the existence of the BIEF.

5.7 Summary

In this chapter, the vacuum decomposition-deposition treatment was used as the third modification method to improve the battery performances of TiO₂ nanocrystals. After this treatment process, the pure TiO₂ nanocrystals were converted to the carbon-coated TiO₂ nanocrystals. A disordered amorphous layer containing around 4.6 wt% carbon was covered on the crystalline core. Compared with the pure TiO₂ nanocrystals, the carbon-coated TiO₂ nanocrystals displayed a better discharge capacity (166 mAh/g after 100 cycles), a near 100% Coulombic efficiency without noticeable degradation, and an improved high-rate performance.

The analysis of the galvanostatic charge/discharge profiles indicated that the amorphous carbon layer of the carbon-coated TiO₂ nanocrystals possessed a weaker chemical bonding between the transferred charge and host matrix. It also provided a larger charge transfer depth. The large structural tolerance of the carbon-coated TiO₂ nanocrystals could be one possible explanation to the improvement. Furthermore, this

improvement could also be attributed to the improvement of conductivity after the introduction of carbon and the carbon layer could be served as a dispersant to prevent agglomerations.¹⁴¹ As the carbon-coated TiO₂ nanocrystals went through a vacuum treatment, the oxygen vacancies might have been created to during this process and helped lower the charge transfer resistance in the amorphous carbon layer.

CHAPTER 6

CONCLUSION

6.1 Structural Similarity

Three kinds of the modified TiO₂ nanocrystals were discussed in this dissertation. According to the study of the structural and electronic properties, the hydrogenated TiO₂ nanocrystals, the vacuum-treated TiO₂ nanocrystals, and the carbon-coated TiO₂ nanocrystals all showed a disordered amorphous outer layer covering on the crystalline core. The battery performance tests showed that the three modified TiO₂ nanocrystals had better discharge capacity, Coulombic efficiency, and rate performance than the pure TiO₂ nanocrystals, which indicated that these disordered amorphous outer layer played a role in improving the battery performances.

6.2 Mechanism Differences of Improved Battery Performances

Although all the three modified TiO₂ nanocrystals had a disordered amorphous outer layer and showed the improvement of the battery performances, the reasons for the improvement were different. Through hydrogenating of the pure TiO₂ nanocrystals, the hydrogenated TiO₂ nanocrystals were generated by the incorporation of hydrogen under a high pressure and an elevated temperature. Meanwhile, their arrangement of the atoms on the surface layers were changed compared to the pure TiO₂ nanocrystals. This

disordered amorphous outer layer possessed the structural tolerance to accommodate more lithium-ions. Also, it might have provided a possibility of the faster ion exchange and hydrogen mobility that helped realize better charge transfer efficiency and capacity retention efficiency.

When the pure TiO₂ nanocrystals underwent a vacuum treatment at a relatively low vacuum level (1-2 mTorr) and a low temperature (500 °C), a disordered amorphous outer layer that contained the oxygen vacancies was generated. The new modified TiO₂ nanocrystals are called the vacuum-treated TiO₂ nanocrystals. This special outer layer provided not only the structural tolerance to accommodate more lithium-ions, but also the oxygen vacancies to form a BIEF that facilitated the transport of lithium-ions during the charge/discharge processes.

As for the carbon-coated TiO₂ nanocrystals, they were converted under a vacuum decomposition-deposition treatment process of the pure TiO₂ nanocrystals. Similar to the hydrogenated TiO₂ nanocrystals and the vacuum-treated TiO₂ nanocrystals, the carbon-coated TiO₂ nanocrystals that contained a special disordered outer layer, possessed the structural tolerance to accommodate more lithium-ions. Meanwhile, as carbon was introduced during this treatment, this layer also contained carbon that might have played a role in improving the conductivity of the TiO₂ nanocrystals, as well as served as dispersant to prevent agglomerations. Moreover, as the carbon-coated TiO₂ nanocrystals also underwent a vacuum treatment, the oxygen vacancies that could have formed a BIEF might have been created. As the BIEF could facilitate the transport of lithium-ions during

the charge/discharge processes, this could also be one possible reason to explain the improved battery performances.

6.3 Comparison of Battery Performances for Three TiO₂ Nanocrystals

The three modified TiO₂ nanocrystals had different performances of the improvements. For discharge capacity, the vacuum-treated TiO₂ nanocrystals and the carbon-coated TiO₂ nanocrystals performed better than the hydrogenated TiO₂ nanocrystals. After 100 cycles, the discharge capacity of the hydrogenated TiO₂ nanocrystals, the vacuum-treated TiO₂ nanocrystals, and carbon-coated TiO₂ nanocrystals was 138 mAh/g, 155 mAh/g, and 166 mAh/g, respectively. As for the Coulombic efficiency, both the hydrogenated TiO₂ nanocrystals and the vacuum-treated TiO₂ nanocrystals had the efficiency of 99.9% after 100 cycles, while the value of the carbon-coated TiO₂ nanocrystals was 99.7%. In general, the vacuum-treated TiO₂ nanocrystals and the carbon-coated TiO₂ nanocrystals had better rate performance than the hydrogenated TiO₂ nanocrystals regardless of the symmetry of the charge and discharge rates as shown in Figure 6.1 and Figure 6.2. At low charge rates (e.g. 1C), the carbon-coated TiO₂ nanocrystals had higher discharge capacities than the vacuum-treated TiO₂ nanocrystals. However, as the rates went higher (>2C), the vacuum-treated TiO₂ nanocrystals showed higher discharge capacities than the carbon-coated TiO₂ nanocrystals, which meant that the vacuum-treated TiO₂ nanocrystals were more suitable for high-rate applications, while the carbon-coated TiO₂ nanocrystals worked better for low-rate batteries.

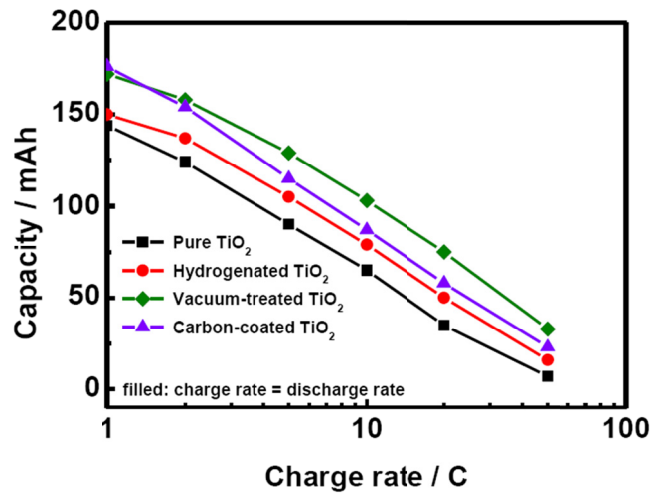


Figure 6.1. Comparison of rate performance for the four TiO₂ nanocrystals when discharge rate equaled charge rate.

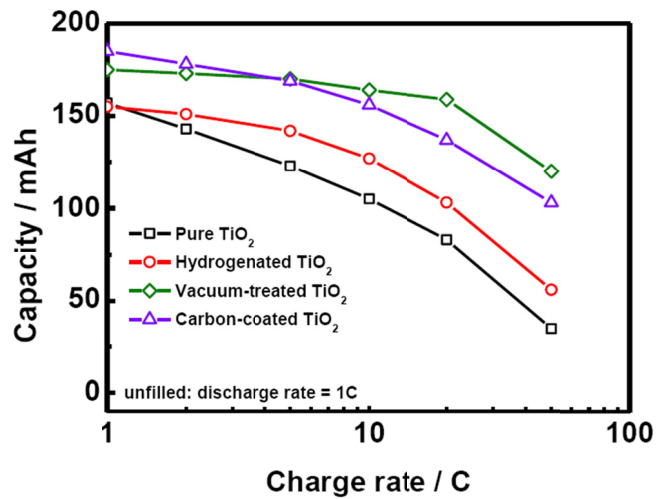


Figure 6.2. Comparison of rate performance for the four TiO₂ nanocrystals when discharge was kept at 1C.

When cycling number exceeded 100, although the three modified TiO₂ nanocrystals did not really break the maximum intercalation limitation of anatase (167.5 mAh/g, $x = 0.5$), the three modified TiO₂ nanocrystals did make big improvements compared to the pure TiO₂ nanocrystals. Most importantly, the three strategies used in this dissertation provide new ways to modify the surface of nanomaterials, which can be used in other applications as well as the battery development.

REFERENCES

1. Lewis, N. S.; Nocera, D. G. Powering the Planet: Chemical Challenges in Solar Energy Utilization. *Proc. Natl. Acad. Sci. U. S. A.* **2006**, *103*, 15729-15735.
2. Thompson, B. C.; Frechet, J. M. J. Polymer-Fullerene Composite Solar Cells. *Angew. Chem., Int. Ed.* **2008**, *47*, 58-77.
3. Deng, D.; Kim, M. G.; Lee, J. Y.; Cho, J. Green Energy Storage Materials: Nanostructured TiO₂ and Sn-Based Anodes for Lithium-Ion Batteries. *Energy Environ. Sci.* **2009**, *2*, 818-837.
4. Dong, H.; Zhu, H.; Meng, Q.; Gong, X.; Hu, W. Organic Photoresponse Materials and Devices. *Chem. Soc. Rev.* **2012**, *41*, 1754-1808.
5. Lv, H.; Geletii, Y. V.; Zhao, C.; Vickers, J. W.; Zhu, G.; Luo, Z.; Song, J.; Lian, T.; Musaev, D. G.; Hill, C. L. Polyoxometalate Water Oxidation Catalysts and the Production of Green Fuel. *Chem. Soc. Rev.* **2012**, *41*, 7572-7589.
6. Whittingham, M. S. History, Evolution, and Future Status of Energy Storage. *Proc. IEEE* **2012**, *100*, 1518-1536.
7. Arico, A. S.; Bruce, P.; Scrosati, B.; Tarascon, J.-M.; van Schalkwijk, W. Nanostructured Materials for Advanced Energy Conversion and Storage Devices. *Nat. Mater.* **2005**, *4*, 366-377.
8. Vincent, C. A. Lithium Batteries: A 50-Year Perspective, 1959-2009. *Solid State Ionics* **2000**, *134*, 159-167.
9. Dell, R. M. Batteries-Fifty Years of Materials Development. *Solid State Ionics* **2000**, *134*, 139-158.
10. Goodenough, J. B.; Park, K.-S. The Li-Ion Rechargeable Battery: A Perspective. *J. Am. Chem. Soc.* **2013**, *135*, 1167-1176.
11. Yoshino, A. The Birth of the Lithium-Ion Battery. *Angew. Chem., Int. Ed.* **2012**, *51*, 5798-5800.
12. Armand, M.; Tarascon, J. M. Building Better Batteries. *Nature*. **2008**, *451*, 652-657.
13. Yang, Z.; Choi, D.; Kerisit, S.; Rosso, K. M.; Wang, D.; Zhang, J.; Graff, G.; Liu, J. Nanostructures and Lithium Electrochemical Reactivity of Lithium Titanites and Titanium Oxides: A Review. *J. Power Sources* **2009**, *192*, 588-598.

14. Scrosati, B. History of Lithium Batteries. *J. Solid State Electrochem.* **2011**, *15*, 1623-1630.
15. Leclanche, G. New Form of Galvanic Battery. *Compt. rend.* **1866**, *83*, 54-56.
16. Whittingham, M. S. Electrical Energy Storage and Intercalation Chemistry. *Science* **1976**, *192*, 1126-1127.
17. Whittingham, M. S. Lithium Batteries and Cathode Materials. *Chem. Rev.* **2004**, *104*, 4271-4301.
18. Panasonic. Panasonic LC-R1233P Specifications, 2010.
19. PowerSonic. PS, PSG and PSH General Purpose Battery Specifications, 2014.
20. Jiang, C.; Hosono, E.; Zhou, H. Nanomaterials for Lithium Ion Batteries. *Nano Today*, **2006**, *1*, 28-33.
21. Moriguchi, I.; Hidaka, R.; Yamada, H.; Kudo, T.; Murakami, H.; Nakashima, N. A. Mesoporous Nanocomposite of TiO₂ and Carbon Nanotubes as a High-Rate Li-Intercalation Electrode Material. *Adv. Mater.* **2006**, *18*, 69-73.
22. Weber, C. J.; Geiger, S.; Falusi, S.; Roth, M. Material Review of Li Ion Battery Separators. *AIP Conf. Proc.* **2014**, *1597*, 66-81.
23. Linden, D. *Handbook of Batteries and Fuel Cells*; McGraw-Hill Companies, Inc.: New York, 1984.
24. Yang, S.; Feng, X.; Zhi, L.; Cao, Q.; Maier, J.; Muellen, K. Nanographene-Constructed Hollow Carbon Spheres and Their Favorable Electroactivity with Respect to Lithium Storage. *Adv. Mater.* **2010**, *22*, 838-842.
25. Zhu, G.-N.; Wang, Y.-G.; Xia, Y.-Y. Ti-Based Compounds as Anode Materials for Li-Ion Batteries. *Energy Environ. Sci.* **2012**, *5*, 6652-6667.
26. Zhang, S. S. The Effect of the Charging Protocol on the Cycle Life of a Li-Ion Battery. *J. Power Sources* **2006**, *161*, 1385-1391.
27. Winter, M.; Besenhard, J. O.; Spahr, M. E.; Novak, P. Insertion Electrode Materials for Rechargeable Lithium Batteries. *Adv. Mater.* **1998**, *10*, 725-763.
28. Linden, D. *Handbook of batteries*; McGraw-Hill Companies, Inc: New York, 1995.
29. Luo, J.-Y.; Cui, W.-J.; He, P.; Xia, Y.-Y. Raising the Cycling Stability of Aqueous Lithium-Ion Batteries by Eliminating Oxygen in the Electrolyte. *Nat. Chem.* **2010**, *2*, 760-765.

30. Wang, Q.; Ping, P.; Zhao, X.; Chu, G.; Sun, J.; Chen, C. Thermal Runaway Caused Fire and Explosion of Lithium Ion Battery. *J. Power Sources* **2012**, *208*, 210-224.
31. Biensan, P.; Simon, B.; Pere, J. P.; de Guibert, A.; Broussely, M.; Bodet, J. M.; Perton, F. On Safety of Lithium-Ion Cells. *J. Power Sources* **1999**, *81-82*, 906-912.
32. Belharouak, I.; Sun, Y. K.; Lu, W.; Amine, K. On the Safety of the $\text{Li}_4\text{Ti}_5\text{O}_{12}/\text{LiMn}_2\text{O}_4$ Lithium-Ion Battery System. *J. Electrochem. Soc.* **2007**, *154*, A1083-A1087.
33. Venugopal, G.; Moore, J.; Howard, J.; Pandalwar, S. Characterization of Microporous Separators for Lithium-Ion Batteries. *J. Power Sources*. **1999**, *77*, 34-41.
34. Tobishima, S.-i.; Yamaki, J.-i. A Consideration of Lithium Cell Safety. *J. Power Sources* **1999**, *81-82*, 882-886.
35. Scrosati, B. Recent Advances in Lithium Ion Battery Materials. *Electrochim. Acta* **2000**, *45*, 2461-2466.
36. Holleck, G. L.; Driscoll, J. R. Transition Metal Sulfides as Cathodes for Secondary Lithium Batteries. II. Titanium Sulfides. *Electrochim. Acta* **1977**, *22*, 647-655.
37. Whittingham, M. S. Chemistry of Intercalation Compounds: Metal Guests in Chalcogenide Hosts. *Prog. Solid State Chem.* **1978**, *12*, 41-99.
38. Haering, R. R.; Stiles, J. A. R.; Brandt, K. Lithium Molybdenum Disulfide Battery Cathode. U. S. Patent 4,224,390, September 23, 1980.
39. Murphy, D. W.; Trumbore, F. A. The Chemistry of Titanium Sulfide (TiS_3) and Niobium Selenide (NbSe_3) Cathodes. *J. Electrochem. Soc.* **1976**, *123*, 960-964.
40. Whittingham, M. S. The Role of Ternary Phases in Cathode Reactions. *J. Electrochem. Soc.* **1976**, *123*, 315-320.
41. Dampier, F. W. Cathodic Behavior of Copper Sulfide, Molybdenum Trioxide, and Manganese Dioxide in Lithium Cells. *J. Electrochem. Soc.* **1974**, *121*, 656-60.
42. Fergus, J. W. Recent Developments in Cathode Materials for Lithium Ion Batteries. *J. Power Sources* **2010**, *195*, 939-954.
43. Mizushima, K.; Jones, P. C.; Wiseman, P. J.; Goodenough, J. B. Lithium Cobalt Oxide(Li_xCoO_2) ($0 < x \leq 1$): A New Cathode Material for Batteries of High Energy Density. *Mater. Res. Bull.* **1980**, *15*, 783-789.

44. Koksang, R.; Barker, J.; Shi, H.; Saiedi, M. Y. Cathode Materials for Lithium Rocking Chair Batteries. *Solid State Ionics* **1996**, *84*, 1-21.
45. Tarascon, J. M.; Armand, M. Issues and Challenges Facing Rechargeable Lithium Batteries. *Nature* **2001**, *414*, 359-367.
46. Li, H.; Wang, Z.; Chen, L.; Huang, X. Research on Advanced Materials for Li-Ion Batteries. *Adv. Mater.* **2009**, *21*, 4593-4607.
47. Amatucci, G. G.; Tarascon, J. M.; Klein, L. C. Cobalt Dissolution in LiCoO₂-Based Non-Aqueous Rechargeable Batteries. *Solid State Ionics* **1996**, *83*, 167-173.
48. Ohzuku, T.; Ueda, A. Solid-State Redox Reactions of LiCoO₂ ($\bar{R}3m$) for 4 Volt Secondary Lithium Cells. *J. Electrochem. Soc.* **1994**, *141*, 2972-2977.
49. Cho, J.; Kim, C.-S.; Yoo, S.-I. Improvement of Structural Stability of LiCoO₂ Cathode During Electrochemical Cycling by Sol-Gel Coating of SnO₂. *Electrochem. Solid-State Lett.* **2000**, *3*, 362-365.
50. Cho, J.; Kim, Y. J.; Park, B. Novel LiCoO₂ Cathode Material with Al₂O₃ Coating for a Li Ion Cell. *Chem. Mater.* **2000**, *12*, 3788-3791.
51. Kweon, H.-J.; Park, D. G. Surface Modification of LiSr_{0.002}Ni_{0.9}Co_{0.1}O₂ by Overcoating with a Magnesium Oxide. *Electrochem. Solid-State Lett.* **2000**, *3*, 128-130.
52. Sato, H.; Takahashi, D.; Nishina, T.; Uchida, I. Electrochemical Characterization of Thin-Film LiCoO₂ Electrodes in Propylene Carbonate Solutions. *J. Power Sources* **1997**, *68*, 540-544.
53. Barker, J.; Pynenburg, R.; Koksang, R.; Saiedi, M. Y. An Electrochemical Investigation into the Lithium Insertion Properties of Li_xCoO₂. *Electrochim. Acta* **1996**, *41*, 2481-2488.
54. Wang, Y.; Cao, G. Developments in Nanostructured Cathode Materials for High-Performance Lithium-Ion Batteries. *Adv. Mater.* **2008**, *20*, 2251-2269.
55. Ohzuku, T.; Ueda, A.; Kouguchi, M. Synthesis and Characterization of LiAl_{1/4}Ni_{3/4}O₂ ($\bar{R}3m$) for Lithium-Ion (Shuttlecock) Batteries. *J. Electrochem. Soc.* **1995**, *142*, 4033-4039.
56. Thackeray, M. M.; de Kock, A.; David, W. I. F. Synthesis and Structural Characterization of Defect Spinels in the Lithium-Manganese-Oxide System. *Mater. Res. Bull.* **1993**, *28*, 1041-1049.

57. Padhi, A. K.; Nanjundaswamy, K. S.; Goodenough, J. B. Phospho-Olivines as Positive-Electrode Materials for Rechargeable Lithium Batteries. *J. Electrochem. Soc.* **1997**, *144*, 1188-1194.
58. Ellis, B. L.; Lee, K. T.; Nazar, L. F. Positive Electrode Materials for Li-Ion and Li Batteries. *Chem. Mater.* **2010**, *22*, 691-714.
59. Liu, Y.; Mi, C.; Yuan, C.; Zhang, X. Improvement of Electrochemical and Thermal Stability of LiFePO₄ Cathode Modified by CeO₂. *J. Electroanal. Chem.* **2009**, *628*, 73-80.
60. Mukherjee, R.; Krishnan, R.; Lu, T.-M.; Koratkar, N. Nanostructured Electrodes for High-Power Lithium Ion Batteries. *Nano Energy* **2012**, *1*, 518-533.
61. Shi, X.; Wang, C.; Ma, X.; Sun, J. Synthesis and Electrochemical Properties of LiNi_{0.9}Co_{0.1}O₂ Cathode Material for Lithium Secondary Battery. *Mater. Chem. Phys.* **2009**, *113*, 780-783.
62. Lee, D. G.; Gupta, R. K.; Cho, Y. S.; Hwang, K. T. Improved Electrochemical Properties of Li(Ni_{0.7}Co_{0.3})O₂ Cathode for Lithium Ion Batteries with Controlled Sintering Conditions. *J. Appl. Electrochem.* **2009**, *39*, 671-679.
63. Wang, L.; Li, J.; He, X.; Pu, W.; Wan, C.; Jiang, C. Recent Advances in Layered LiNi_xCo_yMn_{1-x-y}O₂ Cathode Materials for Lithium Ion Batteries. *J. Solid State Electrochem.* **2009**, *13*, 1157-1164.
64. Wu, Y.; Manthiram, A. Structural Stability of Chemically Delithiated Layered (1-z)Li[Li_{1/3}Mn_{2/3}]O_{2-z}Li[Mn_{0.5-y}Ni_{0.5-y}Co_{2y}]O₂ Solid Solution Cathodes. *J. Power Sources* **2008**, *183*, 749-754.
65. Albertus, P.; Christensen, J.; Newman, J. Experiments on and Modeling of Positive Electrodes with Multiple Active Materials for Lithium-Ion Batteries. *J. Electrochem. Soc.* **2009**, *156*, A606-A618.
66. Chikkannanavar, S. B.; Bernardi, D. M.; Liu, L. A Review of Blended Cathode Materials for Use in Li-Ion Batteries. *J. Power Sources* **2014**, *248*, 91-100.
67. Buiel, E.; Dahn, J. R. Li-Insertion in Hard Carbon Anode Materials for Li-Ion Batteries. *Electrochim. Acta* **1999**, *45*, 121-130.
68. Yazami, R.; Touzain, P. A Reversible Graphite-Lithium Anode for Batteries. *J. Power Sources* **1983**, *9*, 365-371.
69. Yoshino, A.; Sanechika, K.; Nakajima, T. Secondary Battery with Nonaqueous Electrolyte. European Patent 205,856, December 30, 1986.

70. Xu, K. Nonaqueous Liquid Electrolytes for Lithium-Based Rechargeable Batteries. *Chem. Rev.* **2004**, *104*, 4303-4417.
71. Yamaura, J.; Ozaki, Y.; Morita, A.; Ohta, A. High Voltage, Rechargeable Lithium Batteries Using Newly Developed Carbon for Negative Electrode Material. *J. Power Sources* **1993**, *43*, 233-239.
72. Mabuchi, A. A Survey on the Carbon Anode Materials for Rechargeable Lithium Batteries. *Tanso* **1994**, *165*, 298-306.
73. Dahn, J. R.; Zheng, T.; Liu, Y.; Xue, J. S. Mechanisms for Lithium Insertion in Carbonaceous Materials. *Science* **1995**, *270*, 590-593.
74. Azuma, H.; Imoto, H.; Yamada, S. i.; Sekai, K. Advanced Carbon Anode Materials for Lithium Ion Cells. *J. Power Sources* **1999**, *81-82*, 1-7.
75. de las Casas, C.; Li, W. A Review of Application of Carbon Nanotubes for Lithium Ion Battery Anode Material. *J. Power Sources* **2012**, *208*, 74-85.
76. Tatsumi, K.; Iwashita, N.; Sakaebe, H.; Shioyama, H.; Higuchi, S.; Mabuchi, A.; Fujimoto, H. The Influence of the Graphitic Structure on the Electrochemical Characteristics for the Anode of Secondary Lithium Batteries. *J. Electrochem. Soc.* **1995**, *142*, 716-720.
77. Yoshio, M.; Wang, H.; Fukuda, K. Spherical Carbon-Coated Natural Graphite as a Lithium-Ion Battery-Anode Material. *Angew. Chem., Int. Ed.* **2003**, *42*, 4203-4206.
78. Endo, M.; Kim, C.; Nishimura, K.; Fujino, T.; Miyashita, K. Recent Development of Carbon Materials for Li Ion Batteries. *Carbon* **2000**, *38*, 183-197.
79. Tirado, J. L. Inorganic Materials for the Negative Electrode of Lithium-Ion Batteries: State-of-the-Art and Future Prospects. *Mater. Sci. Eng., R* **2003**, *40*, 103-136.
80. Candelaria, S. L.; Shao, Y.; Zhou, W.; Li, X.; Xiao, J.; Zhang, J.-G.; Wang, Y.; Liu, J.; Li, J.; Cao, G. Nanostructured Carbon for Energy Storage and Conversion. *Nano Energy* **2012**, *1*, 195-220.
81. Sandhya, C. P.; John, B.; Gouri, C. Lithium Titanate as Anode Material for Lithium-Ion Cells: A Review. *Ionics* **2014**, *20*, 601-620.
82. Etacheri, V.; Marom, R.; Elazari, R.; Salitra, G.; Aurbach, D. Challenges in the Development of Advanced Li-Ion Batteries: A Review. *Energy Environ. Sci.* **2011**, *4*, 3243-3262.

83. Shen, L.; Zhang, X.; Uchaker, E.; Yuan, C.; Cao, G. $\text{Li}_4\text{Ti}_5\text{O}_{12}$ Nanoparticles Embedded in a Mesoporous Carbon Matrix as a Superior Anode Material for High Rate Lithium Ion Batteries. *Adv. Energy Mater.* **2012**, *2*, 691-698.
84. Yi, T.-F.; Jiang, L.-J.; Shu, J.; Yue, C.-B.; Zhu, R.-S.; Qiao, H.-B. Recent Development and Application of $\text{Li}_4\text{Ti}_5\text{O}_{12}$ as Anode Material of Lithium Ion Battery. *J. Phys. Chem. Solids* **2010**, *71*, 1236-1242.
85. Besenhard, J. O.; Yang, J.; Winter, M. Will Advanced Lithium-Alloy Anodes Have a Chance in Lithium-Ion Batteries? *J. Power Sources* **1997**, *68*, 87-90.
86. Bruce, P. G.; Scrosati, B.; Tarascon, J.-M. Nanomaterials for Rechargeable Lithium Batteries. *Angew. Chem., Int. Ed.* **2008**, *47*, 2930-2946.
87. Hassoun, J.; Panero, S.; Simon, P.; Taberna, P. L.; Scrosati, B. High-Rate, Long-Life Ni-Sn Nanostructured Electrodes for Lithium-Ion Batteries. *Adv. Mater.* **2007**, *19*, 1632-1635.
88. Chen, J. S.; Lou, X. W. SnO_2 and TiO_2 Nanosheets for Lithium-Ion Batteries. *Mater. Today* **2012**, *15*, 246-254.
89. Fan, J.; Wang, T.; Yu, C.; Tu, B.; Jiang, Z.; Zhao, D. Ordered, Nanostructured Tin-Based Oxides/Carbon Composite as the Negative-Electrode Material for Lithium-Ion Batteries. *Adv. Mater.* **2004**, *16*, 1432-1436.
90. Lou, X. W.; Wang, Y.; Yuan, C.; Lee, J. Y.; Archer, L. A. Template-Free Synthesis of SnO_2 Hollow Nanostructures with High Lithium Storage Capacity. *Adv. Mater.* **2006**, *18*, 2325-2329.
91. Shin, J.-Y.; Samuelis, D.; Maier, J. Sustained Lithium-Storage Performance of Hierarchical, Nanoporous Anatase TiO_2 at High Rates: Emphasis on Interfacial Storage Phenomena. *Adv. Funct. Mater.* **2011**, *21*, 3464-3472.
92. Guyomard, D.; Tarascon, J. M. Lithium Metal-Free Rechargeable Lithium Manganese Oxide (LiMn_2O_4)/Carbon Cells: Their Understanding and Optimization. *J. Electrochem. Soc.* **1992**, *139*, 937-948.
93. Zhang, S. S. A Review on Electrolyte Additives for Lithium-Ion Batteries. *J. Power Sources* **2006**, *162*, 1379-1394.
94. Verma, P.; Maire, P.; Novak, P. A Review of the Features and Analyses of the Solid Electrolyte Interphase in Li-Ion Batteries. *Electrochim. Acta* **2010**, *55*, 6332-6341.
95. Chen, Z.; Belharouak, I.; Sun, Y. K.; Amine, K. Titanium-Based Anode Materials for Safe Lithium-Ion Batteries. *Adv. Funct. Mater.* **2013**, *23*, 959-969.

96. Scrosati, B.; Garche, J. Lithium Batteries: Status, Prospects and Future. *J. Power Sources* **2010**, *195*, 2419-2430.
97. Smijs, T. G.; Pavel, S. Titanium Dioxide and Zinc Oxide Nanoparticles in Sunscreens: Focus on Their Safety and Effectiveness. *Nanotechnol., Sci. Appl.* **2011**, *4*, 95-112.
98. Yuan, S.; Chen, W.; Hu, S. Fabrication of TiO₂ Nanoparticles/Surfactant Polymer Complex Film on Glassy Carbon Electrode and Its Application to Sensing Trace Dopamine. *Mater. Sci. Eng., C* **2005**, *25*, 479-485.
99. Fujishima, A.; Honda, K. Electrochemical Photolysis of Water at a Semiconductor Electrode. *Nature* **1972**, *238*, 37-38.
100. O'Regan, B.; Graetzel, M. A Low-Cost, High-Efficiency Solar Cell Based on Dye-Sensitized Colloidal Titanium Dioxide Films. *Nature* **1991**, *353*, 737-740.
101. Linsebigler, A. L.; Lu, G.; Yates, J. T., Jr. Photocatalysis on TiO₂ Surfaces: Principles, Mechanisms, and Selected Results. *Chem. Rev.* **1995**, *95*, 735-758.
102. Fujishima, A.; Rao, T. N.; Tryk, D. A., Titanium Dioxide Photocatalysis. *J. Photochem. Photobiol., C* **2000**, *1*, 1-21.
103. Muscat, J.; Swamy, V.; Harrison, N. M. First-Principles Calculations of the Phase Stability of TiO₂. *Phys. Rev. B Condens. Matter Mater. Phys.* **2002**, *65*, 224112/1-224112/15.
104. Ovenstone, J.; Yanagisawa, K. Effect of Hydrothermal Treatment of Amorphous Titania on the Phase Change from Anatase to Rutile during Calcination. *Chem. Mater.* **1999**, *11*, 2770-2774.
105. Jellison, G. E., Jr.; Boatner, L. A.; Budai, J. D.; Jeong, B. S.; Norton, D. P. Spectroscopic Ellipsometry of Thin Film and Bulk Anatase (TiO₂). *J. Appl. Phys.* **2003**, *93*, 9537-9541.
106. Tang, H.; Prasad, K.; Sanilines, R.; Schmid, P. E.; Levy, F. Electrical and Optical Properties of TiO₂ Anatase Thin Films. *J. Appl. Phys.* **1994**, *75*, 2042-2047.
107. Foger, K.; Anderson, J. R. Thermally Stable SMSI Supports: Iridium Supported on Titania-Alumina and on Cerium-Stabilized Anatase. *Appl. Catal.* **1986**, *23*, 139-155.
108. Zhang, F.; Zheng, Z.; Ding, X.; Mao, Y.; Chen, Y.; Zhou, Z.; Yang, S.; Liu, X. Highly Oriented Rutile-Type TiO₂ Films Synthesized by Ion Beam Enhanced Deposition. *J. Vac. Sci. Technol., A* **1997**, *15*, 1824-1827.

109. Alivisatos, A. P. Perspectives on the Physical Chemistry of Semiconductor Nanocrystals. *J. Phys. Chem.* **1996**, *100*, 13226-13239.
110. Chen, X.; Lou, Y.; Dayal, S.; Qiu, X.; Krolicki, R.; Burda, C.; Zhao, C.; Becker, J. Doped Semiconductor Nanomaterials. *J. Nanosci. Nanotechnol.* **2005**, *5*, 1408-1420.
111. Chen, X.; Mao, S. S., Titanium Dioxide Nanomaterials: Synthesis, Properties, Modifications, and Applications. *Chem. Rev.* **2007**, *107*, 2891-2959.
112. Shin, J.-Y.; Joo, J. H.; Samuelis, D.; Maier, J. Oxygen-Deficient TiO_{2- δ} Nanoparticles via Hydrogen Reduction for High Rate Capability Lithium Batteries. *Chem. Mater.* **2012**, *24*, 543-551.
113. Lindstroem, H.; Soedergren, S.; Solbrand, A.; Rensmo, H.; Hjelm, J.; Hagfeldt, A.; Lindquist, S.-E. Li⁺ Ion Insertion in TiO₂ (Anatase). 2. Voltammetry on Nanoporous Films. *J. Phys. Chem. B* **1997**, *101*, 7717-7722.
114. Van de Krol, R.; Goossens, A.; Meulenkamp, E. A. In Situ X-Ray Diffraction of Lithium Intercalation in Nanostructured and Thin Film Anatase TiO₂. *J. Electrochem. Soc.* **1999**, *146*, 3150-3154.
115. Graetz, J.; Ahn, C. C.; Yazami, R.; Fultz, B. Highly Reversible Lithium Storage in Nanostructured Silicon. *Electrochem. Solid-State Lett.* **2003**, *6*, A194-A197.
116. Han, H.; Song, T.; Lee, E.-K.; Devadoss, A.; Jeon, Y.; Ha, J.; Chung, Y.-C.; Choi, Y.-M.; Jung, Y.-G.; Paik, U. Dominant Factors Governing the Rate Capability of a TiO₂ Nanotube Anode for High Power Lithium Ion Batteries. *ACS Nano* **2012**, *6*, 8308-8315.
117. Xu, J.; Wang, Y.; Li, Z.; Zhang, W. F. Preparation and Electrochemical Properties of Carbon-Doped TiO₂ Nanotubes as an Anode Material for Lithium-Ion Batteries. *J. Power Sources* **2008**, *175*, 903-908.
118. Li, J.; Tang, Z.; Zhang, Z. Preparation and Novel Lithium Intercalation Properties of Titanium Oxide Nanotubes. *Electrochem. Solid-State Lett.* **2005**, *8*, A316-A319.
119. Armstrong, A. R.; Armstrong, G.; Canales, J.; Bruce, P. G. TiO₂-B Nanowires as Negative Electrodes for Rechargeable Lithium Batteries. *J. Power Sources* **2005**, *146*, 501-506.
120. Guo, Y.-G.; Hu, Y.-S.; Sigle, W.; Maier, J. Superior Electrode Performance of Nanostructured Mesoporous TiO₂ (Anatase) through Efficient Hierarchical Mixed Conducting Networks. *Adv. Mater.* **2007**, *19*, 2087-2091.

121. Hu, Y.-S.; Kienle, L.; Guo, Y.-G.; Maier, J. High Lithium Electroactivity of Nanometer-Sized Rutile TiO₂. *Adv. Mater.* **2006**, *18*, 1421-1426.
122. Brutti, S.; Gentili, V.; Menard, H.; Scrosati, B.; Bruce, P. G. TiO₂-(B) Nanotubes as Anodes for Lithium Batteries: Origin and Mitigation of Irreversible Capacity. *Adv. Energy Mater.* **2012**, *2*, 322-327.
123. Anji Reddy, M.; Pralong, V.; Varadaraju, U. V.; Raveau, B. Crystallite Size Constraints on Lithium Insertion into Brookite TiO₂. *Electrochem. Solid-State Lett.* **2008**, *11*, A132-A134.
124. Nam, S. H.; Shim, H.-S.; Kim, Y.-S.; Dar, M. A.; Kim, J. G.; Kim, W. B. Ag or Au Nanoparticle-Embedded One-Dimensional Composite TiO₂ Nanofibers Prepared via Electrospinning for Use in Lithium-Ion Batteries. *ACS Appl. Mater. Interfaces* **2010**, *2*, 2046-2052.
125. He, B.-L.; Dong, B.; Li, H.-L. Preparation and Electrochemical Properties of Ag-Modified TiO₂ Nanotube Anode Material for Lithium-Ion Battery. *Electrochem. Commun.* **2007**, *9*, 425-430.
126. Li, N.; Liu, G.; Zhen, C.; Li, F.; Zhang, L.; Cheng, H.-M. Battery Performance and Photocatalytic Activity of Mesoporous Anatase TiO₂ Nanospheres/Graphene Composites by Template-Free Self-Assembly. *Adv. Funct. Mater.* **2011**, *21*, 1717-1722.
127. Hou, J.; Wu, R.; Zhao, P.; Chang, A.; Ji, G.; Gao, B.; Zhao, Q. Graphene-TiO₂(B) Nanowires Composite Material: Synthesis, Characterization and Application in Lithium-Ion Batteries. *Mater. Lett.* **2013**, *100*, 173-176.
128. Xin, X.; Zhou, X.; Wu, J.; Yao, X.; Liu, Z. Scalable Synthesis of TiO₂/Graphene Nanostructured Composite with High-Rate Performance for Lithium Ion Batteries. *ACS Nano* **2012**, *6*, 11035-11043.
129. Kamat, P. V. Graphene-Based Nanoassemblies for Energy Conversion. *J. Phys. Chem. Lett.* **2011**, *2*, 242-251.
130. Kavan, L.; Prochazka, J.; Spitler, T. M.; Kalbac, M.; Zukalova, M.; Drezen, T.; Gratzel, M. Li Insertion into Li₄Ti₅O₁₂ (Spinel). *J. Electrochem. Soc.* **2003**, *150*, A1000-A1007.
131. Zhou, H.; Li, D.; Hibino, M.; Honma, I. A Self-Ordered, Crystalline-Glass, Mesoporous Nanocomposite for Use as a Lithium-Based Storage Device with Both High Power and High Energy Densities. *Angew. Chem., Int. Ed.* **2005**, *44*, 797-802.

132. Xia, T.; Zhang, W.; Murowchick, J.; Liu, G.; Chen, X. Built-in Electric Field-Assisted Surface-Amorphized Nanocrystals for High-Rate Lithium-Ion Battery. *Nano Lett.* **2013**, *13*, 5289-5296.
133. Guo, Y.-G.; Hu, J.-S.; Wan, L.-J. Nanostructured Materials for Electrochemical Energy Conversion and Storage Devices. *Adv. Mater.* **2008**, *20*, 2878-2887.
134. Jiang, Y.; Li, M.; Song, D.; Li, X.; Yu, Y. A Novel 3D Structure Composed of Strings of Hierarchical TiO₂ Spheres Formed on TiO₂ Nanobelts with High Photocatalytic Properties. *J. Solid State Chem.* **2014**, *211*, 90-94.
135. Jung, H.-G.; Yoon, C.-S.; Prakash, J.; Sun, Y.-K., Mesoporous Anatase TiO₂ with High Surface Area and Controllable Pore Size by F-Ion Doping: Applications for High-Power Li-Ion Battery Anode. *J. Phys. Chem. C* **2009**, *113*, 21258-21263.
136. Ye, J.-F.; Liu, W.; Cai, J.-G.; Chen, S.; Zhao, X.-W.; Zhou, H.-H.; Qi, L.-M. Nanoporous Anatase TiO₂ Mesocrystals: Additive-Free Synthesis, Remarkable Crystalline-Phase Stability, and Improved Lithium Insertion Behavior. *J. Am. Chem. Soc.* **2011**, *133*, 933-940.
137. Wang, H.-E.; Cheng, H.; Liu, C.; Chen, X.; Jiang, Q.; Lu, Z.; Li, Y. Y.; Chung, C. Y.; Zhang, W.; Zapien, J. A.; Martinu, L.; Bello, I. Facile Synthesis and Electrochemical Characterization of Porous and Dense TiO₂ Nanospheres for Lithium-Ion Battery Applications. *J. Power Sources* **2011**, *196*, 6394-6399.
138. Gao, X.; Zhu, H.; Pan, G.; Ye, S.; Lan, Y.; Wu, F.; Song, D. Preparation and Electrochemical Characterization of Anatase Nanorods for Lithium-Inserting Electrode Material. *J. Phys. Chem. B* **2004**, *108*, 2868-2872.
139. Armstrong, A. R.; Armstrong, G.; Canales, J.; Garcia, R.; Bruce, P. G. Lithium-Ion Intercalation into TiO₂-B Nanowires. *Adv. Mater.* **2005**, *17*, 862-865.
140. Jun, Y.; Park, J. H.; Kang, M. G. The Preparation of Highly Ordered TiO₂ Nanotube Arrays by an Anodization Method and Their Applications. *Chem. Commun.* **2012**, *48*, 6456-6471.
141. Park, S.-J.; Kim, Y.-J.; Lee, H. Synthesis of Carbon-Coated TiO₂ Nanotubes for High-Power Lithium-Ion Batteries. *J. Power Sources* **2011**, *196*, 5133-5137.
142. Yang, H. G.; Sun, C. H.; Qiao, S. Z.; Zou, J.; Liu, G.; Smith, S. C.; Cheng, H. M.; Lu, G. Q. Anatase TiO₂ Single Crystals with a Large Percentage of Reactive Facets. *Nature* **2008**, *453*, 638-641.
143. Chen, J. S.; Tan, Y. L.; Li, C. M.; Cheah, Y. L.; Luan, D.; Madhavi, S.; Boey, F. Y. C.; Archer, L. A.; Lou, X. W. Constructing Hierarchical Spheres from Large

- Ultrathin Anatase TiO₂ Nanosheets with Nearly 100% Exposed (001) Facets for Fast Reversible Lithium Storage. *J. Am. Chem. Soc.* **2010**, *132*, 6124-6130.
144. Ohzuku, T.; Takehara, Z.; Yoshizawa, S. Nonaqueous Lithium-Titanium Dioxide cell. *Electrochim. Acta* **1979**, *24*, 219-222.
 145. Macklin, W. J.; Neat, R. J. Performance of Titanium Dioxide-Based Cathodes in a Lithium Polymer Electrolyte Cell. *Solid State Ionics* **1992**, *53-56*, 694-700.
 146. Howard, C. J.; Sabine, T. M.; Dickson, F. Structural and Thermal Parameters for Rutile and Anatase. *Acta Crystallogr., Sect. B Struct. Sci.* **1991**, *B47*, 462-468.
 147. Tielens, F.; Calatayud, M.; Beltran, A.; Minot, C.; Andres, J. Lithium Insertion and Mobility in the TiO₂-Anatase/Titanate Structure: A Periodic DFT Study. *J. Electroanal. Chem.* **2005**, *581*, 216-223.
 148. Lunell, S.; Stashans, A.; Ojamae, L.; Lindstroem, H.; Hagfeldt, A. Li and Na Diffusion in TiO₂ from Quantum Chemical Theory versus Electrochemical Experiment. *J. Am. Chem. Soc.* **1997**, *119*, 7374-7380.
 149. Cava, R. J.; Murphy, D. W.; Zahurak, S.; Santoro, A.; Roth, R. S. The Crystal Structures of the Lithium-Inserted Metal Oxides Li_{0.5}TiO₂ Anatase, LiTi₂O₄ Spinel, and Li₂Ti₂O₄. *J. Solid State Chem.* **1984**, *53*, 64-75.
 150. Sudant, G.; Baudrin, E.; Larcher, D.; Tarascon, J.-M. Electrochemical Lithium Reactivity with Nanotextured Anatase-Type TiO₂. *J. Mater. Chem.* **2005**, *15*, 1263-1269.
 151. Wagemaker, M.; Kentgens, A. P. M.; Mulder, F. M. Equilibrium Lithium Transport between Nanocrystalline Phases in Intercalated TiO₂ Anatase. *Nature*, **2002**, *418*, 397-399.
 152. Wagemaker, M.; van de Krol, R.; Kentgens, A. P. M.; van Well, A. A.; Mulder, F. M. Two Phase Morphology Limits Lithium Diffusion in TiO₂ (Anatase): A ⁷Li MAS NMR Study. *J. Am. Chem. Soc.* **2001**, *123*, 11454-11461.
 153. Wagemaker, M.; Borghols, W. J. H.; Mulder, F. M. Large Impact of Particle Size on Insertion Reactions. A Case for Anatase Li_xTiO₂. *J. Am. Chem. Soc.* **2007**, *129*, 4323-4327.
 154. Koudriachova, M. V.; Harrison, N. M.; de Leeuw, S. W. First Principles Predictions for Intercalation Behaviour. *Solid State Ionics* **2004**, *175*, 829-834.

155. Arrouvel, C.; Parker, S. C.; Islam, M. S. Lithium Insertion and Transport in the TiO₂-B Anode Material: A Computational Study. *Chem. Mater.* **2009**, *21*, 4778-4783.
156. Armstrong, G.; Armstrong, A. R.; Canales, J.; Bruce, P. G. Nanotubes with the TiO₂-B Structure. *Chem. Commun.* **2005**, 2454-2456.
157. Armstrong, G.; Armstrong, A. R.; Canales, J.; Bruce, P. G. TiO₂(B) Nanotubes as Negative Electrodes for Rechargeable Lithium Batteries. *Electrochem. Solid-State Lett.* **2006**, *9*, A139-A143.
158. Dambournet, D.; Chapman, K. W.; Koudriachova, M. V.; Chupas, P. J.; Belharouak, I.; Amine, K. Combining the Pair Distribution Function and Computational Methods to Understand Lithium Insertion in Brookite (TiO₂). *Inorg. Chem.* **2011**, *50*, 5855-5857.
159. Fu, L. J.; Liu, H.; Li, C.; Wu, Y. P.; Rahm, E.; Holze, R.; Wu, H. Q. Surface Modifications of Electrode Materials for Lithium Ion Batteries. *Solid State Sci.* **2006**, *8*, 113-128.
160. Kang, K.-Y.; Lee, Y.-G.; Kim, S.; Seo, S. R.; Kim, J.-C.; Kim, K. M. Electrochemical Properties of Carbon-Coated TiO₂ Nanotubes as a Lithium Battery Anode Material. *Mater. Chem. Phys.* **2012**, *137*, 169-176.
161. Kim, H.; Kim, M. G.; Shin, T. J.; Shin, H.-J.; Cho, J. TiO₂@Sn Core-Shell Nanotubes for Fast and High Density Li-Ion Storage Material. *Electrochem. Commun.* **2008**, *10*, 1669-1672.
162. Mancini, M.; Kubiak, P.; Geserick, J.; Marassi, R.; Huesing, N.; Wohlfahrt-Mehrens, M. Mesoporous Anatase TiO₂ Composite Electrodes: Electrochemical Characterization and High Rate Performances. *J. Power Sources* **2009**, *189*, 585-589.
163. Qiao, Y.; Hu, X.; Liu, Y.; Liang, G.; Croft, M. C.; Huang, Y. Surface Modification of MoO_xS_y on Porous TiO₂ Nanospheres as an Anode Material with Highly Reversible and Ultra-Fast Lithium Storage Properties. *J. Mater. Chem. A* **2013**, *1*, 15128-15134.
164. Luo, W.; Hu, X.; Sun, Y.; Huang, Y. Surface Modification of Electrospun TiO₂ Nanofibers via Layer-by-Layer Self-Assembly for High-Performance Lithium-Ion Batteries. *J. Mater. Chem.* **2012**, *22*, 4910-4915.
165. Chandiran, A. K.; Sauvage, F.; Etgar, L.; Graetzel, M. Ga³⁺ and Y³⁺ Cationic Substitution in Mesoporous TiO₂ Photoanodes for Photovoltaic Applications. *J. Phys. Chem. C* **2011**, *115*, 9232-9240.

166. Kyeremateng, N. A.; Hornebecq, V.; Martinez, H.; Knauth, P.; Djenizian, T. Electrochemical Fabrication and Properties of Highly Ordered Fe-Doped TiO₂ Nanotubes. *ChemPhysChem* **2012**, *13*, 3707-3713.
167. Andriamiadamanana, C.; Laberty-Robert, C.; Sougrati, M. T.; Casale, S.; Davoisne, C.; Patra, S.; Sauvage, F. Room-Temperature Synthesis of Iron-Doped Anatase TiO₂ for Lithium-Ion Batteries and Photocatalysis. *Inorg. Chem.* **2014**, *53*, 10129-10139.
168. Liu, S.; Jia, H.; Han, L.; Wang, J.; Gao, P.; Xu, D.; Yang, J.; Che, S. Nanosheet-Constructed Porous TiO₂-B for Advanced Lithium Ion Batteries. *Adv. Mater.* **2012**, *24*, 3201-3204.
169. Wang, Z. L., Transmission Electron Microscopy of Shape-Controlled Nanocrystals and Their Assemblies. *J. Phys. Chem. B* **2000**, *104*, 1153-1175.
170. Jenkins, R.; Snyder, R.; Editors, *Introduction to X-Ray Powder Diffraction*; Wiley: New York, 1996.
171. Cullity, B. D. *Elements of X-Ray Diffraction (2nd Ed.)*; Addison-Wesley Publishing Company INC.: Boston, 1978.
172. Moram, M. A.; Vickers, M. E. X-Ray Diffraction of III-Nitrides. *Rep. Prog. Phys.* **2009**, *72*, 036502/1-036502/40.
173. Gardiner, D. J.; Graves, P. R. Eds. *Practical Raman Spectroscopy*; Springer-Verlag: Berlin, 1989.
174. Gouadec, G.; Colomban, P. Raman Spectroscopy of Nanomaterials. How Spectra Relate to Disorder, Particle Size and Mechanical Properties. *Prog. Cryst. Growth Charact. Mater.* **2007**, *53*, 1-56.
175. Kelly, S.; Pollak, F. H.; Tomkiewicz, M. Raman Spectroscopy as a Morphological Probe for TiO₂ Aerogels. *J. Phys. Chem. B* **1997**, *101*, 2730-2734.
176. Chen, X.; Liu, L.; Yu, P. Y.; Mao, S. S. Increasing Solar Absorption for Photocatalysis with Black Hydrogenated Titanium Dioxide Nanocrystals. *Science* **2011**, *331*, 746-750.
177. Silverstein, R. M.; Webster, F. X.; Kiemie, D. *Spectrometric Identification of Organic Compounds (7th Ed.)*; Wiley: New York, 2002.
178. Zou, J.; Gao, J.; Xie, F. An Amorphous TiO₂ Sol Sensitized with H₂O₂ with the Enhancement of Photocatalytic Activity. *J. Alloys Compd.* **2010**, *497*, 420-427.
179. Craig, D. Q. M.; Reading, M. Eds. *Thermal Analysis of Pharmaceuticals*; CRC Press: Boca Raton, 2007.

180. Lund, A.; Shiotani, M.; Shimada, S., *Principles and Applications of ESR Spectroscopy*; Springer: Dordrecht, Heidelberg, London, New York, 2011.
181. Liu, G.; Xun, S.; Vukmirovic, N.; Song, X.; Olalde-Velasco, P.; Zheng, H.; Battaglia, V. S.; Wang, L.; Yang, W. Polymers with Tailored Electronic Structure for High Capacity Lithium Battery Electrodes. *Adv. Mater.* **2011**, *23*, 4679-4683.
182. Ratnakumar, B. V.; Smart, M. C.; Surampudi, S. Electrochemical Impedance Spectroscopy and its Applications to Lithium Ion Cells. *Annu. Battery Conf. Appl. Adv.*, *17th* **2002**, 273-277.
183. Lu, X.; Wang, G.; Zhai, T.; Yu, M.; Gan, J.; Tong, Y.; Li, Y. Hydrogenated TiO₂ Nanotube Arrays for Supercapacitors. *Nano Lett.*, **2012**, *12*, 1690-1696.
184. Li, G.; Li, L.; Boerio-Goates, J.; Woodfield, B. F. High Purity Anatase TiO₂ Nanocrystals: Near Room-Temperature Synthesis, Grain Growth Kinetics, and Surface Hydration Chemistry. *J. Am. Chem. Soc.* **2005**, *127*, 8659-8666.
185. Kuvarega, A. T.; Krause, R. W. M.; Mamba, B. B. Nitrogen/Palladium-Codoped TiO₂ for Efficient Visible Light Photocatalytic Dye Degradation. *J. Phys. Chem. C* **2011**, *115*, 22110-22120.
186. Crocker, M.; Herold, R. H. M.; Wilson, A. E.; Mackay, M.; Emeis, C. A.; Hoogendoorn, A. M. ¹H NMR Spectroscopy of Titania. Chemical Shift Assignments for Hydroxy Groups in Crystalline and Amorphous Forms of TiO₂. *J. Chem. Soc., Faraday Trans.* **1996**, *92*, 2791-2798.
187. Morimoto, H.; Yamashita, H.; Tatsumisago, M.; Minami, T. Mechanochemical Synthesis of New Amorphous Materials of 60Li₂S·40SiS₂ with High Lithium Ion Conductivity. *J. Am. Ceram. Soc.* **1999**, *82*, 1352-1354.
188. Guan, D.; Cai, C.; Wang, Y. Amorphous and Crystalline TiO₂ Nanotube Arrays for Enhanced Li-Ion Intercalation Properties. *J. Nanosci. Nanotechnol.* **2011**, *11*, 3641-3650.
189. Wakihara, M.; Yamamoto, O. Eds. *Lithium Ion Batteries: Fundamentals and Performance*; Kodansha: Tokyo-WileyVCH Verlag GmbH: Weinheim, 1998.
190. Grey, C. P.; Dupre, N. NMR Studies of Cathode Materials for Lithium-Ion Rechargeable Batteries. *Chem. Rev.* **2004**, *104*, 4493-4512.
191. Jonsen, P. A Proton NMR Study of Reduced Ruthenium/Titania and Titania. *Colloids Surf.* **1989**, *36*, 127-132.

192. Jonsen, P. Identification of Different Hydrogen-Reduced Titania Crystallographic Forms by Proton NMR Spectroscopy. *Catal. Lett.* **1989**, *2*, 345-349.
193. Aschauer, U.; Selloni, A. Hydrogen Interaction with the Anatase TiO₂(101) Surface. *Phys. Chem. Chem. Phys.* **2012**, *14*, 16595-16602.
194. Jun, J.; Dhayal, M.; Shin, J.-H.; Kim, J.-C.; Getoff, N. Surface Properties and Photoactivity of TiO₂ Treated with Electron Beam. *Radiat. Phys. Chem.* **2006**, *75*, 583-589.
195. Dohshi, S.; Anpo, M.; Okuda, S.; Kojima, T. Effect of γ -Ray Irradiation on the Wettability of TiO₂ Single Crystals. *Top. Catal.* **2005**, *35*, 327-330.
196. Champness, P., Pamela, *Electron Diffraction in the Transmission Electron Microscope*; Taylor & Francis: New York, 2001.
197. Fultz, B.; Howe, J. *Transmission Electron Microscopy and Diffractometry of Materials*; Springer: New York, 2009.
198. Xia, T.; Chen, X. Revealing the Structural Properties of Hydrogenated Black TiO₂ Nanocrystals. *J. Mater. Chem. A* **2013**, *1*, 2983-2989.
199. Xia, T.; Zhang, W.; Murowchick, J. B.; Liu, G.; Chen, X. A Facile Method to Improve the Photocatalytic and Lithium-Ion Rechargeable Battery Performance of TiO₂ Nanocrystals. *Adv. Energy Mater.* **2013**, *3*, 1516-1523.
200. Nakamura, I.; Negishi, N.; Kutsuna, S.; Ihara, T.; Sugihara, S.; Takeuchi, K. Role of Oxygen Vacancy in the Plasma-Treated TiO₂ Photocatalyst with Visible Light Activity for NO Removal. *J. Mol. Catal. A Chem.* **2000**, *161*, 205-212.
201. Diebold, U. The Surface Science of Titanium Dioxide. *Surf. Sci. Rep.* **2003**, *48*, 53-229.
202. Berube, V.; Radtke, G.; Dresselhaus, M.; Chen, G. Size Effects on the Hydrogen Storage Properties of Nanostructured Metal Hydrides: A Review. *Int. J. Energy Res.* **2007**, *31*, 637-663.
203. Asahi, R.; Morikawa, T.; Ohwaki, T.; Aoki, K.; Taga, Y. Visible-Light Photocatalysis in Nitrogen-Doped Titanium Oxides. *Science* **2001**, *293*, 269-271.
204. Chen, X.; Burda, C. The Electronic Origin of the Visible-Light Absorption Properties of C-, N- and S- Doped TiO₂ Nanomaterials. *J. Am. Chem. Soc.* **2008**, *130*, 5018-5019.

205. Wang, G.; Wang, H.; Ling, Y.; Tang, Y.; Yang, X.; Fitzmorris, R. C.; Wang, C.; Zhang, J. Z.; Li, Y. Hydrogen-Treated TiO₂ Nanowire Arrays for Photoelectrochemical Water Splitting. *Nano Lett.* **2011**, *11*, 3026-3033.
206. Hagfeldt, A.; Graetzel, M. Light-Induced Redox Reactions in Nanocrystalline Systems. *Chem. Rev.* **1995**, *95*, 49-68.
207. Janotti, A.; Varley, J. B.; Rinke, P.; Umezawa, N.; Kresse, G.; Van de Walle, C. G. Hybrid Functional Studies of the Oxygen Vacancy in TiO₂. *Phys. Rev. B Condens. Matter Mater. Phys.* **2010**, *81*, 085212/1-085212/7.
208. Yu, P. Y.; Cardona, M. *Fundamentals of Semiconductors: Physics and Materials Properties (3rd Ed.)*; Springer: Dordrecht, Heidelberg, London, New York, 2001.
209. Cui, L.-F.; Ruffo, R.; Chan, C. K.; Peng, H.; Cui, Y. Crystalline-Amorphous Core-Shell Silicon Nanowires for High Capacity and High Current Battery Electrodes. *Nano Lett.* **2009**, *9*, 491-495.
210. Li, Y.; Li, X.; Li, J.; Yin, J. TiO₂-Coated Active Carbon Composites with Increased Photocatalytic Activity Prepared by a Properly Controlled Sol-Gel Method. *Mater. Lett.* **2005**, *59*, 2659-2663.

VITA

Ting Xia was born on June 16, 1983 in Suzhou, China, where she attended elementary, middle school and high school. In 2002, she was admitted by the Nanjing University of Technology, China. In 2006, she obtained her Bachelor's degree in chemical engineering and technology. During the four years' study, she became interested in chemistry and wanted to continue the study. Thus, in 2008, she took the national entrance examination for postgraduate and was enrolled in master program in applied chemistry in the Zhejiang University, China.

Thereafter, Ting held positions in management trainee, lab control and then quality assurance in BeautyCos International Co., Ltd., a subsidiary of L'Oreal group.

After approximately three and half years' experience in industry, Ting returned to the academic institute. She was admitted as a graduate student at the University of Missouri-Kansas City in January 2012 and started to pursue doctoral degree in Chemistry. She was appointed as a teaching assistant and research assistant. Her research was mainly on titanium dioxide nanocrystals used for the lithium-ion battery. The list of publications that she had co-authored and the list of presentations at regional conferences are shown below.

PUBLICATIONS

- Y. Zhang; Q. Zhang; T. Xia; D. Zhu; Y. Chen; X. Chen. The Influence of Reaction Temperature on the Formation and Photocatalytic Hydrogen Generation of (001) Faceted TiO₂ Nanosheets. *ChemNanoMat*. **2015**, DOI: 10.1002/cnma.201500030.
- T. Xia; Y. Cao; N. A. Oyler; J. Murowchick; L. Liu; X. Chen. Strong Microwave Absorption of Hydrogenated Wide Bandgap Semiconductor Nanoparticles. *ACS Appl. Mater. Interfaces* **2015**, 7, 10407-10413
- T. Xia; C. Zhang; N. A. Oyler; X. Chen. Enhancing Microwave Absorption of TiO₂ Nanocrystals via Hydrogenation. *J. Mater. Res.* **2014**, 29, 2198-2210.
- T. Xia; P. Wallenmeyer; A. Anderson; J. Murowchick; L. Liu; X. Chen. Hydrogenated Black ZnO Nanoparticles with Enhanced Photocatalytic Performance. *RSC Advances* **2014**, 4, 41654-41658.
- Y. Zhang; M. Shang; Y. Mi; T. Xia; P. Wallenmeyer; J. Murowchick; L. Dong; Q. Zhang; X. Chen. Influence of the Amount of HF on the Formation of (001) Faceted TiO₂ Nanosheets and Their Photocatalytic Hydrogen Generation Performance. *ChemPlusChem* **2014**, 79, 1159-1166.
- Z. Wang; Y. Zhang; T. Xia; J. Murowchick; G. Liu; X. Chen. Lithium-Ion Battery Performance of (001) Faceted TiO₂ Nanosheets vs. Spherical TiO₂ Nanoparticles. *Energy Technology* **2014**, 2, 376-382.
- T. Xia; W. Zhang; Z. Wang; Y. Zhang; X. Song; J. Murowchick; V. Battaglia; G. Liu; X. Chen. Amorphous Carbon-Coated TiO₂ Nanocrystals for Improved Lithium-Ion Battery and Photocatalytic Performance. *Nano Energy* **2014**, 6, 109-118.
- Y. Zhang; T. Xia; K. M. Yu; F. Zhang; H. Yang; B. Liu; Y. An; Y. Yin; X. Chen. Facile Synthesis of [Cu(SCH₃)]_∞ Nanowires with High Charge Mobility. *ChemPlusChem* **2014**, 79, 559-563.
- Y. Zhang; T. Xia; M. Shang; P. Wallenmeyer; D. Katelyn; A. Peterson; J. Murowchick; L. Dong; X. Chen. Structural Evolution from TiO₂ Nanoparticles to Nanosheets and Their Photocatalytic Performance in Hydrogen Generation and Environmental Pollution Removal. *RSC Advances* **2014**, 4, 16146-16152.
- Y. Zhang; T. Xia; P. Wallenmeyer; C. X. Harris; A. A. Peterson; G. A. Corsiglia; J. Murowchick; X. Chen. Photocatalytic Hydrogen Generation from Pure Water with Silicon Carbide Nanoparticles. *Energy Technology* **2014**, 2, 183-187.

- X. Li; T. Xia; C. Xu; J. Murowchick; X. Chen. Synthesis and Photoactivity of Nanostructured CdS-TiO₂ Composite Catalysts. *Catal. Today* **2014**, 225, 64-73.
- T. Xia; Y. Zhang; J. Murowchick; X. Chen. Vacuum-Treated Titanium Dioxide Nanocrystals: Optical Properties, Surface Disorder, Oxygen Vacancy, and Photocatalytic Activities. *Catal. Today* **2014**, 225, 2-9.
- S. Li; G. Tan; J. B. Murowchick; C. Wisner; N. Leventis; T. Xia; X. Chen; Z. Peng. Preparation of Uncapped CdSe_xTe_{1-x} Nanocrystals with Strong Near-IR Tunable Absorption. *J. Electronic Mater.* **2013**, 42, 3373-3378.
- T. Xia; W. Zhang; J. Murowchick; G. Liu; X. Chen. Built-in Electric Field-Assisted Surface-Amorphized Nanocrystals for High-Rate Lithium-Ion Battery. *Nano Lett.* **2013**, 13, 5289-5296.
- T. Xia; N. Li; Y. Zhang; M. B. Kruger; J. Murowchick; A. Selloni; X. Chen. Directional Heat Dissipation across the Interface in Anatase-Rutile Nanocomposites. *ACS Appl. Mater. Interfaces* **2013**, 5, 9883-9890.
- T. Xia; C. Zhang; N. A. Oyler; X. Chen. Hydrogenated TiO₂ Nanocrystals: A Novel Microwave Absorbing Material. *Adv. Mater.* **2013**, 25, 6905-6910.
- T. Xia; W. Zhang; J. Murowchick; G. Liu; X. Chen. A Facile Method to Improve the Photocatalytic and Lithium-Ion Rechargeable Battery Performance of TiO₂ Nanocrystals. *Adv. Energy Mater.* **2013**, 3, 1516-1523.
- T. Xia; W. Zhang; W. Li; N. A. Oyler; G. Liu; X. Chen. Hydrogenated Surface Disorder Enhances Lithium Ion Battery Performance. *Nano Energy* **2013**, 2, 826-835.
- T. Xia; X. Chen. Revealing the Structural Properties of Hydrogenated Black TiO₂ Nanocrystals. *J. Mater. Chem. A* **2013**, 1, 2983-2989.
- T. Xia; J. W. Otto; T. Dutta; J. Murowchick; A. N. Caruso; Z. Peng; X. Chen. Formation of TiO₂ Nanomaterials via Titanium Ethylene Glycolide Decomposition. *J. Mater. Res.* **2013**, 28, 326-332.

ORAL AND POSTER PRESENTATIONS

- Poster presentation in the 47th American Chemistry Society (ACS) Midwest Regional Meeting, October 24-27, Omaha, NE, USA. "Formation of TiO₂ Nanomaterials via Titanium Ethylene Glycolide."

- Oral presentation in the 48th American Chemistry Society (ACS) Midwest Regional Meeting of the American Chemical Society, October 16-19, Springfield, MO, USA. “Phase Transformation Study on TiO₂ Nanomaterials by Calcination.”